technische universität
dortmund

Department
of Physics

Atmospheric Seasoning

Unfolding the Seasonal Variations of the Atmospheric Neutrino Flux

Karolin Hymon
2024

A document submitted in partial fulfillment of the
requirements for the degree of
Doctor rerum naturalium
at
Technische Universität Dortmund

Supervised by
Prof. Dr. Dr. Wolfgang Rhode and Dr. Chris Malena Delitzsch

Abstract

Besides the detection of astrophysical neutrinos, atmospheric neutrinos from cosmic-ray-induced air showers are detected at unprecedented statistics with the IceCube Neutrino Observatory. The conventional component of the atmospheric neutrino flux is produced in decays of kaons and pions. Due to seasonal changes in the atmospheric temperature, the neutrino flux undergoes a seasonal variation. When the temperature increases, the atmosphere expands, and more neutrinos are expected to be produced. Additionally, the seasonal variation increases with energy, as parent particles interact at higher altitudes in the atmosphere, where seasonal temperature variations are larger. The interaction cross section increases with energy and the probability for the parent meson to decay increases. The investigation of seasonal variations serves as an accurate background determination in the search for astrophysical neutrinos and the study of hadronic interactions in atmospheric particle cascades.

In this thesis, seasonal variations in the atmospheric neutrino flux are measured energy-dependently for the first time based on 11.5 years of IceCube data. The determination of the neutrino energy presents an ill-conditioned inverse problem, requiring to infer the energy from measured detector quantities. This challenge is addressed by the Dortmund Spectrum Estimation Algorithm (DSEA+), which utilizes machine learning methods to unfold the neutrino energy. The determined variation strength is compared to theoretical predictions from MCEq, and in particular to the calculation with the atmospheric model NRLMSISE-00.

Kurzfassung

Neben dem Nachweis astrophysikalischer Neutrinos werden mit dem IceCube-Neutrino-Observatorium viele Größenordnungen mehr atmosphärische Neutrinos aus Luftschauern der kosmischen Strahlung gemessen. Die konventionelle Komponente des atmosphärischen Neutrinoflusses entsteht durch Zerfälle von Kaonen und Pionen. Aufgrund der jahreszeitlichen Änderung der atmosphärischen Temperatur unterliegt der Neutrinofluss einer jahreszeitlichen Schwankung. Wenn die Temperatur steigt, expandiert die Atmosphäre und die Neutrinoproduktion steigt. Des Weiteren steigt die jahreszeitliche Schwankung des Flusses mit der Energie an, da die Elternteilchen in größeren Höhen in der Atmosphäre wechselwirken, wo die Temperaturschwankungen größer sind. Gleichzeitig steigt auch der Wechselwirkungsquerschnitt mit der Energie, und damit die Wahrscheinlichkeit, dass das Elternmeson zerfällt. Die Untersuchung der jahreszeitlichen Schwankungen dient als präzise Untergrundbestimmung bei der Suche nach astrophysikalischen Neutrinos und der Analyse hadronischer Wechselwirkungen in atmosphärischen Teilchenkaskaden.

In dieser Dissertation wurden zum ersten Mal saisonale Schwankungen des atmosphärischen Neutrinoflusses energieabhängig gemessen, basierend auf 11,5 Jahren IceCube-Daten. Die Bestimmung der Neutrinoenergie stellt ein schlecht konditioniertes inverses Problem dar, bei dem die Energie aus gemessenen Detektorgrößen abgeleitet werden muss. Dies wird durch den Dortmund Spectrum Estimation Algorithm (DSEA+) addressiert, welcher Methoden des maschinellen Lernens zur Entfaltung der Neutrinoenergie nutzt. Die ermittelte saisonale Variationsstärke wird mit theoretischen Vorhersagen von MCEq, insbesondere mit der Berechnung des Atmosphärenmodell NRLMSISE-00 verglichen.

Contents

1 Introduction

Neutrinos are one of the most obscure elementary particles. Many characteristics remain unknown and violate the principles of the Standard Model of particle physics. Neutrinos are predicted to be free of mass, however, the observation of oscillations between their leptonic flavor states implies that neutrinos must carry a small but non-zero mass. Their electrical neutrality and small interaction cross section permit the propagation on straight paths from the depths of the Universe to Earth, making neutrinos excellent astrophysical messengers. Nonetheless, the detection of neutrinos poses significant challenges. Enormous volumes in dense media, for instance, ice or water, are required to indirectly detect high-energy neutrinos and to determine their origin.
Besides providing valuable insight into the processes of particle production in the cosmos, neutrinos are essential for the understanding of particle cascades and hadronic interactions in the atmosphere. Since current accelerator experiments on Earth can only produce particles up to a certain energy limit, our atmosphere serves as a unique particle physics laboratory. A large number of neutrinos, exceeding those of astrophysical origin by several orders of magnitude, are produced in the upper atmosphere within hadronic particle cascades. These cascades are initiated by a charged nucleus originating from an astrophysical object, referred to as cosmic ray (CR). Conventional muon neutrinos from the decay of secondary particles, such as kaons and pions, are of particular interest. Seasonal temperature variations in the atmosphere impact the number of neutrinos produced in these particle cascades, increasing the neutrino production as temperatures rise. In underground experiments, the variation of the neutrino rates has been measured with a significance larger than 10σ [1]. These variations are expected to increase with the particle energy as the lifetime of the parent mesons is Lorentz-boosted. High-energetic primaries interact at higher altitudes in the atmosphere, where temperature variations are larger. However, the energy dependence of the seasonal flux variation has not been measured in atmospheric neutrino experiments so far because of lacking sufficient statistics.

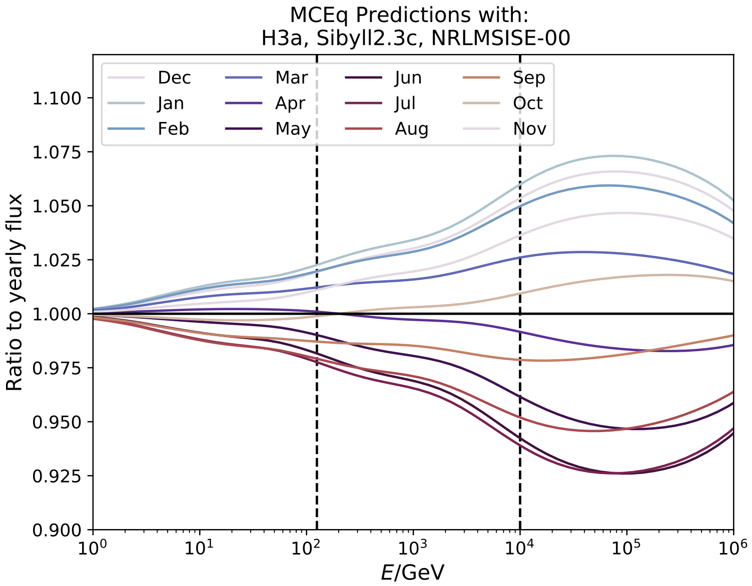

Figure 1.1: Calculated ratio of the monthly muon neutrino flux to annual average for the zenith range from 90° to 120° with MCEq using the Gaisser-Hillas 3 approximation (H3a) [2] as primary CR composition, Sibyll2.3c [3] as hadronic interaction model, and the US Naval Research Laboratory Mass Spectrometer Incoherent Scattering Extension 2000 (NRLMSISE-00) [4] as atmospheric model. Dashed lines mark the investigated energy range in this dissertation. The flux calculation includes neutrinos and antineutrinos for the conventional and prompt atmospheric flux components.

The IceCube Neutrino Observatory is currently the largest neutrino telescope with an instrumented volume of one cubic kilometer inside the Antarctic ice [5]. Providing 11.5 years of neutrino data from complete detector configuration to date, it is the only neutrino telescope with sufficient statistics to measure seasonal variations in the neutrino spectrum at percentage level.

This dissertation aims at the first measurement of seasonal variations in the atmospheric neutrino energy spectrum between 125 GeV and 10 TeV. By utilizing machine learning techniques, the seasonal spectra are determined by a novel approach to spectrum unfolding with the Dortmund Spectrum Estimation Algorithm (DSEA+) [6]. The strength of the variation is obtained by the ratio of the unfolded seasonal to annual average flux. Fig. 1.1 shows the expected results for the ratio of monthly to annual average flux calculated by the Matrix

Cascade Equations (MCEq) [7] code. The energy range of interest in this thesis is represented by dashed lines. The measurement of seasonal variations serves as a way to investigate hadronic interactions in particle showers in the atmosphere, besides the test of the increase of seasonal variations with rising energy. Furthermore, exact modeling of the atmospheric neutrino flux improves the background measurement in astrophysical neutrino searches.

This thesis is structured into the subsequent parts:

Chapter 2 introduces the atmospheric neutrino production in cosmic-ray-induced air showers, the seasonal dependence of conventional atmospheric neutrinos and the current research status.

Chapter 3 illustrates the IceCube Neutrino Observatory, its data acquisition, and event reconstruction techniques.

Chapter 4 outlines selected machine learning algorithms and statistical measures important in the scope of this thesis.

Chapter 5 describes the event selection for atmospheric muon neutrinos and the zenith region to be studied. The concept of weighting simulations to a flux model is explained, and a comparison between data and simulations is presented.

Chapter 6 explains the concept of spectrum unfolding with the DSEA+ algorithm used in this analysis. The selection of estimator variables and their definitions are provided, and internal parameters of the unfolding algorithm are optimized.

Chapter 7 shows the unfolded seasonal energy spectra for the zenith range from 90° to 120° and the determined monthly variation energy-dependently. The statistical and systematic uncertainties that are associated with the unfolded spectra are discussed. The deviation of the unfolded seasonal flux from the annual average flux is determined, and the results are then compared to the theoretical predictions from MCEq.

Chapter 8 discusses the temperature and neutrino rate variations in dependence on the zenith angle. The measurement of seasonal variations in the restricted zenith range from 90° to 110° is determined and compared to MCEq.

Chapter 9 provides an overview of the seasonal variation measurements and discusses future prospects.

2 From Multimessenger Astronomy to Atmospheric Neutrinos

This chapter introduces the field of multimessenger astronomy. The focus is set on two particular messengers, cosmic rays and neutrinos. Basic properties of both messengers are explained, the production mechanism of atmospheric neutrinos, and the seasonal dependence of the flux are elaborated.

2.1 Multimessenger Astronomy

For centuries, optical astronomy was defined as the study of cosmic objects with only visible light. Nowadays, light can be observed across the entire electromagnetic spectrum, which is designated as multiwavelength astronomy. In recent decades, a relatively new field has emerged as a bridge between particle and astrophysics. Particles produced in the cosmos can serve as messengers to study particle production processes and extreme phenomena in the Universe. Gigantic environments, such as Active Galactic Nuclei, can accelerate particles to energies of more than one hundred EeV, creating an extraordinary particle physics laboratory beyond the capacities available on Earth. In addition to observing photons across the entire spectrum, especially gamma rays, charged nuclei (cosmic rays), neutrinos, and, gravitational waves provide insights into astrophysical sources and open up the field of *Multimessenger Astronomy*, as illustrated in Fig. 2.1. While many sources of gamma rays have been confirmed, the era of neutrino astronomy is only now starting. The first high-energy neutrino source discovered was the blazar TXS 0505+065 in 2017 [8], the second was the nearby active galaxy NGC 1068 [9], and recently the Galactic Plane has been revealed as a source of neutrinos [10]. Follow-up observations with different messengers provide detailed insight into the sources and particle interactions in the sources.

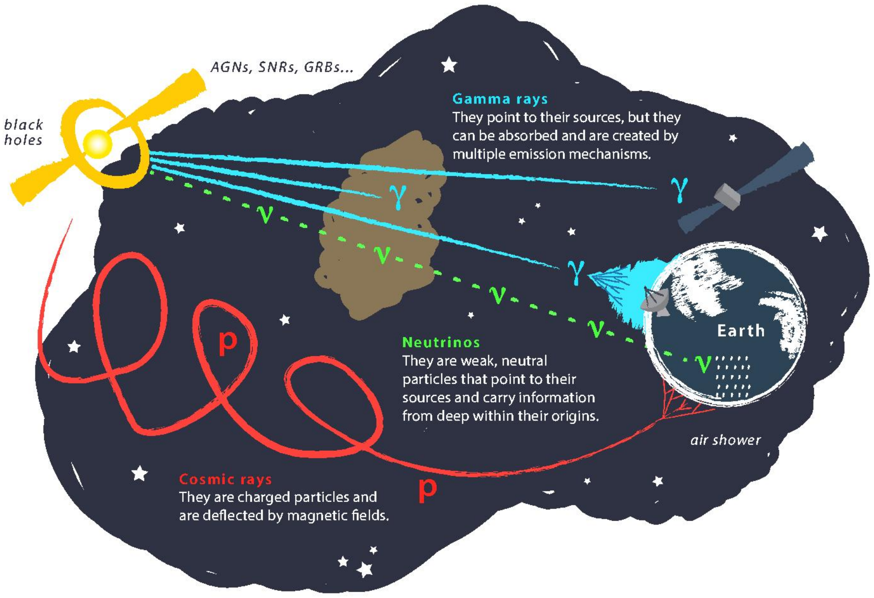

Figure 2.1: Sketch of cosmic messengers and their definition. Gravitational waves were not detected at the time. Figure taken from Ref. [11].

2.2 Cosmic Rays

CRs consist of ionized nuclei: $\sim 90\%$ protons, 9% helium nuclei, and a small fraction of heavier nuclei [12]. They were first discovered more than a century ago by ionization measurements of air in balloon flights by Victor Hess in 1912 [13]. Contrary to what was expected at the time, the radiation detected in the atmosphere increased with altitude, suggesting an extraterrestrial origin of CRs. The arrival direction of CRs is distorted by deflection in galactic and extragalactic magnetic fields, making it extremely challenging to identify their exact origin. Suspected sources are local sources in the Milky Way, such as supernova remnants, or extragalactic sources, such as Active Galactic Nuclei, gamma-ray bursts, or starburst galaxies [12].

2.2.1 Energy Spectrum

The energy of CRs ranges over several orders of magnitude, from GeV CRs from the Solar System, over galactic sources, to EeV CRs from

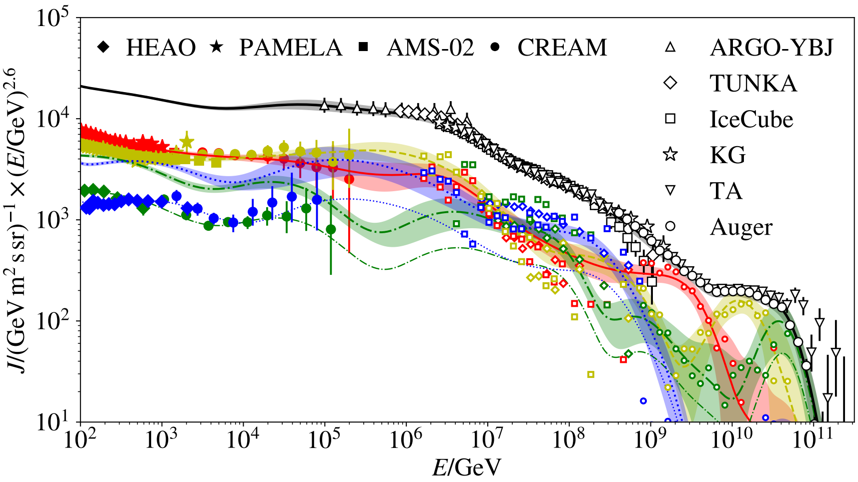

Figure 2.2: All particle CR spectrum from different experiments and the Global Spline Fit for each element group [17]. KG represents measurements from KASCADE-Grande. Colors imply different individual nucleus fluxes: protons (red), helium (yellow), oxygen (gray), iron (blue). The bands around the fit are variations of one standard deviation, and the error bars indicate statistical and systematic uncertainties. The fluxes are corrected for the different energy scales of the experiments.

extragalactic objects. The intensity decreases steeply with increasing energy so that the energy spectrum of CRs can be described by power laws of $J(E) \propto E^{-\gamma}$. Due to the steeply falling spectrum and the need for large detectors, direct detection in space is only feasible up to 100 TeV. Higher energetic CRs are measured indirectly on the ground [12], for instance by the Pierre Auger Observatory (PAO) [14] or the Telescope Array (TA) [15]. Changes in the distribution of source types, production mechanisms, and propagation environments imprint energy-related features on the CR spectrum [16]. The all-particle CR spectrum and the spectra of the individual elements measured by different experiments are shown in Fig. 2.2. Direct measurements from airborne experiments are depicted as filled, indirect measurements as unfilled markers. All measurements are combined into a global fit of the all-particle CR spectrum, denoted as the Global Spline Fit (GSF) [17] CR composition model (refer to the next section).

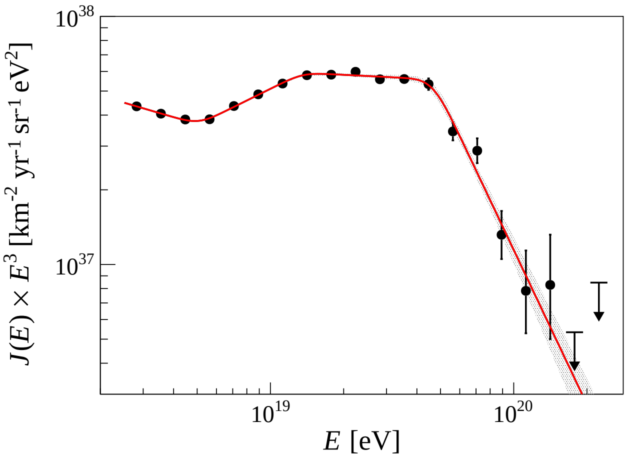

Figure 2.3: Energy spectrum measured by the Pierre Auger Observatory above 2.5 EeV showing the instep feature [21]. The fit of a smoothed broken power law is depicted in red.

The CR spectrum has historically been divided into three parts based on specific features attributed to spectral changes: the *knee* at ~ 5 PeV [18], and the *ankle* at ~ 5 EeV [19, 20]. The CR spectrum up to the knee can be described by the spectral index $\gamma \approx 2.7$. Beyond the knee, the spectrum steepens to $\gamma \geq 3.0$ and hardens to $\gamma \approx 2.6$ above the ankle. Recent measurements have reported additional features in the CR spectrum, defining a distinct separation between the knee and ankle, the low energy ankle at ~ 10 PeV and a second knee at ~ 100 PeV [16]. Both the PAO and the TA reported a new feature, the *instep*, at $\simeq 10$ EeV [21, 22], shown in Fig. 2.3. The presence of the features and their exact structure is not yet completely understood except for compositional changes, as underlined by Fig. 2.2. The increase of the flux above the ankle is attributed to CRs from extragalactic sources. Charged particles remain confined in an acceleration region of radius r up to the Hillas energy

$$E = ZeBr. \tag{2.1}$$

The nuclear charge is denoted by Ze, and the magnetic field strength by B [23]. If a particle exceeds the Hillas energy, it can escape the acceleration environment, propagate through intergalactic magnetic fields, and contribute to an increase in the extragalactic component of the CR flux. The energy spectrum is expected to cut off beyond approx.

60 EeV, which can either be due to sources reaching their maximum energy or the Greisen-Zatsepin-Kuzmin (GZK) effect [24, 25]. The GZK effect describes the interaction of CR protons with photons (photopion production) from the Cosmic Microwave Background (CMB), in which a delta resonance Δ^+ is produced. It decays into protons and neutral pions, or neutrons and positively charged pions:

$$p + \gamma_{\mathrm{CMB}} \rightarrow \Delta^+ \rightarrow \begin{cases} p + \pi^0 \\ n + \pi^+ \end{cases} \tag{2.2}$$

Heavier nuclei interact by photodisintegration [26]. Suppression of the CR flux has been observed by the PAO and the High Resolution Fly's Eye (HiRes) experiment [19, 20]. The energy at which the spectrum cuts off is composition-dependent. Nuclei can be accelerated to the maximum rigidity $R = Z \cdot E_{\mathrm{proton}}$ so that the flux diminishes above the respective maximum acceleration energy. The mass-dependent acceleration and the related spectral cutoffs are referred to as *Peters cycles*, explained in Ref. [27].

2.2.2 Mass Composition Models

The investigation of the relative abundances of CR nuclei provides constraints on their sources and acceleration mechanisms. The composition is investigated based on groups with equal mass in $\ln(A)$. Fig. 2.2 shows how different mass groups contribute to changes in the spectral shape. The spectral evolution is modeled based on elemental mass groups combined into a global fit for the all-particle CR spectrum. The subsequent CR composition models will be discussed in the scope of this thesis:

- The Gaisser-Hillas 3 approximation (H3a) [2] categorizes CRs into five mass groups for different source populations in energy: p, He, CNO, Mg-Si, Fe. The spectrum of nucleon i is expressed by

  $$\Phi_i(E) = \sum_{j=1}^{3} N_{i,j} E^{-\gamma_{i,j}} \cdot \exp\left(\frac{E}{Z_i e R_{c,j}}\right). \tag{2.3}$$

  The fit is performed over $j = 3$ populations, which is why the approximation was named after it. Each population represents CRs from different origins, a galactic component from supernova remnants, a second galactic component from other sources, and a third component from extragalactic sources. $R_{c,j}$ defines the rigidity-based cutoffs, which are fitted simultaneously with the normalization $N_{i,j}$, and the spectral index $\gamma_{i,j}$ for each elemental group and population.

- The alternative Gaisser-Hillas 4 approximation (H4a) is based on the same approach as in Equ. 2.3 with the exception that only protons are present the third population of extragalactic CRs.
- The Gaisser-Stanev-Tilav (GST) [28] model follows the same approach as H3a (Equ. 2.3). Despite five mass groups, an additional group for nuclei beyond iron is introduced. The fit parameters for the individual mass groups are obtained by a fit to data from various experiments, which are shifted in normalization to account for differences in energy calibration.
- The Global Spline Fit (GSF) [17] builds upon GST by a global fit of data from various experiments. The model considers elemental spectra instead of mass groups and does not correct the data from each experiment according to the different energy scales because the energy offsets between the experiments are fitted by the model as well. The data is fitted by cubic B-splines [29] for four mass groups, named after their leading element: p, He, O, Fe (see Fig. 2.2). The spectrum for each leading element is expressed by

  $$\Phi_{\mathrm{L}}(R) = \sum_j N_{i,j} \cdot B_j(\ln({}^{R}\!/_{\mathrm{GV}})) \cdot ({}^{R}\!/_{\mathrm{GV}})^{-3}. \tag{2.4}$$

  Elemental spectra can also be obtained with this model, following the spectral shape of the respective mass group.
- Poly-gonato (PG) [30] is the oldest of the models presented here. The knee is modeled by different species and the high-energy region is interpolated from direct measurements.

2.3 Extensive Air Showers

When a CR enters the atmosphere, it produces an avalanche of subsequent secondary particles in nuclear interactions with air molecules, as illustrated in Fig. 2.4. These initiated particle cascades are referred to as *extensive air showers*, which can be detected by large ground-based detectors such as the Pierre Auger Observatory, Telescope Array, or

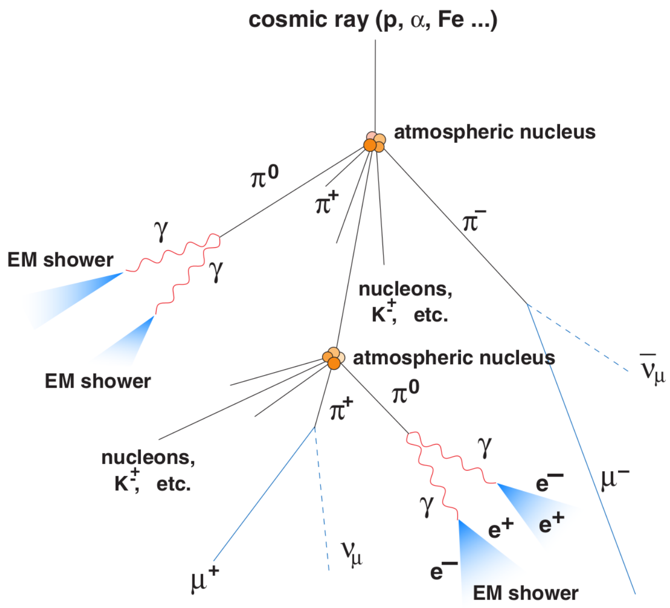

Figure 2.4: Illustration of a CR-induced extensive air shower and the particle species initiated. The sketch displays the lepton production only from pions decay for simplicity. The production via kaon decay follows the same principle. The abbreviation EM indicates the production of an electromagnetic shower. Image taken from Ref. [35].

IceTop (refer to Chapter 3.1). Before state-of-the-art particle accelerators could be built in the enormous sizes we know today, extensive air showers opened up an important field for the discovery of new particles, including the positron e^+ [31], muon $\mu^\pm$ [32], kaon $\mathrm{K}^\pm$ [33], and pion $\pi^{\pm,0}$ [34].

2.3.1 Atmosphere

In the study of extensive air showers, the atmosphere has a significant impact on the development of the air shower, acting as an interaction target for CRs. The atmosphere consists of 78% N_2, 21% O_2, 1% Ar up to an altitude of 100 km with an average mass number of $A \sim 14.5$ [12]. The density of atoms in the atmosphere is an important quantity that models the abundance of interaction targets. The atmospheric density at a given altitude can be approximated by an isothermal gas,

$$\rho(H) = \rho_0 \cdot \exp\left(-{}^{H}/_{H_0}\right), \tag{2.5}$$

with a vertical depth $X_0 = \rho_0 H_0 = 1300\,\mathrm{g\,cm^{-2}}$ [36]. The scale height is derived from the approximation of the chemical composition of the atmosphere as an ideal gas with $H_0 = {}^{RT}/_{Mg} = 6.4\,\mathrm{km}$. The atmospheric depth X can be calculated by integrating the density profile over the trajectory l of the primary particle from the zenith arrival direction Θ [12]:

$$X(l, \Theta) = \int_l^\infty \rho(H(l, \Theta))\mathrm{d}l. \tag{2.6}$$

The atmospheric depth at sea level is $1000\,\mathrm{hPa} = 1000\,\mathrm{g\,cm^{-2}}$ and decreases with altitude. It can be noted that isothermality is an approximation, and atmospheric density and temperature vary daily and seasonally throughout the layered atmosphere (see Section 2.5).

2.3.2 Heitler-Matthews Model

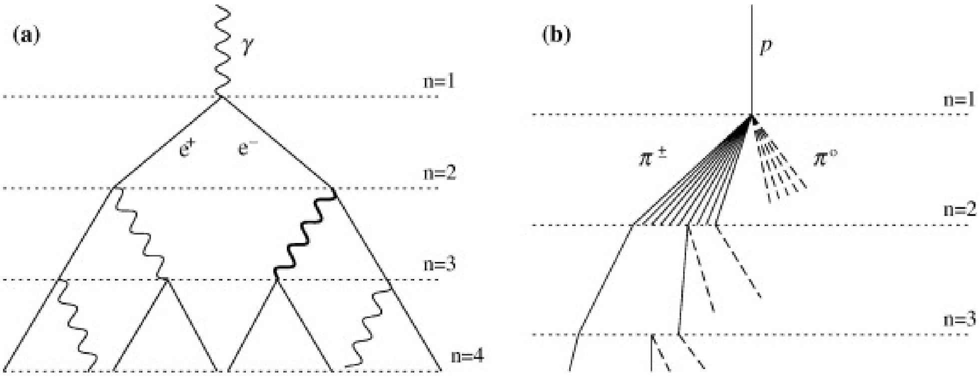

Figure 2.5: Illustration of the (a) Heitler model for an electromagnetic and (b) Heitler-Matthews model for a hadronic cascade. The production of new particles in electromagnetic showers is realized by either bremsstrahlung or pair production, while pions are produced in the hadronic component. Neutral pions in the hadronic cascades initiate further electromagnetic cascades by decaying into gamma rays. Figure taken from Ref. [37].

Extensive air showers are categorized into electromagnetic and hadronic cascades depending on the primary particle type which initiated the shower. Electromagnetic showers are produced by a gamma ray, whereas hadronic showers are produced by nuclear interactions. In the scope of this thesis, only hadronic showers are of interest.

The physics and energy at each interaction step within extensive air showers can be simplified by the Heitler-Matthews-Model [37], shown in Fig. 2.5b. It is a modification of the Heitler model [38] for electromagnetic cascades in which a gamma ray disintegrates into an electron and positron in an interaction with an atmospheric nucleus: $\gamma \rightarrow e^+e^-$ (Fig. 2.5a). When a proton interacts with air nuclei in the atmosphere in a hadronic interaction, pions are created from which $^2/_3$ of the initial energy is transferred to the initiated hadronic cascade by the creation of charged pions $\pi^\pm$, and the remaining fraction is transferred to neutral pions π^0. These decay into gamma rays ($\pi^0 \rightarrow \gamma\gamma$), initiating an electromagnetic cascade. New particles, such as positrons e^+ and electrons e^-, are produced by bremsstrahlung or pair production. In each epoch, a substantial fraction of the extensive air shower induces an additional electromagnetic cascade. The energy budgets in the hadronic E_hadr and electromagnetic E_em components can be derived from the initial energy E_0 of a proton primary:

$$E_\text{hadr} = \left(\frac{2}{3}\right)^n \cdot E_0 \text{ and } E_\text{em} = \left[1 - \left(\frac{2}{3}\right)^n\right] \cdot E_0. \tag{2.7}$$

This scheme is repeated until the interaction length (Equ. 2.10) of the parent pions becomes larger than the decay length (Equ. 2.11), and the pions subsequently decay into muons and neutrinos, which can reach ground level. For simplicity, only pions are considered in this model, rather than a contribution from other hadrons to the extensive air shower development. The Heitler-Matthews model describes only showers initiated by a proton primary, as it is independent of the primary mass. A description for heavier primaries can be derived by a superposition model, described in Ref. [39].

2.3.3 Cascade Equations

The longitudinal propagation of particles in extensive air showers through the atmosphere can be described by the cascade equations, a set of coupled differential equations. The development of the shower component is given by:

$$\begin{aligned}\frac{\mathrm{d}N_i(E_i, X)}{\mathrm{d}X} &= -\frac{N_i(E_i, X)}{\lambda_i} - \frac{N_i(E_i, X)}{d_i} \\ &\quad + \sum_{j=i}^{J} \int_E^\infty \frac{F_{ji}(E_i, E_j)}{E_i} \frac{N_j(E_j, X)}{\lambda_j} \mathrm{d}E_j. \qquad (2.8) \\ & \qquad (2.9)\end{aligned}$$

$N_i(E_i, X)\mathrm{d}E_i$ denotes the flux of the particle species i. The first two terms describe reinteraction and decay respectively, the last term describes the creation of new particles. λ_i is the interaction length in air, d_i the decay length, both measured in $\mathrm{g\,cm^{-2}}$. The function $F_{ji}(E_i, E_j)$ represents the particle yield of a particle of energy E_i produced by a collision of a particle of energy E_j with an air nucleus [12]. The interaction length is given by

$$\lambda_i = l_i \rho = \frac{\rho}{n_A \sigma_i^{\mathrm{air}}}, \tag{2.10}$$

with the number density of a given nuclear species n_A and the cross section for the interaction with air σ_i^{air}. The density of the atmosphere cancels in Equ. 2.10, and the interaction length is independent of the atmospheric density. In contrast, the decay length is defined as

$$d_i = \rho \gamma c \tau_i, \tag{2.11}$$

with the Lorentz factor γ, the speed of light c, and the lifetime τ_i of the particle. No explicit source term for the production of particles from the decay of other particles exists in the cascade equations. Another limitation is the neglect of ionization losses in the air.
Inclusive lepton fluxes can be calculated by solving the cascade equations for a respective particle species. The solutions of the set of coupled equations can be approximated semi-analytically, as described in Ref. [12]. Atmospheric lepton spectra can be derived from the solutions in the subsequent form:

$$\Phi_l(E) = \frac{\Phi_N(E)}{1 - Z_{\mathrm{NN}}} \sum_{i=\pi,\mathrm{K},\ldots} \frac{Z_{\mathrm{N},i,\gamma} Z_{i\to l,\gamma}}{1 + B_i E \cos(\Theta)/\epsilon_{\mathrm{crit},i}}. \tag{2.12}$$

$\Phi_N(E)$ denotes the flux of the CR primary, and $\epsilon_{\mathrm{crit},i}$ the critical energy of parent meson of species i at which decay (Equ. 2.11) and interaction length (Equ. 2.10) are equal. Z-factors are defined as weighted moments towards the CR spectrum displaying interaction and decays of the respective particles:

$$Z_{\mathrm{N}i} = \int_0^1 \mathrm{d}x_{\mathrm{lab}} x_{\mathrm{lab}}^{\gamma-1} \frac{\mathrm{d}N_{\mathrm{N}\to i}}{\mathrm{d}x_{\mathrm{lab}}}. \tag{2.13}$$

The moments govern the hadronic interaction processes between the individual particles, further elaborated in the subsequent section. The parameters of Equ. 2.12 are explained in Section 2.4.3 in more detail. The calculations can be found in Ref. [12, 40].

The cascade equations can be expressed in a matrix representation described in detail in Ref. [41]. The set of equations can be solved numerically by the Python package MCEq [7]. Different hadronic, CR composition and atmospheric models allow for the calculation of inclusive lepton fluxes and for the determination of uncertainties associated with the model selections.

2.3.4 Hadronic Interactions

As explained in the previous section, the primary CR and the initiated hadrons undergo hadronic interactions within extensive air showers. Hadrons define a subclass of particles, such as mesons and baryons, composed of quarks [42]. They are bound together by the strong force, opening up the field of quantum chromodynamics. Hadronic interactions describe the interaction of quarks within the interacting hadrons by the exchange of gluons, the mediators of the strong force. The particle production at high energies is subject to large uncertainties and cannot be accurately calculated. Therefore, hadronic interactions are modeled by different approaches and approximated at the highest energies. The following four models are used in this dissertation. The numbers indicate the model versions:

- Sibyll2.3c [3] is a model optimized for the simulation of extensive air showers, and yields the most commonly used model for lepton flux calculations and simulations in the atmosphere. It is based on the Dual-Parton-Model (DPM) [43]. The here presented version includes interactions of charm quarks within shower cascades, allowing for the calculation of prompt leptons (see Section 2.4.3). One caveat is that heavy ion collisions in colliders cannot be described by this model.

- EPOS-LHC [44] addresses the described lack of description of heavy ion collisions and is only developed from accelerator data from the Large Hadron Collider (LHC). The model is mostly used in particle physics.

- QGSJet-II-04 [45] is developed from the Quark-Gluon-String Model (QGS) [46], an analogous approach to the DPM. *Jet* refers to the description of collimated particle beams and the description of the resulting particles in the final state. The model is tuned to describe the development of extensive air showers, but and has only a few tuning parameters.

- DPMJet-III-3.0.6 [47] is based on Dual-Parton-Model, similar to Sibyll, and the Quark-Gluon-String Model. It is often used in the context of accelerator data.

2.4 Neutrinos

Neutrinos were first postulated by Wolfgang Pauli in 1930 to account for the missing fraction of energy in beta decay. Three decades later, neutrinos were detected in inverse beta decay experiments [48]. Presently, neutrinos are important messengers in particle and astroparticle physics, as certain characteristics violate the principles of the Standard Model and they propagate on a straight path from their source. This section illustrates the main properties of the neutrino, discusses the energy spectrum, implications of possible sources, and their production mechanisms.

2.4.1 Characteristics

Neutrinos are massless elementary particles in the Standard Model. As they do not carry an electric charge, they can propagate over cosmic distances through the Universe, without being deflected by intergalactic magnetic fields. This attribute makes them excellent messengers for the study of cosmic objects. Their small cross section for interaction with matter allows them to escape the dense source environments. Consequently, huge detectors are required to detect them. Neutrinos appear in three flavors, defined by their leptonic counterparts: the muon neutrino ν_μ, the electron neutrino ν_e, and the tau neutrino ν_τ. Neutrinos are produced in astrophysical objects within hadronic processes (see Section 2.3.4). Inelastic collisions of high-energetic protons with matter produce charged and neutral pions at equal probabilities, for instance:

$$\begin{aligned}
&p + p \to p + p + \pi^0 \\
&p + p \to p + n + \pi^+ \\
&p + p \to p + p + \pi^+ + \pi^- .
\end{aligned} \tag{2.14}$$

All three types of pions immediately decay via the following processes with a branching ratio of $\geq 98.8\%$ [49]:

$$\begin{aligned} &\pi^0 \rightarrow \gamma + \gamma \\ &\pi^+ \rightarrow \mu^+ + \nu_\mu \text{ and } \mu^+ \rightarrow e^+ + \bar{\nu}_\mu + \nu_e \\ &\pi^- \rightarrow \mu^- + \bar{\nu}_\mu \text{ and } \mu^- \rightarrow e^- + \nu_\mu + \bar{\nu}_e. \end{aligned} \tag{2.15}$$

The decay of neutral pions creates gamma rays which can be simultaneously detected with neutrinos from the same source. Equ. 2.15 indicates that the flavor composition at an astrophysical source becomes $\nu_e : \nu_\mu : \nu_\tau \approx 1 : 2 : 0$. However, a flavor ratio of $\nu_e : \nu_\mu : \nu_\tau \approx 1 : 1 : 1$ is measured at Earth [50]. The difference in flavor compositions indicates that neutrinos oscillate between flavor states from an astrophysical source toward Earth. The ability to oscillate between different flavor states implies that the neutrino carries a small non-zero mass. Current measurements from the KArlsruhe TRItium Neutrino (KATRIN) experiment constrain the neutrino mass to $< 0.9\,\mathrm{eV}$ [51]. Up to now, only an upper limit for the mass can be determined, but not the measurement of individual masses.

2.4.2 Energy Spectrum

The neutrino energy spectrum spans over 24 orders of magnitude in energy and originates from several different types of sources. Fig. 2.6 shows different proposed and estimated source classes with respect to energy. The low energy tail from µeV to meV is expected to be dominated by cosmological neutrinos, the neutrino counterpart of the CMB at $1.9\,\mathrm{K}$ [53], which has not been observed yet. At higher energies above keV, the neutrino spectrum is dominated by neutrinos from electron capture and other processes within stars and supernova remnants, for instance from the Sun [54] and from the supernova SN1987A [55]. The energy range accessible to neutrino telescopes includes atmospheric neutrinos produced in extensive air showers, astrophysical neutrinos from sources such as Active Galactic Nuclei, and cosmogenic neutrinos from proton interactions with the CMB [56]. However, the latter component has not yet been observed due to the enormous detection volumes required for the detection of ultra-high-energy neutrinos.

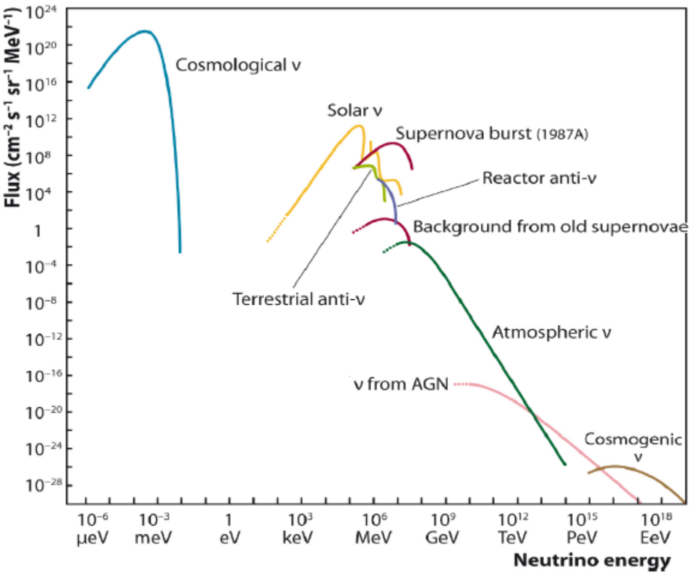

Figure 2.6: Expected neutrino flux for different source categories, taken from Ref. [52].

2.4.3 Atmospheric Component

The majority of neutrinos detected by the IceCube Neutrino Observatory (see Chapter 3) are produced in extensive air showers (see Section 2.3). Since only muon neutrinos will be regarded in this work, the atmospheric electron neutrino spectrum will not be discussed in the scope of this thesis.

The atmospheric neutrino spectrum in Fig. 2.8 calculated by MCEq shows the contribution of different hadrons to the total muon neutrino flux. The spectrum can be separated into two components by a change in spectral index. The low energy tail of the spectrum below $\sim 100\,\mathrm{TeV}$ is dominated by the conventional component, composed of neutrinos from decays of kaons and pions:

$$\begin{aligned} \pi^{\pm} &\rightarrow \mu^{\pm} + \nu_{\mu} \,/\, \bar{\nu}_{\mu} \\ K^{\pm} &\rightarrow \mu^{\pm} + \nu_{\mu} \,/\, \bar{\nu}_{\mu}. \end{aligned} \tag{2.16}$$

Both parent mesons are produced in the interaction of a CR primary (see Section 2.3). Almost the entire conventional component is dominated by kaon decay, whereas pion decay has only a small contribution to the total flux below 100 GeV.

The analytic approximate solution for the differential conventional neutrino flux of the cascade equation (Equ. 2.9) is given by integrating over the neutrino production yield $P(E_\nu, \Theta^\star, X)$ from a given CR primary flux Φ_N of nucleon N, derived from Equ. 2.12 [12]:

$$\begin{aligned}\Phi_\nu(E_\nu, \Theta^\star) &= \Phi_\mathrm{N}(E_\nu) \\ &\times \int\limits_0^{X_\mathrm{ground}} \left(\frac{A_{\pi\to\nu}(X)}{1 + B_{\pi\to\nu}(X) \cdot \frac{E_\nu \cos(\Theta^\star)}{\epsilon_\pi(T(X))}} + \frac{A_{K\to\nu}(X)}{1 + B_{K\to\nu}(X) \cdot \frac{E_\nu \cos(\Theta^\star)}{\epsilon_K(T(X))}} \right) \mathrm{d}X.\end{aligned} \tag{2.17}$$

The numerators $A_{i\to\nu}$ contain the production yields and branching ratios of the respective decay of parent meson i, the factors $B_{i\to\nu}$ in the denominator represent the cross section for the interaction of the parent mesons and nucleons. $\Theta^\star$ denotes the zenith angle at the point of neutrino production as a function of the observed zenith angle Θ. Both angles can be converted into one another by simple geometry, as illustrated in Fig. 2.7:

$$\frac{R_\mathrm{E}}{\sin(\Theta^\star)} = \frac{R_\mathrm{E} + H_\mathrm{int}}{\sin(\Theta)}. \tag{2.18}$$

The critical energies ϵ_i for each respective parent meson denote the energy at which the decay length (Equ. 2.11) is approx. equal to the interaction length (Equ. 2.10):

$$\epsilon_i = T(X) \cdot \frac{Rc}{Mg} \frac{m_i}{\tau_i}. \tag{2.19}$$

The ideal gas constant is denoted as R, M is the molar mass, g the gravitational acceleration constant, c the speed of light, and m_i the mass and τ_i lifetime of the parent particle. The denominator in Equ. 2.17 describes the competition between decay and reinteraction of the parent meson governed by both decay and interaction length. The neutrino flux is dominated by the direct decay of the parent mesons below $E_\nu \cdot \cos(\Theta^\star) < \epsilon_i$, where the neutrino flux follows the same power law as the primary CRs. Beyond the critical energy reinteractions dominate.

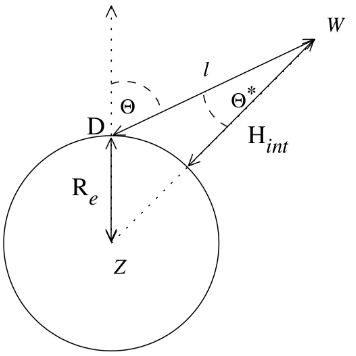

Figure 2.7: Relation of the zenith angle $\Theta^\star$ at production to zenith angle Θ in IceCube coordinates. Figure taken from Ref. [57].

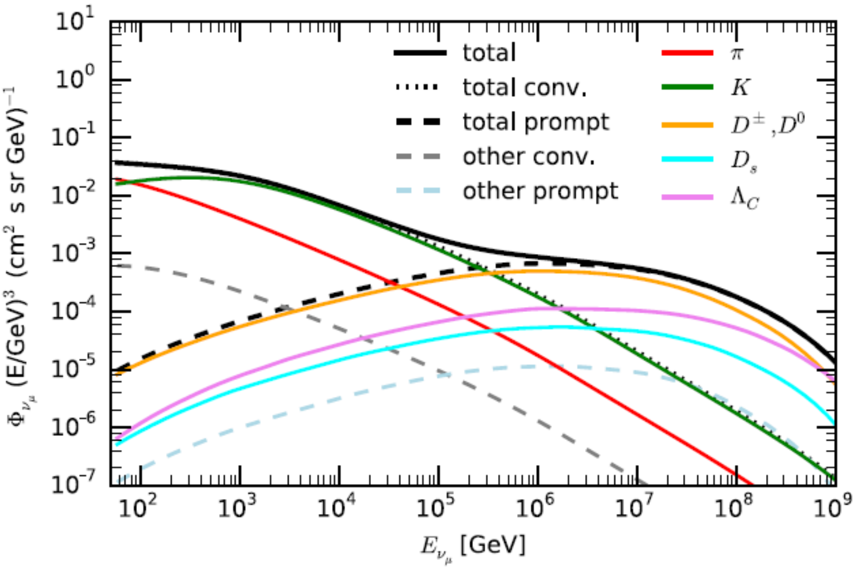

Figure 2.8: Atmospheric muon neutrino flux and the contribution of parent particles to the total flux, calculated by MCEq [7] with Sibyll2.3c as the hadronic interaction model, H3a as the parameterization of CR composition, and the US Standard Atmosphere [58] for the modulation of the atmospheric depth profiles. Figure taken from Ref. [7].

Low energy cascades can be initiated in this interaction, or the parent mesons can decay into neutrinos and muons, and the neutrino flux becomes approximately one power steeper than the primary CR flux. This characteristic is derived by solving the cascade equations (Equ. 2.9) with a different spectral index for the low and high energy regime. Since the critical energy is dependent on atmospheric temperature, the spectral change can be shifted towards lower and higher energy concerning temperature changes in the atmosphere, making the spectral change season-dependent.

The high energy tail above $\sim 100\,\text{TeV}$ is dominated by the prompt component. The prompt component consists of neutrinos from decays short-lived particles, for instance, D-mesons. These parent particles cannot interact and immediately decay since the decay length is large compared to the interaction length (refer to Equ. 2.11 and 2.10). As the decay of the parent particle dominates, the spectrum of prompt neutrinos is expected to follow approximately the spectrum of the CR primary [12]. The shift in the spectral index according to a change in the major contribution of parent particles to the total atmospheric neutrino flux is mirrored in the solutions of the cascade equations. The second term in the denominator in Equ. 2.12 diminishes and the spectrum of dominated by the shape of the primary flux. Prompt neutrinos have not yet been observed, which is on the one hand due to their low abundance. The branching ratios to produce their parent particles are small, as are the branching ratios for them to decay into neutrinos [59]. On the other hand, it is extremely difficult to distinguish prompt neutrinos from a neutrinos of astrophysical with similar energies. Neutrinos of the same flavor induce the same signature in the detector so that the differentiation between the origin is based on the direction and veto techniques (see Chapter 3.3 and 5).

2.5 Seasonal Variations

The critical energy at which the reinteraction and decay probability of the parent meson are equal is linearly proportional to the atmospheric temperature, as discussed in the previous section. Therefore, the critical energy becomes inversely proportional to the atmospheric density under the assumption that the atmosphere is an ideal gas. The temperature in the stratosphere remains mostly constant per altitude except for Sudden Stratospheric Warming (SSW) at high latitudes [60], in which the temperature increases rapidly. Day-to-day temperature variations are negligible. However, seasonal temperature changes lead to a seasonal variation in the critical energy (Equ. 2.19) and a corresponding variation in the neutrino flux compared to the annual average. This dependence was first proposed in Ref. [61]. When the temperature increases, the atmosphere expands, which causes a decrease in its density. Simultaneously, the parent decay probability increases and the reinteraction probability decreases, leading to an enhanced production of neutrinos and muons. Conversely, during winter, the temperature falls and the reinteraction probability dominates in the cold and dense atmosphere.

2.5.1 Muons

The seasonal variation for muons was first measured in 1954 in Ref. [62], among many other experiments, such as Ref. [63, 64, 65, 66]. Previous studies by IceCube and its predecessor, theAntarctic Muon And Neutrino Detector Array (AMANDA), among others, have demonstrated the correlation between muon rate variation and the variation of the effective atmospheric temperature T_{eff} at first order [67, 68, 69] by a linear correlation coefficient α:

$$\frac{R(t) - \langle R \rangle}{\langle R \rangle} = \alpha_{\text{T}} \cdot \frac{T_{\text{eff}}(t) - \langle T_{\text{eff}} \rangle}{\langle T_{\text{eff}} \rangle}. \tag{2.20}$$

The latest IceCube measurement found a correlation coefficient of $\alpha_{\text{T}} = 0.7500 \pm 0.0027$ [70], as displayed in Fig. 2.9.

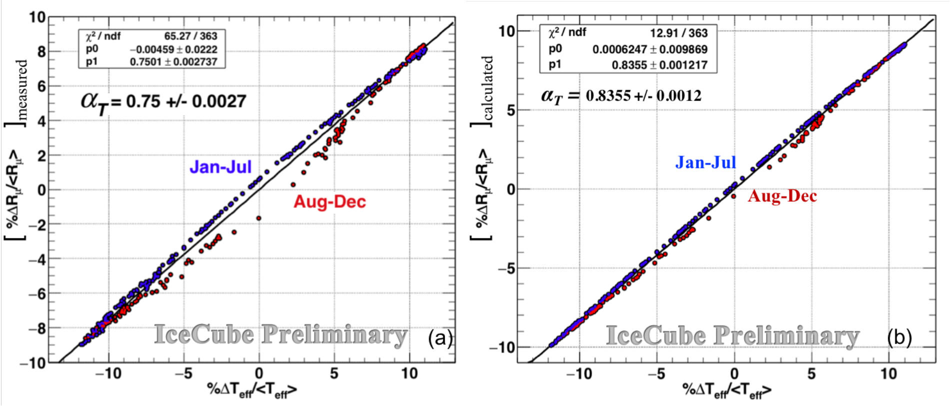

Figure 2.9: (a) Measured, and (b) calculated correlation coefficient between muon rate and effective temperature. Figure taken from Ref. [70].

2.5.2 Neutrinos

The correlation coefficient between the variation in neutrino rate and temperature was measured by AMANDA [71] and IceCube, with significance of more than 10σ [72, 1]. The latest measurement obtained a correlation coefficient of $\alpha = 0.347 \pm 0.029$ (see Equ. 2.20), which is incompatible with model predictions [1]. While the neutrino rate varies, the seasonal variations are expected to increase with the energy of the particle.

Fig. 2.10 displays the predicted seasonal variation at the South Pole between the austral summer from December to February and the winter from June to August for muon and electron (anti-)neutrinos from a zenith region from 90° to 120° [74]. The calculation is based on the empirical atmospheric model NRLMSISE-00 [4], described in detail in Appendix D. The deviation of seasonal flux from the annual mean exponentially increases above 100 GeV in muon neutrinos, reaching an

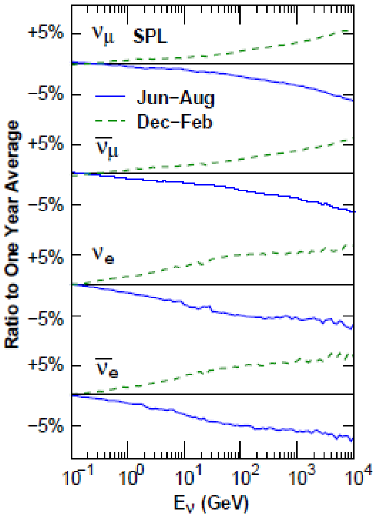

Figure 2.10: Ratio of the calculated neutrino flux for austral summer and winter to the annual average at the South Pole for zenith angles between 90° to 120° compared to the yearly average. Figure taken from Ref. [73].

amplitude of ±5% at 10 TeV. This increase in variation strength can be attributed to the increase in interaction height and cross section. Higher energy neutrinos are produced by CR primaries of higher energy that interact at higher altitudes in the atmosphere, where the temperature variations are larger (see Fig. 8.1). Besides that, higher energetic mesons have a longer decay length and therefore, the produced neutrinos show a larger seasonal variation.

The seasonal variation in the atmospheric neutrino flux is expected to occur only in the conventional component. This is because prompt neutrinos arise from parent mesons with a short lifetime. The experiments measure the total neutrino flux, which is a combination of atmospheric and sub-dominant astrophysical neutrino flux components in the energy range of interest in this dissertation between 125 GeV to 10 TeV. Fig. 2.11 shows the expected seasonal flux deviations to the annual average for austral summer and winter by MCEq. H3a is used as the primary composition, Sibyll2.3c as the hadronic interaction model, and NRLMSISE-00 as the atmospheric modulation. The solid lines indicate the prediction for the conventional atmospheric flux, and the dashed lines indicate the total flux including the prompt component. Despite the infinitesimal deviation between the total (conventional and prompt) and conventional seasonal flux ratios, the ratio of the conventional and prompt flux decreases above approximately 20 TeV. The ratio of seasonal to annual average flux is maximal around 50 TeV for the total flux and decreases with energy as the contribution of the prompt component increases (see Fig. 2.8). The seasonal to annual average flux

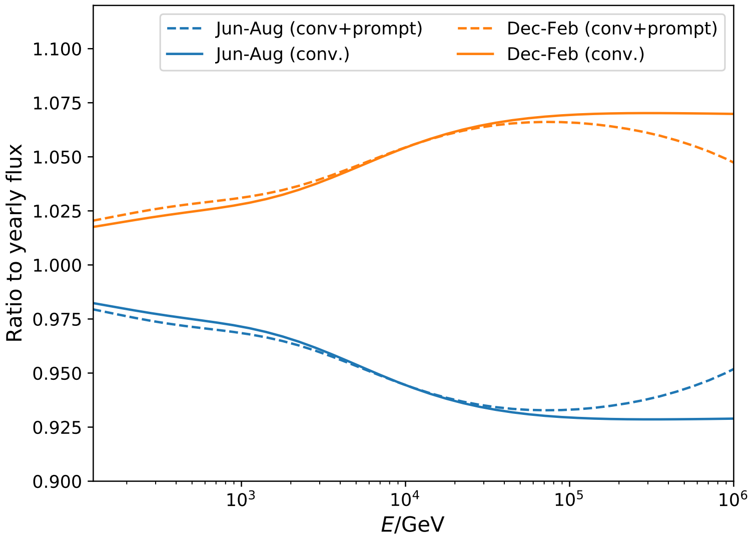

Figure 2.11: Ratio of seasonal muon neutrino flux to the annual average calculated with MCEq (H3a as primary CR composition, Sibyll2.3c as hadronic interaction model and NRLMSISE-00 as atmospheric model) for austral summer and winter. Dashed lines depict the total flux including the prompt component, solid lines depict the conventional atmospheric flux component only.

ratio for the conventional component reaches its maximum variation strength only at 100 TeV.

3 The IceCube Neutrino Observatory

Enormous volumes are required for the detection of astrophysical and atmospheric neutrinos due to their low probability of interaction with matter. State-of-the-art neutrino telescopes use transparent media such as water or ice as detection volume. These telescopes utilize the photoelectric detection of Cherenkov radiation, which is emitted by charged particles from neutrino interactions with matter during propagation through the detector [52]. The IceCube Neutrino Observatory is the largest neutrino detector with an instrumented volume of 1 km^3 within the antarctic ice shield, the successor of AMANDA[75].

3.1 Detector Design

The entire detection array consists of 86 cable strings, each of them equipped with Digital Optical Modules (DOM) at depths between 1450 m to 2450 m in a 17 m vertical spacing [76]. 78 strings of the main array are arranged on a hexagonal grid with a horizontal distance of 125 m. The *DeepCore* component [77] comprises of eight innermost strings deployed at a lower distance, forming an infill array at a distance of only 75 m. This configuration features DOMs with higher quantum efficiency, allowing for a lower energy threshold of 10 GeV in combination with the reduced string spacing compared to 100 GeV for the main array. The DOMs of the infill array are positioned between 1750 m to 1850 m and 2100 m to 2450 m in ice with highly transparent optical properties. The ice layer in between is referred to as the *dust layer*, where the presence of dust grains enhances scattering effects within the ice. The lower energy threshold enables DeepCore to explore neutrino oscillations and low-energy phenomena, such as the search for new particle signatures beyond the Standard Model. At an altitude of 2835 m, an additional detector component, known as *IceTop*, is located on the ice surface. The IceTop array is composed of 81 surface stations arranged in the same grid as the in-ice detector. Each station contains two tanks spaced 10 m apart, each

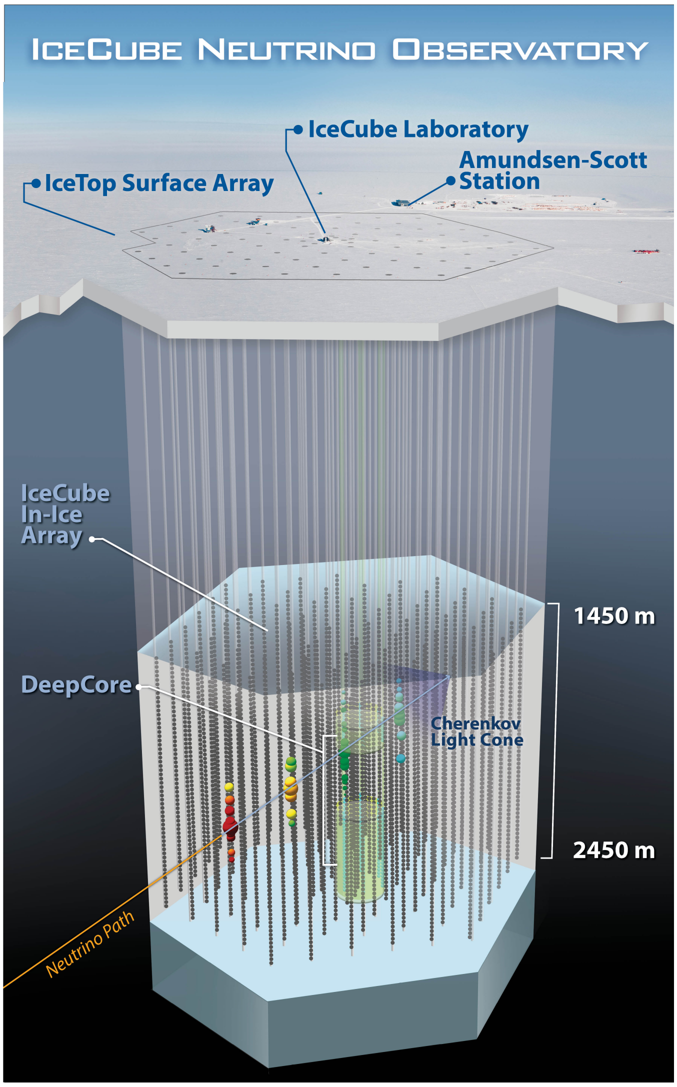

Figure 3.1: Illustration of the IceCube Neutrino Observatory and its detector components including an incoming neutrino event. Each colored sphere represents a DOM which detected the emitted Cherenkov light. The size correlates with the charge deposit. The color represents the timing information. Red corresponds to early hit DOMs, blue to late. Figure taken from Ref. [11].

housing two DOMs. The primary objective is to simultaneously detect air showers, which allows for the detection of coincident events with the in-ice detector. IceTop is often used as a veto to detect the air shower counterpart of an atmospheric neutrino of an in-ice event. Another goal is to examine air shower parameters to determine the mass composition of cosmic rays and their energy spectrum. The altitude is distinctive in comparison to other experiments and facilitates a measurement near the maximum shower development. An illustrated overview of the individual detector components is provided in Fig. 3.1.

Each optical module encloses a downward-facing photomultiplier tube (PMT) of 25 cm diameter inside a spherical glass sphere for protection against increasing pressure with increasing ice-depth [78], as depicted in Fig. 3.2. The signal from the PMT is digitized and amplified on a main board before transmission via cable strings to the IceCube Lab (ICL) at the surface. For pulse calibration, every DOM includes an LED. The detector deployment was finished in 2010. However, data acquisition began in May of the subsequent year incorporating the newly installed strings into the data acquisition system.

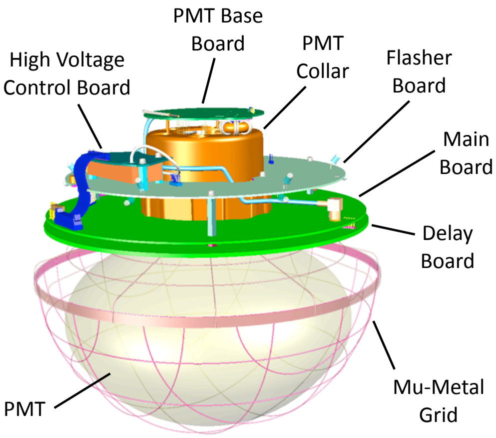

Figure 3.2: Illustration of an optical module and its components. Figure taken from Ref. [5].

An extension towards the next-generation neutrino telescope *IceCube-Gen2* [79] is currently in planning stages. This extension will increase the detection volume to 10 km^3 by incorporating additional in-ice strings, enhancing the IceTop array using scintillation detectors, and introducing an in-ice radio array to exploit the detection ability of very-high-energy neutrinos beyond PeV energies, where the Earth is opaque to neutrinos.

3.2 Detection Principle

As neutrinos cannot be detected directly, neutrino telescopes utilize an indirect method of detecting them via Cherenkov emission of secondary particles. If the velocity of charged high-energy particles traveling through an optically transparent dielectric medium is greater than the speed of light in the medium, they emit Cherenkov light along their path. When a neutrino interacts in the ice or near the bedrock, energy is deposited in the detector, and secondary charged particles are produced. Cherenkov radiation is emitted by the secondaries in a conical shape with an opening angle of

$$\Theta_C = \arccos\left(\frac{1}{\beta n}\right) \tag{3.1}$$

at first order with the particle velocity $\beta = {}^{v}/_{c}$ in units of the speed of light and the refractive index n [80]. The emitted photon spectrum is wavelength-dependent with λ^{-2} [81], and peaks in the blue spectrum of visible light. The emitted Cherenkov photons are detectable through single photon hits within the DOMs. The accumulation of coincident local photon hits and timing information is used to reconstruct the energy and direction of the neutrino as described in Section 3.6. Fig. 3.3 shows an illustration of the different event signatures in IceCube and the emission of Cerenkov light, further explained in the next section.

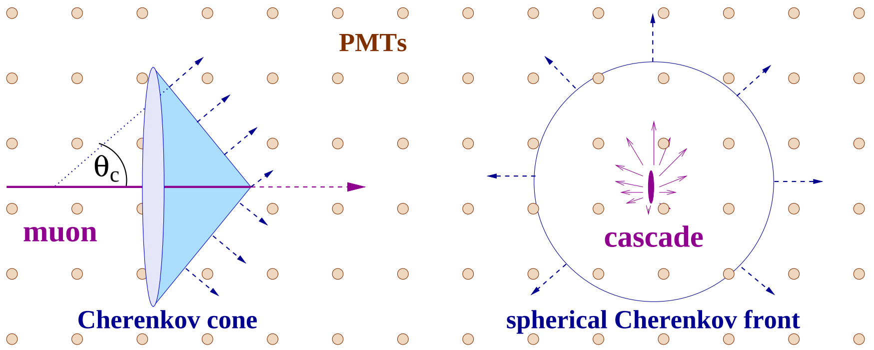

Figure 3.3: Illustration of a particle traversing the detector initiating Cherenkov light. The left side shows a track-like signature of an incoming muon, which emits Cherenkov light in a cone-like shape. The right side depicts a cascade event, in which Cherenkov light is emitted in a spherical cone. Figure taken from Ref. [52].

3.3 From Neutrino Interaction to Event Signatures

Neutrinos with energies above 10 GeV interact with the detection medium by deep inelastic scattering at the quarks inside the nucleon via the weak force [82]. This interaction can take place in two distinct processes. In the case of a Charged-Current (CC) interaction [83], the neutrino transforms into a lepton by exchanging a Z boson, and the energy is transferred to the nucleus. Consequently, a hadronic cascade X is generated at the interaction vertex: $\nu_l + N \rightarrow l + X$. Neutral-Current (NC) interactions arise from the exchange of a neutral Z^0 boson, resulting in energy deposition within a hadronic cascade: $\nu_l + N \rightarrow \nu_l + X$.

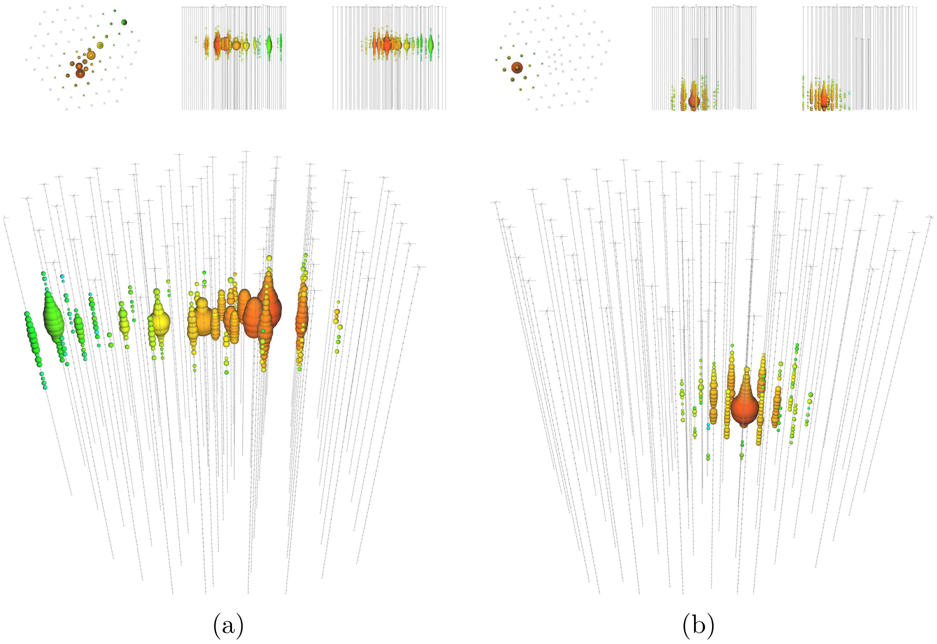

Figure 3.4: Illustration of two events from Ref. [84]: (a) track signature, (b) hadronic cascade. The size of the DOMs represents the detected charge. Red denotes early, green late hits.

The main event signatures in IceCube consist of hit patterns that are track- or cascade-like. When muons, either from atmospheric air showers or from CC ν_μ interactions, propagate through the ice, Cherenkov radiation is emitted in a mostly linear trajectory. The related hit trajectory along the modules in the detector is designated as a track event, illustrated in Fig. 3.4(a). Track signatures starting within the detector are a result of neutrino interactions within the detection volume while stopping tracks are expected to originate from low-energy muons. A stopping track represents a muon that lost suddenly the most energy so that the muon has a lower energy than the detection threshold of IceCube. Sudden large energy losses are often attributed to atmospheric muons, whereas the probability of these sudden losses is low for a neutrino-induced muon [85]. Cascade events are identified as spherical emissions of Cherenkov light initiated by a hadronic cascade from CC ν_e and NC interactions of all flavors [52], as illustrated in Fig. 3.4(b). A unique signature originates from the CC interaction of ν_τ. The production of two cascades, referred to as double cascades, arises from the τ production by ν_τ and from the subsequent τ decay into a hadronic or electromagnetic cascade [86].

3.4 Data Acquisition and Processing

An IceCube event is defined as the occurrence of multiple simultaneous hits within the detector [87]. A hit refers to a measured charge above a trigger threshold of 0.25 photoelectron (PE) at a PMT [78]. The waveform, quantified as the pulse shape initiated by the photons, is digitized in the DOM mainboard by either the Analog Transient Waveform Digitizer (ATWD) or the fast Analog to Digital Converter (fADC). Each DOM has two converters to account for another hit being recorded during signal conversion. Multiple concurrent hits are required to qualify as an IceCube event within a specified time frame. This condition is referred to as a trigger. The Simple Multiplicity Trigger (SMT) [5] is the most fundamental trigger, triggered when a minimum of N strings are hit by Hit Local Coincidence (HLC). HLC are hits with neighboring or the second nearest DOMs within a few µs. In the scope of this thesis, an event is saved when the SMT-8 trigger is fulfilled.

The collected data is reduced to 100 GB per day to be transferred to the data storage in the Northern Hemisphere, where event reconstruction algorithms are performed offline. The remaining data tapes are transported from the Pole once per year [5]. The processing sequence from raw data to high-level attributes is categorized into five steps, referred to as processing *Level*. Level 0 signifies the processing of waveforms into an event via detector triggers. Level 1 is a preprocessing stage for pulse cleaning and reduction of background noise. It includes the preliminary fit of the track through the detector, such as LineFit [88] and Likelihood Fit (LLHFit) [89]. All processing stages up to Level 2 are performed directly at the Pole. Level 2 comprises the basic reconstruction pipeline explained in Section 3.6. Finally, Level 3 is an offline processing running working group-specific reconstructions and cleaning filters. Levels 4 and 5 focus on the selection of a specific event hypothesis and background reduction for a particular analysis. These two steps generate the necessary high-level features for the analysis at hand.

3.5 Simulation Chain

The IceCube simulation chain consists of simulations of the atmospheric muon background produced by air showers, the neutrino interactions in the ice, and the propagation of their leptonic counterparts through the detector, the propagation of Cherenkov photons through the ice, as well as simulations of the recorded signal and the detector electronics.

Neutrino events in IceCube need to be generated with Monte Carlo Simulation (MC) methods. The interactions of neutrinos and the propagation of the induced lepton are probabilistic. The nondeterministic processes can be described by random sampling from one interaction to another by MC simulations. The software Neutrino Generator (NuGen) is employed for this purpose, described in Ref. [90]. This framework has been adapted from the All Neutrino Interaction Simulation (ANIS), as reported in Ref. [91]. The neutrino energy at the surface is sampled from a predefined distribution, forcing the neutrino to interact in the vicinity of the detector. The simulation framework models the propagation of neutrinos to the detector and their interactions within the ice [90]. The latest version of NuGen serves as a successor to the C++ Neutrino Simulation (NuSim) [92] and has been integrated into the IceCube software *IceTray* [93].
The simulation framework COsmic Ray SImulations for KAscade (CORSIKA) [94] is used to simulate the muon background from atmospheric air showers. CORSIKA generates the interactions of various primary nuclei in the atmosphere and propagates the initiated particle interactions throughout the atmosphere to accurately describe extensive air showers.

The generated leptons, regardless of their origin, are propagated through the detector by the PRopagator with Optimal Precision and Optimized Speed for All Leptons (PROPOSAL) [95, 96]. This tool simulates energy losses, decay, and scattering of charged leptons in a medium. The initiated Cherenkov photons are simulated by `clsim` [97], which propagates the photons through the inhomogeneous South Pole ice.

3.6 Event Reconstruction

Various reconstruction techniques are employed in the IceCube processing chain to determine the direction of the neutrino and to estimate its initial energy from the measured pulses in the detector. These algorithms require a series of clean pulses, ideally free of any background noise. The standard reconstruction pipeline includes the following fits to the pulses from each DOM for reconstructing the neutrino-induced muon track: LineFit, LLHFit, SPEFit, MPEFit, and SplineMPE [98]. The previous fit is always used as a seed for the consecutive one to enhance the directional prediction in each sequence. Except for LineFit, all reconstructions rely on likelihood methods. Recent advancements in this field involve deep neural networks [99], with the advantage of combining several reconstruction steps into one. Since the latest methods were not accessible for the data selection utilized during the development phase of this dissertation, the reconstructed variables for the energy estimation in Chapter 6.3 rely on the track reconstruction SplineMPE.

SPEFit and MPEFit

The directional reconstruction of the induced muon is based on a maximum likelihood approach with the likelihood $\mathcal{L}(\vec{x}|\vec{a})$ as an objective function. The likelihood is minimized to obtain the optimal parameters $\vec{a}$ of a given track hypothesis for the measured data $\vec{x}$. Since the measured data are statistically independent, the likelihood can be expressed as the product of the probability density function (PDF) p of each event:

$$\mathcal{L}(\vec{x}|\vec{a}) = \prod_i \mathrm{p}(x_i|\vec{a}). \tag{3.2}$$

The path through the detector is approximated as an infinite line, along which the muon travels with the speed of light. The Cherenkov photons emitted scatter in the ice, causing a delay in their arrival time t_{observed}

in comparison to the direct line of sight between the track and DOM t_{expected}. The time difference between the two is defined as the time residual [100], as illustrated in Fig. 3.5:

$$t_{\text{residual}} = t_{\text{observed}} - t_{\text{expected}}. \tag{3.3}$$

The PDF from Equ. 3.2 can be expressed as the observed time residual as
$\mathrm{p}(t_{\text{residual},i}|\vec{a})$ given by the Pandel function [101]. This function is an attempt to describe the propagation of Cherenkov photons in the ice analytically. Two different approaches are used for calculating the conditional probabilities for each DOM, which define two distinct reconstruction algorithms.
The Single-Photoelectron (SPE) reconstruction calculates the PDF by taking into account only the first Cherenkov photon for each DOM. The first photon is usually the least scattered out of all arriving photons.
The Multi-Photoelectron (MPE) reconstruction considers the total number of hits n_i detected at each DOM in addition to the first hits [98]:

$$\begin{aligned}\mathcal{L}_{\text{MPE}}(\vec{x}|\vec{\Theta}) &= \prod_i \mathcal{L}_{\text{DOM}} \\ &= \prod_i^{\text{1st hits}} n_i \cdot \mathrm{p}(t_{\text{residual},i}|\vec{a}) \cdot \left(1 - \int_{-\infty}^{t_{\text{residual}}} \mathrm{p}(t_{\text{expected}}|\vec{a})\mathrm{d}t\right)^{n_i-1}.\end{aligned} \tag{3.4}$$

The likelihood describes the probability that the first of all hits at a DOM arrives within the defined time residual accumulated in the whole detector. Both methods show similar performance at energies below 10 TeV since they are equivalent if only one photon is detected per DOM. This scenario is realistic for low-energy events, which only have a few hits within the detector.

SplineMPE

The previous MPE-Fit reconstruction cannot account for the depth-dependent absorption and scattering in the ice due to the selected PDF. To address this, the successor SplineMPE employs a PDF based on B-splines [29] into Equ. 3.4, in which the probability of detecting photons from a muon track in different time windows is parameterized. Splines

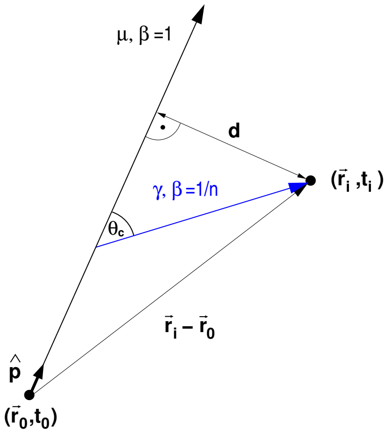

Figure 3.5: Illustration of the time residual defined for muon track reconstruction (Equ. 3.3). The muon emits a Cherenkov photon under the angle Θ_C, propagating to the nearest DOM at position $\vec{r_i}$. The photon is expected to arrive at time $t_i = t_{\text{expected}}$. Figure taken from Ref. [52].

are piecewise polynomial functions that can interpolate the propagation between different depths from photon tables. Further details can be found in Ref. [98]. However, SplineMPE has yet to account for the azimuthal anisotropy and tilt of the layers (see Chapter 7.2).

4 Selected Concepts of Machine Learning and Statistical Measures

Machine learning, a branch of artificial intelligence, is the development of algorithms and models that allow computers to learn from data to make predictions or decisions about new, unobserved data [102]. The data analysis process based on machine learning consists of four stages: data collection, training and optimization of an algorithm or model, validation of the model performance, and the application and evaluation of the model to unknown data. Machine learning can be supervised (where the model is trained on labeled data), unsupervised (using pattern recognition), or reinforcement learning (learning by experiment and experience). The classification algorithms that are used in this thesis fall into the category of supervised machine learning.

Predicting the class category of new data based on particular features of the dataset at hand is a common target addressed by this subcategory of learning algorithms. The quality of the classification is usually measured by a probabilistic quantity or loss function [103].

4.1 Tree-based Algorithms

Many machine learning classifiers rely on the concept of a Decision Tree (DT). Decision Trees are tree-like models that recursively divide the data into subsets based on the most important attributes or features for the classification. Fig. 4.1 shows the principle of a DT. At each data split, a decision node is created where an event is classified into one of the categories. This process is applied at each branch until the final classification has been made. The number of classes matches the number of leaf nodes. DTs are widely used algorithms, as they provide a trackable and human-readable decision-making path. The classification quality is determined by selecting the best suitable features (known as attributes) that are then used to construct the decision path at each node. The selection criterion for the classification is generally established by a measure of impurity [104]. This may include metrics

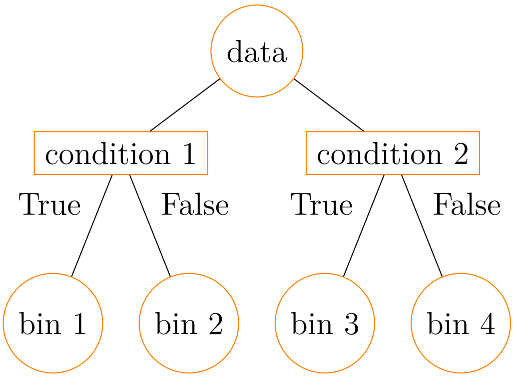

Figure 4.1: Illustration of a DT. The data is sorted into $n = 4$ categories (leaf nodes) along various decision paths.

such as the misclassification count, or entropy. The *Gini-Index* $i(N)$ [105, 106] is utilized as a measure in all algorithms presented in this thesis:

$$i(N) = \sum_{i \neq j} P(w_i)P(w_j) = \frac{1}{2}\left[1 - \sum_{j} P^2(w_j)\right]. \tag{4.1}$$

P denotes the fraction of category w_i and w_j, respectively. N signifies the node where the decision occurs. Trees that use the Gini index are known as Classification And Regression Tree (CART) algorithms [107]. The maximum number of branches along a decision path determines the depth of the tree. Although DTs are a commonly used algorithm, their output can be biased towards the training dataset, and the accuracy of predictions may suffer if the training and test data originate from slightly different distributions. This phenomenon is known as overfitting to the training set. The use of multiple trees in modified versions of the decision tree method results in improved performance and independence from the training dataset [108].

4.1.1 Random Forest

A Random Forest (RF) is an ensemble technique that utilizes multiple decision trees [104]. To create different DTs, the technique constructs several random subsets using *bootstrapping* [108]. New sub-samples are generated by sampling with replacement. The ultimate probability of the origin of each event from a specific leaf node is calculated by averaging over all trees [109]. Table 4.1 provides default parameters and their respective descriptions.

Parameter	Value	Explanation
`n_estimators`	100	number of trees
`max_features`	$\sqrt{N_{\text{features}}}$	observables for best split
`criterion`	Gini-index	quality measure for split
`max_depth`	unlimited	maximum tree depth
`min_samples_split`	2	minimum number of samples to perform split
`min_samples_leaf`	1	minimum samples to create a leaf node
`min_weight_fraction_leaf`	0	required sum of weights to create a leaf node
`max_leaf_nodes`	unlimited	maximum number of leaf nodes
`bootstrap`	True	different random sub-set for each tree
`min_impurity_decrease`	0	decrease of Gini-Index to create a split

Table 4.1: Definition and default settings of the parameters in the Random Forest classifier [109].

4.1.2 Extremely Randomized Trees

Closely related to RF, the Extremely Randomized Trees (ERT) concept [110] is an ensemble technique that adds more randomness to DT. ERT generate multiple trees similar to the RF, but a random subset of features is used to determine the best split at each node, instead of all features. Additionally, the ERT classifier selects feature splits from a random threshold within a predefined range.

4.1.3 Boosted Decision Trees

The integration of boosting into DTs creates ensemble methods with more stable and faster predictions than those composed of a single tree. The algorithms commence with a basic DT that undergoes progressive improvement through the generation of multiple, more complex trees. Misclassified events are associated with higher weights to impose sanctions on these nodes, while accurately classified events are assigned lower weights. The aim is to minimize the weighted error of the newly constructed tree during each iteration. This process continues until a predetermined stopping point is reached, generally a predefined number of iterations. The learning rate tracks the contribution of each tree to the final classification [108]. In this work, two frequently used methods are employed, which differ substantially in the definition of weighting.

AdaBoost

The Adaptive Boosting (AdaBoost) [111] algorithm assigns weights to data points in the training sample sequentially, updating them according to misclassifications in each iteration of the algorithm [112]. The method penalizes incorrectly classified events as outliers, making it sensitive to noisy data.

Gradient Boosting

The Gradient Boosting (GB) [113] algorithm aims to minimize the overall loss function instead of penalizing single misclassified events. Multiple trees are built independently in parallel, allowing GB to function as a fast and robust classifier.

4.2 Naive Bayes

Naive Bayes (NB) is a simple probabilistic machine learning classifier to estimate the class category with Bayes' theorem [114]:

$$P(y \mid x_1, ..., x_N) = \frac{P(y) \prod_{i=1}^{N} P(x_n \mid y)}{P(x_1, ..., x_N)}. \tag{4.2}$$

The conditional probability calculates the probability of a class category y_i based on a particular event x_n. An important aspect of this algorithm is its *naive* assumption that the features are conditionally independent, for instance, the absence of one feature does not affect the prediction based on the other features [115]. During the training phase, the frequencies of each class are used to calculate the prior probabilities $P(y)$ and the likelihoods of each feature within a given class. To classify new data, the posterior probability is calculated. The NB classifier has various variants determined by the assumptions about the feature distributions. The probability is represented by a Gaussian distribution, the Gaussian NB classifier [109], in this dissertation which can be expressed as

$$P(x_n \mid y) = \frac{1}{\sqrt{2\pi\sigma_y^2}} \cdot \exp\left(-\frac{(x_n - \mu_y)^2}{2\sigma_y^2}\right). \tag{4.3}$$

The mean of the population is given by $\mu \in \mathbb{R}$, and the standard deviation by $\sigma \in \mathbb{R}$.

4.3 Crossvalidation

k-fold cross-validation (CV) [108] serves as a performance measure of a machine learning model. Its primary purpose is the identification of optimal model settings without biased selection of training data. The training set is partitioned into k equal-sized subsets. The model is trained on $k-1$ of these, and the remaining subset is used for evaluation. The training subsets are then shifted iteratively to enable the use of all possible combinations as training data. The outcome is calculated as the mean of all classifications from the k sets. CV has the benefit of accounting for all available data efficiently by repeatedly employing different sections of the dataset for training and testing, thereby reducing bias towards selecting a particular training set. The typical number of divisions is often $k = 5$ or $k = 10$.

4.4 Wasserstein Distance

The Wasserstein Distance (WD), commonly known as the *Earth Mover's Distance*, quantifies the cost of transforming one distribution to another. The WD in this thesis is defined by the implementation found in Ref. [109, 116]:

$$l_1(u, v) = \inf_{\pi \in \Gamma(u,v)} \int_{\mathbb{R}\times\mathbb{R}} |x - y| \mathrm{d}\pi(x, y). \tag{4.4}$$

$\Gamma(u, v)$ in $\mathbb{R} \times \mathbb{R}$ is the set of all PDF over which the infimum is calculated for the distance between the two random variables x and y. π denotes the set of joint probabilities.

4.5 χ^2-Test

The χ^2-test is a statistical hypothesis test used to determine whether there is a statistically significant difference between the observed (measured) m_i and expected e_i number of frequencies:

$$\chi^2 = \sum_i \frac{(m_i - e_i)^2}{\sigma_i^2}. \tag{4.5}$$

σ_i denotes the respective uncertainties of the measured data. The test assesses two hypotheses: The first is the null hypothesis or the expected result that is chosen as the opposite of what is being examined. It assumes no association between two quantities. The second hypothesis is the alternative hypothesis or the observed result, which suggests an association between two variables. A hypothesis is rejected at a specific level of significance $1 - p$, specified by the corresponding p-value. The p-value measures the extremity or exceptionality of the observed data under the assumption that the null hypothesis is valid. It is calculated on a test statistic by computing the probability of observing a test statistic as or more extreme than the observed value. Generally, a predetermined level of significance is selected to decide when to reject the null hypothesis. If the p-value is less than the designated threshold, the null hypothesis can be rejected with a corresponding percentage [117].

5 Event Selection

Developing an event selection for atmospheric muon neutrinos is challenging due to the dominant background of atmospheric muons. The search for buried neutrino signatures can be compared to *finding a needle in a haystack*. The selection of events used in this work consists of muon neutrinos from track signatures in the detector, as introduced in Chapter 3.3. Besides distinguishing between atmospheric muons and neutrinos, the sample has to be cleaned from electron neutrino-induced cascades. The same event selection is utilized as in the seasonal variation analysis in Ref. [1] to ensure comparability.

5.1 The Diffuse Muon Neutrino Track Sample

The event selection is based on the diffuse muon neutrino sample developed by the IceCube group in Aachen. The sample is a standard event selection in IceCube for the extraction of muon neutrino-induced track events with a purity of 99.85%, where the remaining 0.15% is due to contamination by atmospheric muons [118]. The sample does not distinguish between muon neutrinos of atmospheric or astrophysical origin. A detailed overview of all selection steps is given in Ref. [119, 120]. This section describes the main aspects of the event selection in each processing step.

5.1.1 Variable Definitions

This section provides an overview of the variables utilized as cuts in the event selection.

- Q_{tot}: Total detected charge in PE in the detector.
- d_{Qavg}: Average distance from DOM to track weighted by charge q_i of each DOM:

$$d_{\mathrm{Qavg}} = \frac{1}{Q_{\mathrm{tot}}} \sum_{i \in \mathrm{DOMs}} q_i \|\vec{x_i} - \vec{p}\|_{\mathrm{min}}. \tag{5.1}$$

- n_{dir} & l_{dir}: Both variables are defined based on *direct hits*, which signify unscattered photons detected in the time residual from Equ. 3.3 (see Fig. 3.5). The time residual is defined in five different intervals indicated by capital letters `A` through `E`. In the following event selection, hits are counted in the time interval from $[-15\,\text{ns}, 250\,\text{ns}]$. The number of identified hits during this time window is denoted as n_{dir}, and l_{dir} is the calculated track length in the detector derived from these hits.

- s_{dir}: Smoothness of the reconstructed track from direct hits can be quantified as in Ref. [121]:

$$s_{\text{dir}} = \max_j \frac{j-1}{N-1} - \frac{l_j}{l_N}. \tag{5.2}$$

The projected distance from the track to the j-th closest DOM is denoted as l_j, the and the number of direct hits N. The smoothness measures the consistency of the observed hit pattern with constant Cherenkov light emission by a muon by performing a Kolmogorov-Smirnov consistency test. A track with equally distributed hits corresponds to $S \sim 0$. Events with clustering of hits at the beginning or end of a track reach a smoothness close to $S \pm 1$.

- $\overrightarrow{\text{COG}}$ — Center of gravity of an event:

$$\overrightarrow{\text{COG}} = \frac{\sum_{i=0}^{n_{\text{DOMs}}} q_i \vec{x}_i}{\sum_{i=0}^{n_{\text{DOMs}}} q_i}, \tag{5.3}$$

with the total charge q_i and the position $\vec{x}_i$ of each DOM in cylindrical coordinates. COG_ρ denotes the radial and COG_z indicates the z-component.

- l_{sep}: Distance between the center of gravity of the first and last quarter of hit DOMs within a radius of 150 m around the reconstructed path.

- l_{empty}: Minimum distance between hit DOM positions projected onto the track. A small value indicates a smooth track signature.

- $\sigma_{\text{paraboloid}}$: Angular uncertainty, calculated as the quadratic mean of the error ellipse.

- $\Delta\mathrm{LLH}_{\mathrm{Bayes}}$: Measure of misreconstruction as the difference in likelihood between up-going and down-going tracks with a Bayesian prior $\phi(\Theta)$ for down-going atmospheric muons:

$$\Delta\mathrm{LLH}_{\mathrm{Bayes}} = \log\left(\mathcal{L}(\hat{H}_u)\right) - \log\left(\mathcal{L}(\tilde{H}_d)\phi(\tilde{\Theta})\right). \tag{5.4}$$

The definition of up-going and down-going tracks is further elaborated in the next section.

5.1.2 Muon Level 3

The primary objective of Level 3 reconstruction and processing is to decrease the contamination of atmospheric muons in the sample, whilst simultaneously retaining as many neutrino events as possible. The sky observed by IceCube is divided into the North ($0° \leq \Theta \leq 85°$) and South ($86° \leq \Theta \leq 180°$), based on the arrival direction in zenith of the incoming particle. Particles from the North are defined as *down-going* since they hit the detector from the top surface. Consequently, particles from the South are classified as *up-going*. Down-going events are dominated by atmospheric muons because of their large abundance in atmospheric air showers compared to atmospheric neutrinos. In contrast, up-going track signatures primarily originate from muon neutrinos due to the limited distance that muons can travel in ice. The maximum distance that muons can penetrate the Earth is approximately 13 kmwe [57] so that they are mostly unable to reach the detector.

The Muon Level 3 processing step is divided into preselection, separation into individual events, quality cuts, and directional and energy reconstruction. The preselection stage minimizes misreconstructed low energy events by retaining those with a total charge exceeding $Q_{\mathrm{tot}} \geq 100$ PE and $d_{\mathrm{Qavg}} \leq 90\,\mathrm{m}$. The second selection eliminates inaccurately reconstructed events whose reconstructed track is distant from the DOMs, which poses greater difficulties in reconstruction. Furthermore, the zenith-dependent muon filter is applied using the likelihood of angular reconstruction $\mathcal{L}$ from the MPE reconstruction:

$$\begin{aligned}
\frac{\log(\mathcal{L})}{n_{\text{DOMs}}-3} &\leq 8.9 && \text{if} \quad -1.0 \leq \cos(\Theta) &< 0.2 \\
Q_{\text{tot}} &> 3.0\cos(\Theta) + 0.65 && \text{if} \quad +0.2 \leq \cos(\Theta) &< 0.5 \\
Q_{\text{tot}} &> 0.6\cos(\Theta) + 2.3 && \text{if} \quad +0.5 \leq \cos(\Theta) &< 1.0.
\end{aligned} \tag{5.5}$$

Afterward, the *HiveSplitter* [122] divides coincident events in the detector into individual ones by analyzing the causality of light propagation through the ice. All reconstruction algorithms except LineFit (see Chapter 3.6) assume a single primary particle and cannot cope with multiple simultaneous events. However, the splitter might fail in distinguishing between vertically through-going, low energy events. The module *CoincSuite* is applied as a secondary splitting module that searches for causal connections among sub-events.

The final step of the Level 3 selection is passen when

$$\begin{aligned}
\left(\left({}^{l_{\text{dir}}}/_{180\,\text{m}}\right)^2 + \left({}^{n_{\text{dir}}}/_{10}\right)^2\right) > 2 \quad &\text{and} \quad n_{\text{dir}} > 6 \\
\text{or} \quad \frac{\mathcal{L}_{\text{reduced}}}{\text{ndof}} &< 9 \\
\text{or} \quad \hat{\mathcal{L}}_{\text{reduced}} \cdot \text{ndof} &< 7.5.
\end{aligned} \tag{5.6}$$

The parameters in the selection are obtained from the first successful reconstruction, either by SPEFit or MPEFit (see description in Chapter 3.6). Despite the rate being lowered from 34 Hz to 3 Hz, the number of atmospheric muons in the sample exceeds that of atmospheric neutrinos by over three orders of magnitude.

5.1.3 Background Removal with Boosted Decision Trees

The event sample is purified by two BDTs (see description in Chapter 4.1.3) by the Level 4 and Level 5 processing stages. AdaBoost is selected as the boosting method, implemented in the python library `scikit-learn` [109]. The Southern Hemisphere is targeted for further selection due to the difficulty in distinguishing muons and neutrinos in the North. One possibility to keep down-going events is the search for a hit signature starting in the detector, referred to as *starting events*. An atmospheric muon must originate from outside of the detector, whereas a neutrino-induced muon can be initiated outside or inside of the detector in the ice or nearby bedrock.

Before background events are removed by the BDTs, a cut on the MPEFit reconstruction quality is applied and each events must pass the following conditions:

$$\begin{gathered} n_{\text{DOMs}} > 12 \quad \text{and} \quad n_{\text{dir}} > 6 \quad \text{and} \quad l_{\text{dir}} > 200\,\text{m} \\ \text{and} \quad l_{\text{empty}} < 400\,\text{m} \quad \text{and} \quad \cos\left(\Theta^2_{\text{geo}}\right) < 0.2. \end{gathered}$$

The challenge here is to find an acceptable directional reconstruction since a misreconstructed direction could show the same event signature as an up-going neutrino-induced muon. Furthermore, events with more than 330 malfunctioning DOMs or four excluded non-DeepCore strings are removed from the sample. Both BDTs were trained on the subsequent variables: COG_z, COG_ρ, $\cos(\Theta)$, l_{sep}, l_{dir}, n_{dir}, $\sigma_{\text{paraboloid}}$, $\Delta\text{LLH}_{\text{Bayes}}$, n_{DOMs}, $\mathcal{L}/\text{ndof}$.

Level 4: Separation of muons and neutrinos

The first BDT is trained on MC simulations of CC muon neutrino events with a resolution of less than 5° from NuGen and muon background from CORSIKA (refer to Section 5.3 for a detailed description). The classifier is optimized in a 10-fold CV method (see Chapter 4.3). The final optimization is assessed by the comparison of signal efficiency and background contamination in dependence of the BDT score. Fig. 5.1(a) presents the event rate for the individual event populations based on the selected score cut. The number of atmospheric muons decreases logarithmically with increasing score values. The rate of atmospheric and astrophysical neutrinos remains generally stable with scores ranging from 0.2 to 0.6 but increases incrementally beyond this range. Implementing a score cut of 0.9 efficiently reduces the amount of atmospheric neutrinos while enhancing the signal. A small number of cascade events from electron neutrinos remains in the sample, which are to be removed in the next step.

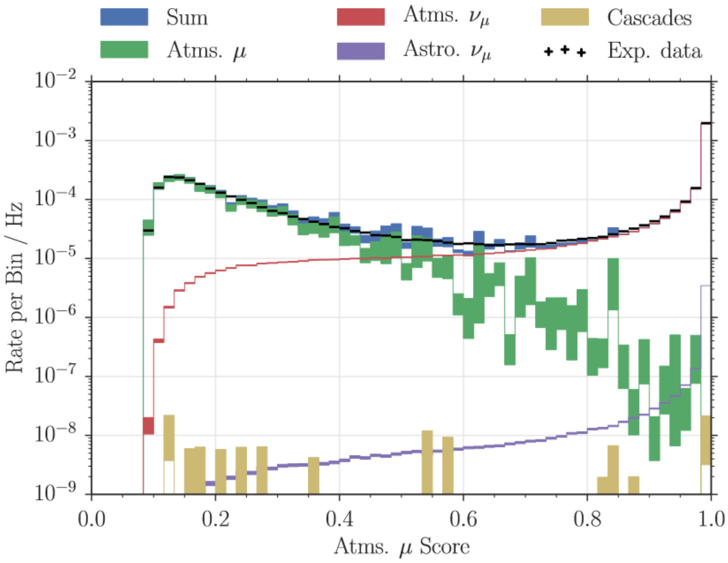

(a)

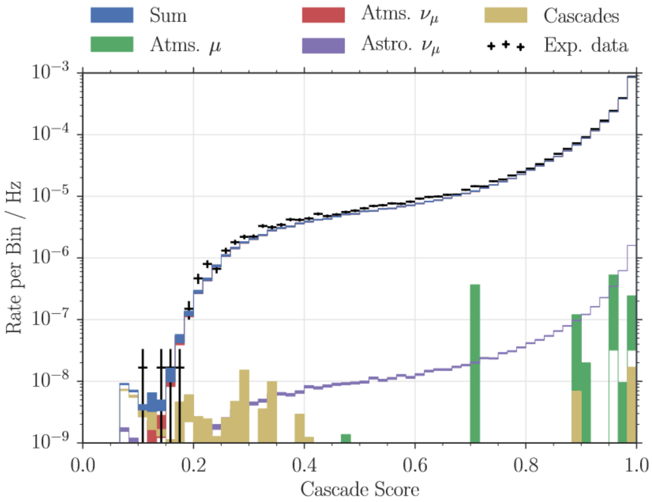

(b)

Figure 5.1: Event rate of individual particle populations in dependence of BDT score for the separation of muon neutrino-induced tracks from (a) atmospheric muons and (b) cascade signatures. Figure taken from Ref. [119].

Level 5: Separation of tracks and cascades

The cascades in the sample can usually be identified by a degraded performance of the track reconstruction algorithms. The second BDT diminishes the impact of cascades in the sample. The signal definition remains the same as for the first BDT. Cascade events from electron neutrinos are classified as background. No further BDT parameter optimizations are carried out since the signal category is unaltered. The event rate for the individual populations is depicted in Fig. 5.1(b). The event rate gain exhibits similar patterns as shown in Fig. 5.1(a), as anticipated due to the unchanged signal definition. A cascade score cut above 0.5 can exclude most cascades, leaving only a negligible amount in the sample. Nevertheless, the sample will inevitably have a small contribution from atmospheric muons, as noted in the introduction to this section.

5.2 Selection of Arrival Directions

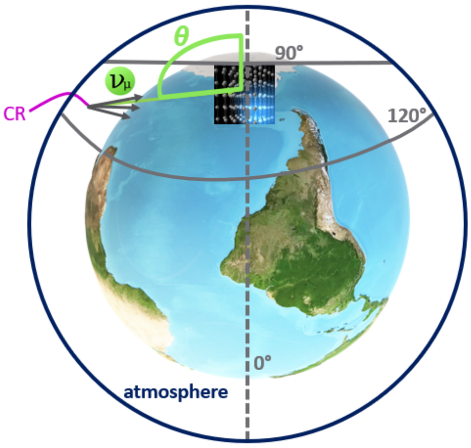

Figure 5.2: Illustration of the selected zenith region and an incoming atmospheric neutrino from a CR-induced shower. The zenith angle is defined with respect to the rotation axis at 0°. The atmosphere is scaled for better visibility.

The event selection presented in the previous section includes up-going events in the entire zenith range between 86° to 180°. In order to study the seasonal variation of the atmospheric neutrino flux, the selected sample of events requires temperature variations throughout the year at the altitude where neutrinos are produced. The temperature remains relatively constant in the zenith directions between the Tropic of Cancer and the Tropic of Capricorn, and thus, due to the lack of seasonal variations, it should be excluded from this analysis. The progenitor analysis from Ref. [72] examined the correlation between temperature variations in the stratosphere and the measured neutrino rate, selecting the zenith region because of its present temperature changes throughout the year. This selection is based on the quantity T_{eff}, which represents the stratospheric effective temperature. The temperature is calculated by the integration of the atmospheric temperature profiles at various depths, convoluted with the corresponding energy-dependent neutrino production yields. The temperature profiles were taken from the Atmospheric Infrared Sounder (AIRS) [123], using one year of data from May 2012 to April 2013. A detailed description of the device is given in Appendix D.1.3. Fig. 5.3 presents the computed effective temperature corresponding to the zenith angle.

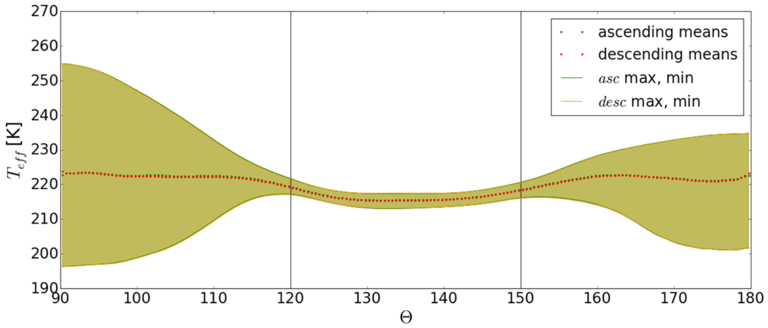

Figure 5.3: Calculated effective temperature from one year of AIRS data versus zenith angle. Figure taken from Ref. [72].

The zenith angle is defined such that $\Theta = 90°$ corresponds to the IceCube detector, and $\Theta = 135°$ to the Equator. The effective temperature variation peaks at $\Theta = 90°$ and gradually decreases, remaining relatively constant between zenith angles from 120° to 150°. The lack of variation in this range can be attributed to the tropical atmosphere, where the temperature remains constant throughout the year. The Northern Hemisphere beyond $\Theta > 150°$ shows increasing temperature variations with the zenith angle. However, the temperature amplitude remains lower in comparison to the Southern Hemisphere. Since the number of neutrinos declines with increasing zenith angle, only events between zenith angles from 90° to 120° are selected for this analysis, as illustrated in Fig. 5.2. The same zenith range was investigated in Ref. [72]. The sample is cut on the reconstructed zenith angle from SplineMPE (see description in Chapter 3.6). The selection of the zenith region holds up to Chapter 8, where the zenith region is restricted from 90° to 110° based on detailed evaluation of temperature and rate variation.

5.3 Simulation

The NuGen simulation set 21002 is used to train and optimize the unfolding algorithm, as described in Chapter 6.2. The sample comprises muon neutrino and antineutrino events in the energy range of 1×10^2 GeV to 1×10^8 GeV, processed to the event selection presented in Section 5.1.

5.3.1 Weighting

Simulations in astroparticle physics often involve sampling from a simple power law distribution of either E^{-1} or E^{-2} to efficiently simulate high-energy events. Initiating simulations with a realistic flux model would be computationally costly, particularly for high-energy events featuring steep power laws. Simulated events are weighted to a realistic flux model for the respective analysis.

As the simulation is created from an energy distribution of E^{-2}, the simulated events are weighted using a realistic representation of the expected neutrino flux. This procedure is crucial to train the unfolding algorithm and to make comparisons between data and simulation for each variable utilized in the unfolding process. The atmospheric flux from ν_μ and $\bar{\nu_\mu}$, both the conventional and prompt component, is modeled by MCEq. Throughout the entire thesis, Sibyll 2.3c is set as the hadronic interaction model, H3a as the primary CR composition model, and NRLMSISE-00 as the empirical model for the atmosphere. A detailed description of the models is given in Chapter 2.3.4 and 2.2.2, and in Appendix D.
In addition, the impact of the astrophysical flux needs to be considered as well, which can be approximated by

$$\Phi_{\nu_\mu+\bar{\nu_\mu}} \approx 1.44 \times 10^{-18} \cdot \left(\frac{E}{100\,\mathrm{TeV}}\right)^{-2.37} . \tag{5.7}$$

This estimation provides a realistic scenario of the flux at energies beyond 10 TeV [118]. The astrophysical component might only be relevant for the added overflow bin in the optimization (see Chapter 6.4). Since the event selection does not differentiate between neutrinos of atmospheric or astrophysical origin, the astrophysical component is added for the complete modulation of the neutrino flux.

Each simulated event is weighted by the simulation quantity *OneWeight* [91], which accounts for the complete flux modulation. OneWeight is a measure of a time-independent inverse flux, expressed in units of $\mathrm{GeV\,cm^2\,sr}$ per unit area and energy:

$$\text{OneWeight}_i = p_{\text{int}} \cdot A_{\text{gen}} \cdot \frac{\int_\Omega \int_{E_1}^{E_2} \Phi_{\text{gen}}(E_i) \mathrm{d}E \mathrm{d}\Omega}{\Phi_{\text{gen}}(E_i)}. \tag{5.8}$$

The probability of forced interaction near the detector p_{int} can be expressed as $\frac{\mathrm{d}^2 N}{\mathrm{d}E \mathrm{d}\Omega}$, where N represents the number of detected neutrinos. In this scenario, A_{gen} is the generation surface, while Φ_{gen} defines the injected flux of neutrinos [124]. The event weight w_i is computed based on OneWeight, the number of generated events N_{gen}, and the flux Φ_i to which the event is weighted:

$$w_i = \frac{\text{OneWeight}_i}{N_{\text{gen}}} \cdot \Phi_i. \tag{5.9}$$

The total weight of the event is given by the sum of the atmospheric and astrophysical weight. The weighting accounts for the number of neutrinos and antineutrinos in the simulation, whereas neutrino telescopes cannot distinguish between particle and antiparticle. It is corrected for by adding the contribution from neutrinos and antineutrinos for each respective flux representation.

The unfolding algorithm described in Chapter 6.2 cannot incorporate weights as an additional input to the training set or sample to be unfolded. Hence, simulated events are resampled based on their flux weights to create a realistic training sample with the module `multinomial_resampling` from the Python library `filterpy.monte_carlo` [125]. Three sampling methods from the same package were compared in the progenitor work in Ref. [126], in which the multinomial re-sampling method produced the best results. The sampling methods were compared again on the simulation set at hand.

5.3.2 Effective Area

To obtain a universally independent differential flux $\mathrm{d}\Phi/\mathrm{d}E$ from an event spectrum N_i, correcting the event spectrum is necessary. This can be achieved by incorporating the livetime T of the dataset, the effective detection area A_{eff}, the width of the energy bin ΔE and the solid angle $\Delta\Omega = 2\pi \cdot \cos(\Theta_{\text{min}}) - \cos(\Theta_{\text{max}})$:

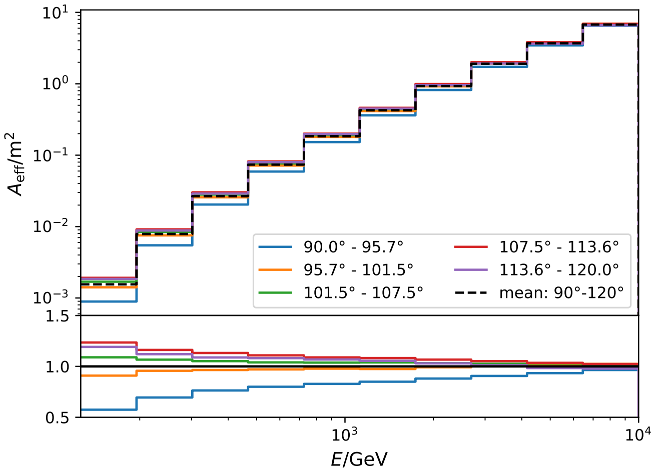

Figure 5.4: Effective area per equidistant bins in cos(Θ) for zenith angles between 90° to 120°.

$$\frac{\mathrm{d}\Phi_i}{\mathrm{d}E\mathrm{d}\Omega} = \frac{N_i}{T \cdot A_{\mathrm{eff}} \cdot \Delta E \Delta\Omega}. \tag{5.10}$$

The effective area refers to the hypothetical area of a fully efficient detector [52]. It describes the efficiency of the event selection and is analysis-specific. The effective area per energy bin and solid angle is calculated by dividing the number of events that survive the event selection by the total number of generated events [124]:

$$A_{\mathrm{eff}}(\Delta E, \Delta\Omega) = A_{\mathrm{gen}} \cdot \frac{\hat{N}_{\mathrm{events}}(\Delta E, \Delta\Omega)}{\hat{N}_{\mathrm{gen}}(\Delta E, \Delta\Omega)}. \tag{5.11}$$

A_{gen} represents the generated detection area in the simulation, while $\hat{N}_{\mathrm{events}}$ denotes the expected number of events after the selection process. Equ. 5.11 is an approximation for the discrete representation of the effective area. The number of events that successfully pass through the event selection can be determined by

$$\hat{N}_{\mathrm{events}}(\Delta E, \Delta\Omega) = \sum_{i=1}^{N_{\mathrm{gen}}} w_i \cdot p_{i,\mathrm{int}} = \sum_{(i|E_i \in \Delta E, \Omega_i \in \Delta\Omega)} p_{\mathrm{int},i}, \tag{5.12}$$

with the probability of forced interaction in the vicinity of the detector $p_{\mathrm{int},i}$. The effective area can be expressed in a OneWeight-formalism:

$$A_{\text{eff}}(\Delta E, \Delta\Omega) \approx \frac{1}{N_{\text{gen}}\Delta\Omega\Delta E} \cdot \sum_{(i|E_i \in \Delta E, \Omega_i \in \Delta\Omega)} \text{OneWeight}_i. \tag{5.13}$$

A detailed derivation can be found in Ref. [126].

The effective area for the analysis at hand is calculated in four equidistant zenith bins in $\cos(\Theta)$, as displayed in Fig. 5.4. The selected energy binning is discussed in Chapter 6.4. The effective area decreases slightly at energies below 1 TeV in the zenith band close to the horizon, as these events are more difficult to detect in IceCube.

5.4 Data

The dataset is processed to the event selection explained in Section 5.1. Only years with a complete detector configuration are selected to ensure consistency in the reconstructed variables. Despite the completion of detector construction in December 2010, the strings deployed during this construction season were integrated into the data acquisition chain only on May 7, 2011, with the start of the new run configuration. Data in IceCube is stored in detector runs of approximately eight hours each. Runs marked as *good* are added to the *Goodrunlist*, from which datasets are constructed. A run is deemed *good* when a sufficient number of DOMs and strings are declared as active, depending on the specific event selection (refer to Section 5.1). Currently, data is available through December 2022, resulting in the detection of 523 736 neutrino events within an effective detector livetime of 11.3 years.
Regarding the data processing stream, the charge distribution of individual photoelectrons was shifted by 4% in a recalibration campaign in 2016. As a result, data predating 2016 has undergone reprocessing to align with the updated DOM calibration, which is referred to as Pass2-processing [128]. Only the calibration has been changed, which was reimplemented in all previous simulation samples and data processing.

The zenith distribution of the dataset is depicted in Fig. 5.5. Most of the events originate from close to the horizon, while the number of events decreases as the zenith angle increases. Furthermore, Fig. 5.6 shows the average monthly neutrino rate from May 2011 to December 2022, with statistical uncertainties included. The observed rate variations throughout the year are not entirely symmetrical. The maximum

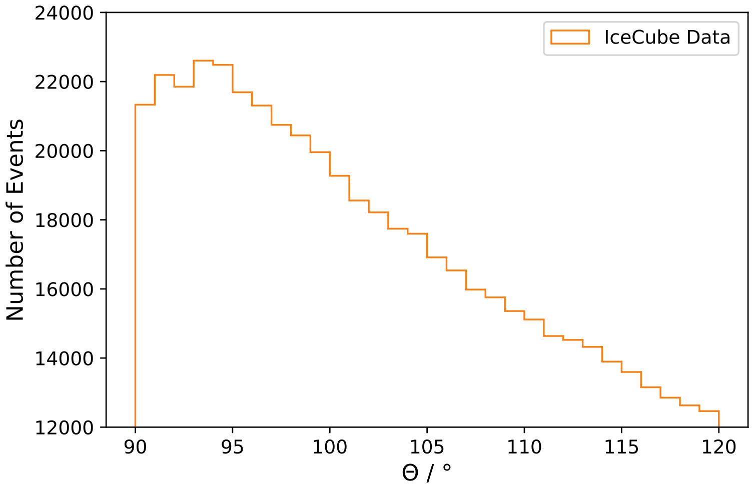

Figure 5.5: Zenith distribution of the complete dataset [127].

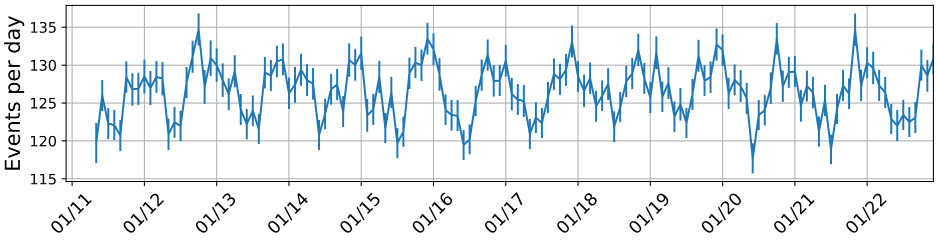

Figure 5.6: Average monthly neutrino rates in the zenith range from 90° to 120° from May 2011 to December 2022. Uncertainties denote the standard deviation of the rate.

rate differs from year to year and is often reached in October or shows a broader maximum from October to January. The minimum rate occurs more sharply in June or July.

5.5 Data-MC Agreement

The algorithm used for unfolding is optimized and trained on simulated events, which requires close agreement between simulation and data for the unfolding of the energy spectrum. Fig. 5.7 shows the event distribution of each of the variables employed in the unfolding process (see Chapter 6.3 and 6.5). The ratio of simulated to data events is nearly constant, with a surplus of roughly 20% in the data, illustrated

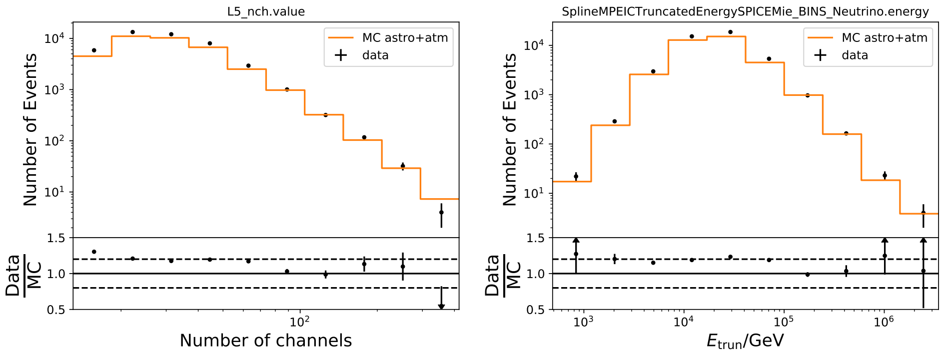

(a)

(b)

Figure 5.7: Comparison of data and MC simulated events in both unfolding variables. The error bars depict the statistical uncertainty in data. Dashed lines indicate a ratio of ±20%.

by the dashed lines. This can be attributed to uncertainties in atmospheric fluxes. Simulation of muons and neutrinos commonly predict fewer events than being observed, i.e. discussed in Ref. [129, 130]. The diffuse neutrino flux measurements fit the atmospheric normalization to approximately 19%, such as in Ref. [131]. Only two bins in both variables show no excess of data. A constant offset in the agreement between data and MC is acceptable because the sampling procedure normalizes the weights. The crucial part is the agreement in shape between the simulation and data variables.

6 Solving Inverse Problems: Determination of the Energy Spectrum

Inverse problems are a frequent obstacle in experimental physics. When a physical quantity cannot be accessed directly through experiments, such as neutrino energy, it must be derived from correlated quantities that can be measured instead. To obtain the neutrino energy spectrum, this chapter introduces the unfolding concept, in particular the Dortmund Spectrum Estimation Algorithm (DSEA+). The subsequent section explains the estimator variables and algorithm optimization.

6.1 Unfolding in a Nutshell

6.1.1 Definition

An inverse problem is the determination of the distribution of a physical quantity x, from a set of measurements. However, this process is constrained by measurement uncertainties and inaccuracies, including limited acceptance and limited measurement accuracy, in addition to the difficulty of determining the related quantity. As a consequence, the related quantity y is measured instead of x, and the probability density $g(y)$ is obtained. The relationship between the true distribution $f(x)$ and the observed distribution $g(y)$ is made by a convolution integral, referred to as the Fredholm integral equation of the first kind [132]:

$$g(y) = \int_a^b A(x,y) f(x) \mathrm{d}x + b(y) + \epsilon(y). \tag{6.1}$$

Because the relationship between the variables may not be fully known, the equation is not necessarily deterministic. The conversion of one quantity to another has a finite resolution due to the experimental setup. Background contamination $b(y)$ and deviations attributed to statistical errors $\epsilon(y)$ and other imperfections present in the measurement process restrict the ability to solve Equ. 6.1. Since the number of observations is finite, the inverse problem is discretized into histograms:

$$\vec{g}(y) = \mathbf{A}(x, y)\vec{f}(x) + \vec{b}(y) + \vec{\epsilon}(y). \tag{6.2}$$

MC simulations are often utilized to approximate $\mathbf{A}(x, y)$, while statistical uncertainties and noisy background pose additional challenges. The process of determining the folding matrix $\mathbf{A}$ to reconstruct $\vec{f}(x)$ is known as *unfolding*. The division of the target quantity into a binned distribution introduces uncertainties and biases, which are further enhanced by the limited measurement accuracy [133]. The conversion into the true target distribution is statistically an ill-conditioned problem. Oscillating solutions in bins with insufficient statistics are characteristic for inverse problems. Various regularization techniques can suppress these oscillations to establish limitations for achieving a smoother solution, displayed in Ref. [134]. A common method is a smooth second derivative, as in Ref. [135].

6.1.2 Application to Neutrinoastronomy

In neutrino astronomy, the reconstruction of the true neutrino energy distribution $f(x)$ is a challenging task as it is dominated by a distribution of background events from atmospheric muons. Chapter 5.1.3 discusses event selection techniques that limit the background to sub-percent levels, so that the inverse problem becomes approximately background-free and the term $b(y)$ can be eliminated from Equ. 6.2. However, the neutrino energy needs to be inferred from the muon induced in the interaction of the neutrino in the ice or nearby bedrock [5]. The rate of observed neutrino-induced muons is determined by the integration over the convolution of the neutrino spectrum ${}^{\mathrm{d}N_\nu}/_{\mathrm{d}E_\nu}$ and the probability that the neutrino induces a muon in the energy range detectable for IceCube [136]:

$$\frac{\mathrm{d}N_\mu}{\mathrm{d}E_\mu} = \int_{E_\mu}^{\infty} \mathrm{d}E_\mu \left(\frac{\mathrm{d}N_\nu}{\mathrm{d}E_\nu}\right) \left(\frac{\mathrm{d}P(E_\nu)}{\mathrm{d}E_\mu}\right). \tag{6.3}$$

The energy resolution of the muon is smeared due to energy loss ${}^{\mathrm{d}E}/_{\mathrm{d}x}$ during the propagation through a medium, which is defined as

$$\frac{\mathrm{d}E}{\mathrm{d}x} = -a(E) - b(E)E. \tag{6.4}$$

Two distinct processes characterize the energy loss in this scenario. The first process involves continuous energy losses through ionization, represented by the term $a(E) \approx 0.24\,\mathrm{GeV\,m^{-1}}$. The second process, described by the term $b(E) \approx 3.3 \times 10^{-4}\,\mathrm{m^{-1}}$, represents stochastic radiative energy losses via bremsstrahlung, pair production, or photon scattering [137]. Continuous losses are dominant at low energies, but stochastic losses become dominant above $E_\mu > 1\,\mathrm{TeV}$. Stochastic losses increase linearly with energy, resulting in even larger energy reconstruction uncertainties. In-ice energy deposits from secondary particles can initiate electromagnetic cascades, which expose an even larger number of secondary particles to energy loss processes. Consequently, the energy reconstruction becomes more difficult.

6.2 DSEA+

Common unfolding methods, such as iterative Bayesian unfolding [138], which is based on the conditional probability in Bayes' theorem, or regularized unfolding with a maximum likelihood approach [134, 139], return a discrete probability distribution, but lose information about each event. A novel approach to unfolding a spectrum is the Dortmund Spectrum Estimation Algorithm (DSEA+) [6, 140, 141]. It presents unfolding as a multinomial classification task, similar to supervised machine learning. The algorithm categorizes each event into predefined energy bins, which are treated as separate and independent categories. One of the advantages compared to other unfolding techniques is the retention of data for each event after unfolding.

6.2.1 Workflow

DSEA+ iteratively rescales a predicted PDF based on a regularization function to estimate the energy bin (class category) through a classifier from preselected energy proxies. The input classifier can be any machine learning classifier, e.g. from the `scikit-learn` [109] Python library, as long as it estimates conditional probabilities (confidences) for each input event x_n to have a corresponding neutrino energy to energy bin i. These discrete PDFs are denoted as $c_M(i \mid x_\mathrm{n})$. The confidences for each event are accumulated and normalized, and DSEA+ returns a discrete PDF [142], which represents the total probability of a particle having a specific energy, in each iteration k:

$$\hat{f}_i^{(k)} = \frac{1}{N} \sum_{n=1}^{N_{\text{events}}} c_M(i \mid x_{\text{n}}) \qquad \forall\, 1 \leq i \leq I. \tag{6.5}$$

The current estimate is regularized by scaling it to specific functions, as described in the following section. The scaled estimate acts as a prior guess to which the output of the classifier is weighted in the subsequent iteration of the algorithm. This method is repeated until adequate precision is attained. A uniform prior is assumed as the initial guess for the first iteration. The process is illustrated in Fig. 6.1.

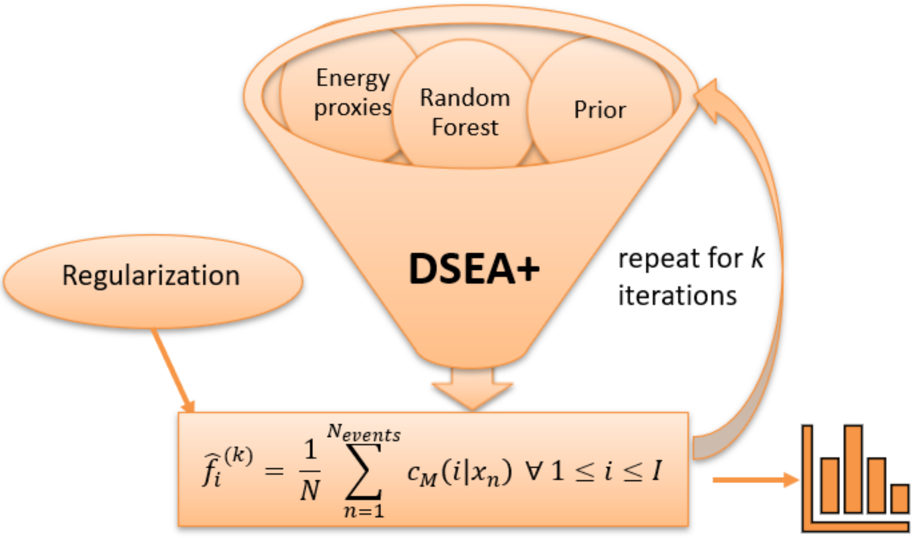

Figure 6.1: Iterative workflow of DSEA+. The current estimate $\hat{f}_i^{(k)}$ is scaleable by various regularization functions.

6.2.2 Regularization

The estimated PDF can be adjusted by three-step size decay functions, which smooth the spectrum and control the convergence speed of the algorithm. Each iteration updates the current estimate $\hat{f}^{(k-1)}$ towards the next iteration k by

$$\hat{f}^{(k),+} = \hat{f}^{(k-1)} + \alpha^{(k)} \cdot p^{(k)}, \tag{6.6}$$

with the step size $\alpha^{(k)} \geq 0$ and the search direction $p^{(k)} = \hat{f}^{(k)} - \hat{f}^{(k-1)}$ [142]. The step size can remain constant in each iteration, as it is for multiplicative (slow) and exponential (fast) decay, or it can be modified iteratively based on the previous estimation. The step sizes are defined as

$$\begin{aligned} \alpha_{\text{multiplicative}} &= k^{\xi-1}, \qquad (6.7)\\ \alpha_{\text{exponential}} &= s\cdot\xi^{k-1}, \qquad (6.8)\\ \alpha_{\text{adaptive}} &= \arg\min_{\alpha^{(k)}\geq 0} \hat{l}_r^{(k)}(\hat{f}^{(k-1)}+\alpha^{(k)}). \qquad (6.9) \end{aligned}$$

$\xi > 0$ denotes the decay rate, and s the initial scaling of the step size. Step size decay can speed up the convergence to the optimal estimate of DSEA+ compared to the unregularized algorithm by requiring fewer iterations. However, selecting the ideal step size is challenging, given that a smaller step size may hinder the convergence of the algorithm. Adaptive step sizes (Equ. 6.9) circumvent this caveat by adjusting the step size in each iteration. While other methods may not be able to find the optimal solution if the step size is too large, the adaptive approach allows the step size to shrink when the optimal solution is close. α_{adaptive} is adjusted based on the current estimate through maximum likelihood optimization in the search direction. This process is similar to a line search [143] in the context of numerical optimization. The loss function $l_r^{\hat{(k)}}(\hat{f})$ to be minimized in the adaptive step size decay is defined by the Regularized UNfolding (RUN) algorithm [134, 139]:

$$\hat{l}_r^{(k)}(\hat{f}) = \hat{l}^{(k)}(f) + r(f), \tag{6.10}$$

with the objective function

$$\hat{l}^{(k)}(\mathbf{f}) = \frac{1}{2} f^{\mathrm{T}}\mathbf{H}\mathbf{f} - \mathbf{f}^{\mathrm{T}}(\mathbf{H}\hat{f}^{(k)} - \boldsymbol{\nabla} l(\hat{f}^{(k)})), \tag{6.11}$$

and the Tikhonov regularization [135] term

$$r(f) = \frac{\tau}{2}\cdot\sum_{i=2}^{\ell-1}(-\mathbf{f}_{i-1}+2\cdot\mathbf{f}_i-\mathbf{f}_{i+1})^2 = \frac{\tau}{2}\cdot\mathbf{f}^T\mathbf{C}\mathbf{f}. \tag{6.12}$$

H denotes the Hessian of the current estimate. To obtain a smoother solution, the estimate is constrained by the Tikhonov regularization [135] instead of solely optimizing the objective function. The maximum likelihood optimization is realized by dimension reduction of the observable space to ℓ degrees of freedom. The dimensional reduction is realized by the CART algorithm (introduced in Chapter 4.1). Within this algorithm, clusters represent the degrees of freedom in classification, equivalent to the number of leaves in the tree. The impurity of each node is measured by the Gini-index (see Equ. 4.1), indicating the the probability of an incorrect classification of a random event.The step size can be regularized by the regularization strength $\tau \geq 0$ (Equ. 6.12). The Tikhonov term is regulated solely by the flattening of the second derivative of the loss function when $\tau = 0$ (Equ. 6.11). If $\alpha = 1$, no regularization is applied.

6.3 Description of Energy Proxies

The selection of suitable energy proxies for unfolding is based on progenitor work in Ref. [144, 145, 146, 126]. Several reconstruction algorithms use charge measurements to reconstruct a neutrino track through the detector and to determine the arrival direction and energy, as discussed in Chapter 3.6. The progenitor study in Ref. [126] on old simulations (discussed in Chapter 5.3) tested a combination of five variables, three of which were ultimately chosen as the optimal combination. It is crucial to limit the number of unfolding variables since correlated variables have a negative impact on convergence speed. The parameter optimization in Section 6.4 is performed on the same variables, and their combinations are tested in Section 6.5:

- **Number of Channels** (`L5_nch`): Number of DOMs exceeding the charge threshold of 0.25 PE [100]. The prefix `L5` denotes the highest level of processing, where potential background hits are removed and the overall quantity is calculated.

- **Direct Hits** (`L5_ndir_c`): The number of direct photons represents the number of photons detected in a given time residual without scattering by ice impurities [100], as defined in Chapter 5.1.1. The number relies on the reconstructed track and counts the photons along the respective track hypothesis. The variable is computed by utilizing the SplineMPE reconstruction (refer to Chapter 3.6) and the measured hits within the time window `C` from $-15\,\mathrm{ns} < t < 75\,\mathrm{ns}$.

- **Truncated Energy** (`Etrun`): Truncated neutrino energy is a standard energy reconstruction in IceCube [147] that can be applied to a reconstructed track, such as e. g. SplineMPE. The algorithm calculates the differential energy loss using the ratio of observed to expected photoelectrons as if induced by muons with a fixed energy loss of 1 GeV m^{-1}. The energy loss can be determined in two ways – by calculating the losses at each hit DOM (referred to as the suffix `DOMs`) or along the track by projecting the hit DOMs onto the reconstructed track (referred to as the suffix `BINs`). The algorithm estimates the energy by truncating the largest energy losses. Both approaches produce comparable outcomes [126], and the first method is selected for this work.

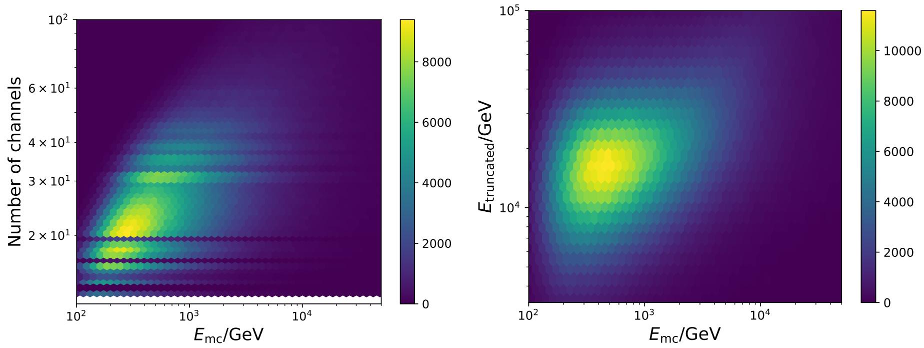

(a) (b)

Figure 6.2: Correlation between the final selection of energy proxies and simulated neutrino energy E_{mc}.

6.4 Parameter Optimization for DSEA+

The energy spectrum is unfolded into ten bins equidistant in logarithmic space from 125 GeV to 10 TeV from the energy proxies introduced in the previous section: `L5_nch`, `L5_ndir_c`, and `Etrun`. The exact bin edges are depicted in Table B.2 and C.2 in the Appendix. The maximum energy is set to 10 TeV because of the limited statistics at higher energies. An important factor for the low-energy limit to consider is that events below 100 GeV are not simulated, as it is the threshold energy for neutrino detection in IceCube. This aspect is covered by adding under- and overflow bins as two additional bins below and above the defined range. These bins are essential when an event in the dataset has an unfolded energy that exceeds the predefined energy range, such specific values of the proxy variables are outside of the simulation range. Another aspect is the correct determination of bin-to-bin migrations. The combination of the three energy proxies was determined to be optimal in progenitor studies using MC simulations with different DOM calibrations Ref. [126]. For a detailed account of changes, see Ref. [128] and Chapter 5.4. The selected parameters will be further examined in Section 6.5 after the optimization of DSEA+ and its parameters. An initial selection of proxy variables is required for the optimization process. The choice of parameters is strongly dependent on the variables at hand. Parts of the optimization process have been discussed in Ref. [148].

The search for optimal parameters of DSEA+, is performed through a 10-fold CV on 500 000 simulated events, as discussed in Appendix 4.3. The choice of this number balances accurate unfolding with acceptable optimization runtime. The quality of the resulting spectrum is evaluated using the Wasserstein Distance (WD) [116] (defined in Chapter 4.4).

6.4.1 General Aspects

The selection of the most appropriate machine learning classifier is investigated by testing six classifiers from `scikit-learn`:Naive Bayes (NB) [114], Adaptive Boosting (AdaBoost), Gradient Boosting (GB) [149], Decision Tree (DT) [107], Extremely Randomized Trees (ERT) [110], and Random Forest (RF) [104]. For comparison, the classifiers are used with their default settings. After optimizing the classifier that yields the smallest WD over the entire energy range including under- and overflow bin, the internal parameters of the classifier are further optimized. The regularization parameters, in particular the parameters of the step size decay functions, are optimized in the last step. Since a grid search over all parameters in parallel is computationally expensive, three values for each parameter are tested and the vicinity of the best-performing one is investigated in more detail. This process, developed in Ref. [126], is utilized in this thesis for new IceCube simulations after a recalibration of the modules [128]. The number of iterations in DSEA+ is standardized to four to ensure that all predictions converge (see Appendix B.3). To provide a realistic scenario, the E^{-2}-distributed MC is resampled using neutrino flux weights, which include conventional, prompt, and astrophysical weights (described in Chapter 5.3). The description of the classifiers can be found in Chapter 4.

6.4.2 Selection and Optimization of the Classifier

Fig. 6.3 shows the results of the grid search for optimal classifier settings. Additionally, Fig. 6.3(a) and Fig. 6.3(b) exhibit the unfolded spectra with various classifiers using default settings. An in-depth analysis reveals that Adaptive Boosting performs the worst, as it unfolds a flat spectrum. It is the effect of the initial uniform prior that dominates the output spectrum. The Gaussian Naive Bayes and Gradient Boosting classifiers exhibit comparable performances with WD ≈ 0.01000 at first glance. Nonetheless, the unfolded spectra vary substantially in shape. The unfolded spectrum obtained with the Gradient Boosting Classifier deviates less than 10% from the true spectrum in bins 2 to 8. However, it differs significantly in the underflow bin, leading to an increase in the overall WD. The unfolded spectrum with the Gaussian NB is steeper and leads to large discrepancies in the energy range of interest.

The tree-based classifiers presented in Fig. 6.3(b) perform similarly, and the unfolded spectrum only deviates at a percentage level from the MC truth. The most accurate prediction is obtained with the RF with WD ≈ 0.00122. Under- and overflow bins are also estimated precisely at percentage level.

Fig. 6.3(c) to Fig. 6.3(f) display the subsequent grid search for selected parameters of the RF classifier. The RF has an unlimited default tree depth, as shown in Table 4.1. Increasing the tree depth enhances the classifier's complexity and classification time. However, a tree depth of 10 is insufficient as the unfolded spectrum is too flat with WD ≈ 0.00994. Above a maximum depth of 20, the unfolded spectrum remains unchanged with WD ≈ 0.00100, comparable to the unfolded spectrum with default RF settings. The default number of estimators, the number of trees in the forest, is 100. For the grid search, a lower number of trees is used to reduce the runtime of the classification (Fig. 6.3(d)). The obtained WDs are slightly lower than for the default RF, but comparable with WD ≈ 0.00160 for 50 estimators. The maximum number of features determines the number of observables for the best split at a tree node and establishes the importance of each variable for accurate classification. A maximum number of features of 1 or 2 yields results comparable to the standard classification with WD ≈ 0.01200 (Fig. 6.3(e)). However, there is a discrepancy of approximately 2% in the underflow and the last two bins when considering a maximum of three features in the unfolded spectrum. The increase of the WD with increasing number of features indicates that potentially redundant fea-

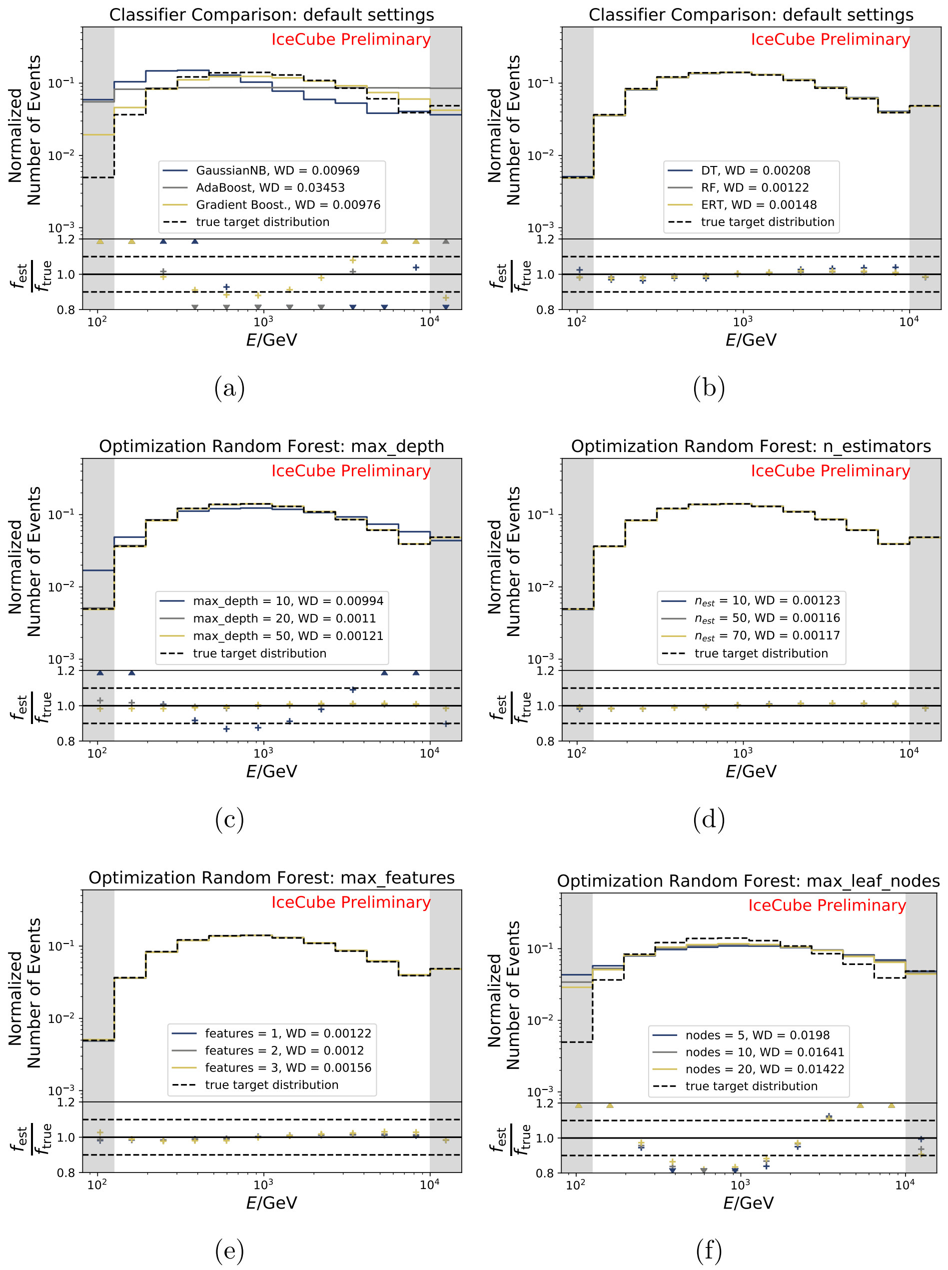

(a) (b) (c) (d) (e) (f)

Figure 6.3: *Top panel*: Unfolded normalized event spectra compared to the true distribution in black for different classifier settings. Under- and overflow bins are denoted by shaded bins. *Lower panel*: Ratio of unfolded spectra to the true distribution. (a) and (b) depict the spectrum obtained with classifiers at default settings, (c) to (f) the optimization of the RF.

tures are selected for the classification. Thus, the selection of variables is further investigated in Section 6.5. The maximum number of leaf nodes at every decision vertex is determined by the maximum number of leaf nodes parameter and is, by default, unrestricted (see Table 4.1). The adjustment of this parameter alone, without changing any others, does not enhance the accuracy of the unfolded spectrum. The spectrum becomes flatter and exhibits significant deviations exceeding 20% in most energy bins.

In conclusion, the grid search for the parameters of the RF classifier does not improve the accuracy of the unfolded spectrum. Therefore, the default RF classifier settings, as shown in Table 4.1, are utilized throughout this thesis.

6.4.3 Optimization of Regularization Parameters

The search for optimal regularization parameters in DSEA+ using the default RF classifier is shown in Fig. 6.4. Figures 6.4(a) and 6.4(b) show that variation of the parameter ξ in the multiplicative step size decay (Equ. 6.7) yields on average comparable accuracy with WD ≈ 0.00190 for $\xi = 0.25$ compared to no regularization. However, $\xi > 1.5$ regularizes too strongly, and the true spectrum cannot be determined. Compared to multiplicative stepsize decay, the exponential stepsize decay (Equ. 6.8) shows a significant dependence on ξ to obtain an accurately unfolded spectrum (Fig. 6.4(c) and 6.4(d)) for a start size $s = 2$. $\xi = 0.5$ results in a spectrum similar to the default one without regularization, with WD ≈ 0.00120. The starting size for the exponential step size decay is investigated for $\xi = 0.5$. The unfolded spectrum is similar across $s = 0.5$, $s = 1$, and $s = 2$. The resulting WDs do not differ significantly from that of unregularized DSEA+.

The regularization strength is adjusted by varying the parameters for adaptive step size decay (Equ. 6.9) while keeping the others constant. To bin the observable space, the number of leaves is set to $l = 10$. The results are consistent for $\tau \leq 20$, with WD ≈ 0.00293 (Fig. 6.4(e)). The effect of the number of clusters is examined by setting the regularization strength to $\tau = 0$ so that the second term in Equ. 6.12 vanishes. A decrease in the number of leaves to $l \leq 10$ results in worse results compared to the other regularization functions (Fig. 6.4(f)). To achieve an accurate spectrum, a larger number of clusters would be needed, which would increase the runtime of the algorithm tremendously.

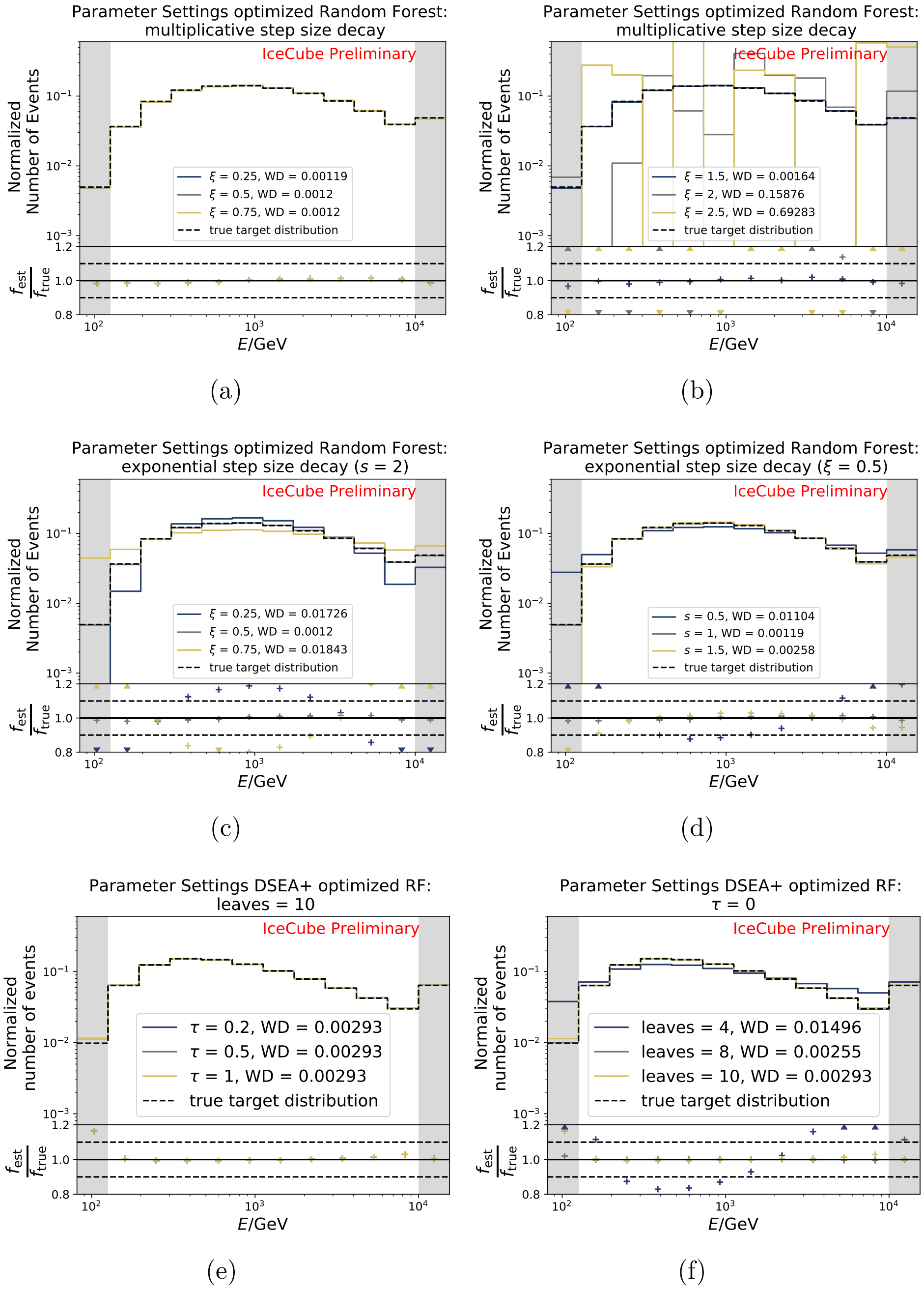

Figure 6.4: *Top panel*: Unfolded normalized event spectra compared to the true distribution in black for different regularization parameters. Under- and overflow bins are denoted by shaded bins. *Lower panel*: Ratio of unfolded spectra to the true distribution.

6.4.4 Conclusion

The grid search results for the parameters are summarized in Table 6.1. The default RF remains as the optimal classifier. Accuracy is improved only minimally through regularization, despite multiplicative and exponential step size decay. For this thesis, the parameters are selected as follows: exponential step size decay with $\xi = 0.5$ and $s = 1$.

Parameter	Value	Wasserstein Distance
Random Forest	default	0.00122
Decision Tree	default	0.00208
Extremely Randomized Trees	default	0.00148
Adaptive Boosting	default	0.03453
Gradient Boosting	default	0.00976
Gaussian Naive Bayes	default	0.00969
Random Forest: `maximum_depth`	10	0.00994
Random Forest: `maximum_depth`	20	0.00110
Random Forest: `maximum_depth`	50	0.00121
Random Forest: `maximum_features`	1	0.00122
Random Forest: `maximum_features`	2	0.00120
Random Forest: `maximum_features`	3	0.00156
Random Forest: `n_estimators`	10	0.00123
Random Forest: `n_estimators`	50	0.00116
Random Forest: `n_estimators`	120	0.00117
Random Forest: `max_leaf_nodes`	5	0.01980
Random Forest: `max_leaf_nodes`	10	0.01641
Random Forest: `max_leaf_nodes`	20	0.01422
multiplicative decay	$\xi = 0.25$	0.00119
multiplicative decay	$\xi = 0.5$	0.00120
multiplicative decay	$\xi = 0.75$	0.00120
exp step size decay	$\xi = 0.5,\ s = 0.5$	0.01104
exp step size decay	$\boldsymbol{\xi = 0.5,\ s = 1.0}$	**0.00119**
exp step size decay	$\xi = 0.5,\ s = 1.5$	0.00258
exp step size decay	$\xi = 0.5,\ s = 2.0$	0.00120
exp step size decay	$\xi = 0.25,\ s = 2.0$	0.01726
exp step size decay	$\xi = 0.75,\ s = 2.0$	0.01843
adaptive step size decay	$l = 4,\ \tau = 0$	0.01496
adaptive step size decay	$l = 8,\ \tau = 0$	0.00255
adaptive step size decay	$l = 10,\ \tau = 0$	0.00293
adaptive step size decay	$l = 10,\ \tau = 0.2$	0.00293
adaptive step size decay	$l = 10,\ \tau = 0.5$	0.00293
adaptive step size decay	$l = 10,\ \tau = 1.0$	0.00293

Table 6.1: Overview of DSEA+ parameter optimization. The highlighted settings will be used within this dissertation.

6.5 Variable Selection

The selection of unfolding variables can be justified through coverage and bias tests, which examine the stability of DSEA+ to statistical fluctuations. A subsample of 100 000 simulated, resampled atmospheric events is randomly divided into two-thirds for algorithm training and one-third for testing (unfolding). This process is repeated over 2000 trials. A suitable variable selection should result in coverage within one standard deviation and minimal bias. The feature importance for the RF are : 8% for `L5_nch`, 3% for `L5_ndir_c`, and 89% for `Etrun`. Fig. 6.3(e) indicates that the performance slightly worsens for a node split that utilizes three variables. Subsequent sections will explore whether the variable `L5_ndir_c` is substantial for the unfolding.

6.5.1 Coverage Test

The coverage test assesses the containment of the unfolded result within statistical uncertainties to identify if the uncertainties are overestimated or underestimated. The coverage is defined as

$$c_i = \text{coverage}_i = \frac{f_{\text{est},i} - f_{\text{true},i}}{\sigma_i}, \tag{6.13}$$

with the unfolded number of events $f_{\text{est},i}$ per energy bin i, the true number of events $f_{\text{true},i}$, and the standard deviation

$$\sigma_i = \left(\sum_n \sqrt{c_M(i \mid x_\text{n})} \right)^2 \tag{6.14}$$

under the assumption of Poisson statistics. The discrepancy between the unfolded number of events and the MC truth per bin should not exceed one standard deviation. In this scenario, the variable selection would add further uncertainties to the outcome. In case the deviation is well-contained within one standard deviation, the statistical uncertainty is underestimated, as it is a relatively conservative measure. The confidences c_M of the classifier outputs can be determined with DSEA+, which is one advantage compared to other unfolding algorithms.

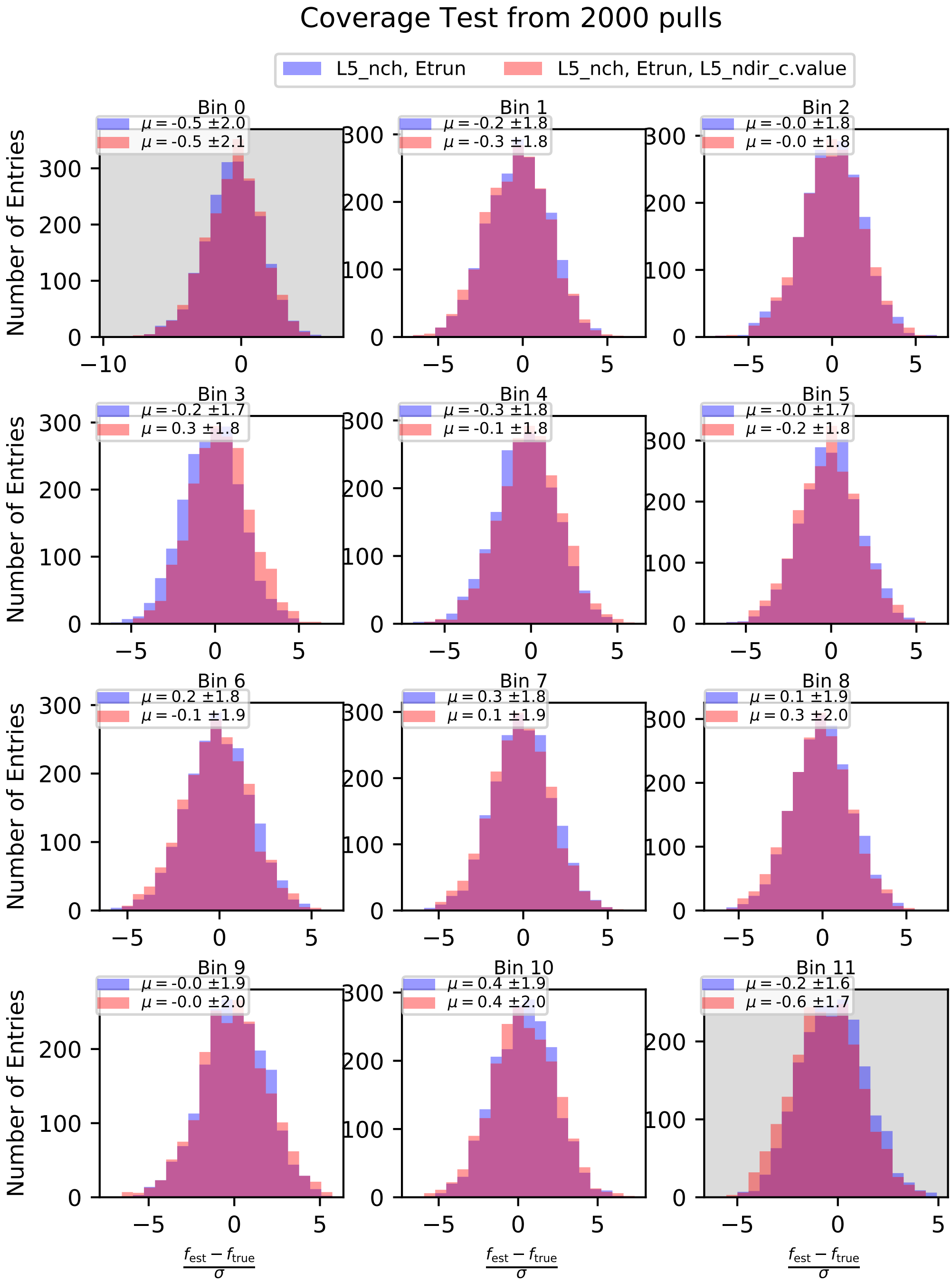

Figure 6.5: Coverage test of the unfolding variables with and without `L5_ndir_c`. The mean and the corresponding standard deviation are calculated for each bin. Bin 0 and 11 denote underflow and overflow bins, respectively.

6.5.2 Bias

The bias test examines if the chosen variables introduce additional bias into the unfolded event spectrum, measuring the deviation from the MC truth:

$$b_i = \mathrm{bias}_i = \frac{f_{\mathrm{est},i} - f_{\mathrm{true},i}}{f_{\mathrm{true},i}}. \tag{6.15}$$

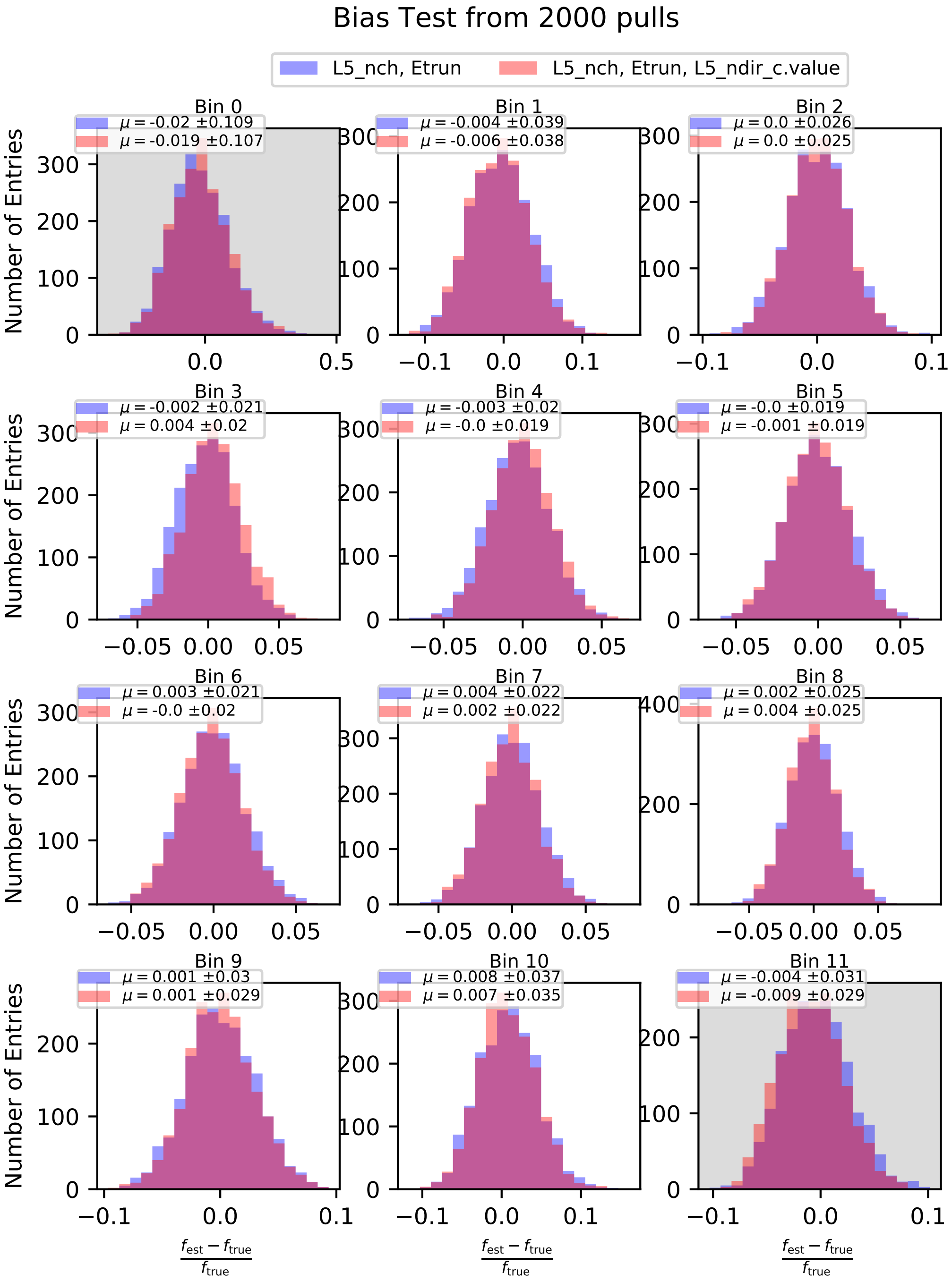

Figure 6.6: Bias test of the unfolding variables with and without `L5_ndir_c`. The mean and the corresponding standard deviation are calculated for each bin. Bin 0 and 11 denote underflow and overflow bins, respectively.

6.5.3 Final Remarks

Both variable combinations yield similar results in both tests, as presented in Table 6.2. Bias and Coverage are slightly improved excluding the third variable `L5_ndir_c`, with a mean absolute coverage of 0.20 and bias of 0.0043, disregarding statistical uncertainties. The redundancy of the direct hits variable was previously indicated in the feature importance at each node in the RF classifier, as depicted in Fig. 6.3(e). Therefore, in this dissertation only two variables will be used in this dissertation: `L5_nch` and `Etrun`. The comparison of both variables to data is shown in Fig. 5.7.

Bin	**Coverage Test**		**Bias Test**	

	`L5_nch`
	`Etrun`
	`L5_ndir_c`
		`L5_nch`
		`Etrun`
			`L5_nch`
			`Etrun`
			`L5_ndir_c`
				`L5_nch`
				`Etrun`

1	-0.3 ± 1.8	-0.2 ± 1.8	-0.006 ± 0.038	-0.004 ± 0.039
2	-0.0 ± 1.8	-0.0 ± 1.8	$+0.000 \pm 0.025$	$+0.000 \pm 0.026$
3	-0.3 ± 1.8	-0.2 ± 1.7	$+0.004 \pm 0.020$	-0.002 ± 0.021
4	-0.1 ± 1.8	-0.3 ± 1.8	-0.000 ± 0.019	-0.003 ± 0.020
5	-0.2 ± 1.8	-0.0 ± 1.7	-0.001 ± 0.019	-0.000 ± 0.019
6	-0.1 ± 1.9	$+0.2 \pm 1.8$	-0.000 ± 0.020	$+0.003 \pm 0.021$
7	$+0.1 \pm 1.9$	$+0.3 \pm 1.8$	$+0.002 \pm 0.022$	$+0.004 \pm 0.022$
8	$+0.3 \pm 2.0$	$+0.1 \pm 1.9$	$+0.004 \pm 0.025$	$+0.002 \pm 0.025$
9	-0.0 ± 2.0	-0.0 ± 1.9	$+0.001 \pm 0.029$	$+0.001 \pm 0.030$
10	$+0.4 \pm 2.0$	$+0.4 \pm 1.9$	$+0.007 \pm 0.035$	$+0.008 \pm 0.037$
0	-0.5 ± 2.1	-0.5 ± 2.0	-0.019 ± 0.107	-0.020 ± 0.109
11	-0.6 ± 1.7	-0.2 ± 1.6	-0.009 ± 0.029	-0.004 ± 0.031
Abs. mean	0.24	**0.20**	0.0044	**0.0043**

Table 6.2: Coverage and bias test results for each energy bin. The final selection is determined by comparison of the mean value averages.

7 Seasonal Variations in the Zenith Range from 90° to 120°

This chapter presents the main findings of this thesis, the unfolded seasonal spectra of atmospheric muon neutrinos, and the resulting seasonal variation of the flux in the zenith range from 90° to 120°. The estimation of statistical and systematic uncertainties is described in the first two sections. Afterwards, the analysis chain is presented and the expected results from simulation studies are shown. The last section discusses the determined seasonal variations monthly and compares the obtained results to the theoretical predictions from MCEq.

Parts of this chapter are contained in conference proceedings of the author, in particular, Ref. [150, 127].

7.1 Estimation of Statistical Uncertainties

DSEA+ does not contain a measure of statistical uncertainties of the unfolded spectrum. This can be solved with an estimation of statistical uncertainties with a bootstrap method (refer to Chapter 4.1). The generated sub-samples from sampling with replacement are divided into monthly and seasonal datasets based on the timing information and then unfolded. The number of events per energy bin is determined afterward by scaling the obtained PDF to the total number of events in a specific season. The bootstrap approach is repeated over 2000 pulls. A detailed description of the analysis chain can be found in Section 7.3.

Fig. 7.1 and 7.2 display the distribution of the bootstrap pulls in each energy bin exemplary for the season from June to August. The distributions are analogous for all seasons but with different numbers of events per energy bin. The distribution of the obtained number of events in each bin can be approximated by a Gaussian fit, depicted in red. The standard deviation and mean are calculated for each pull distribution and compared to the fit. Since both are compatible, the

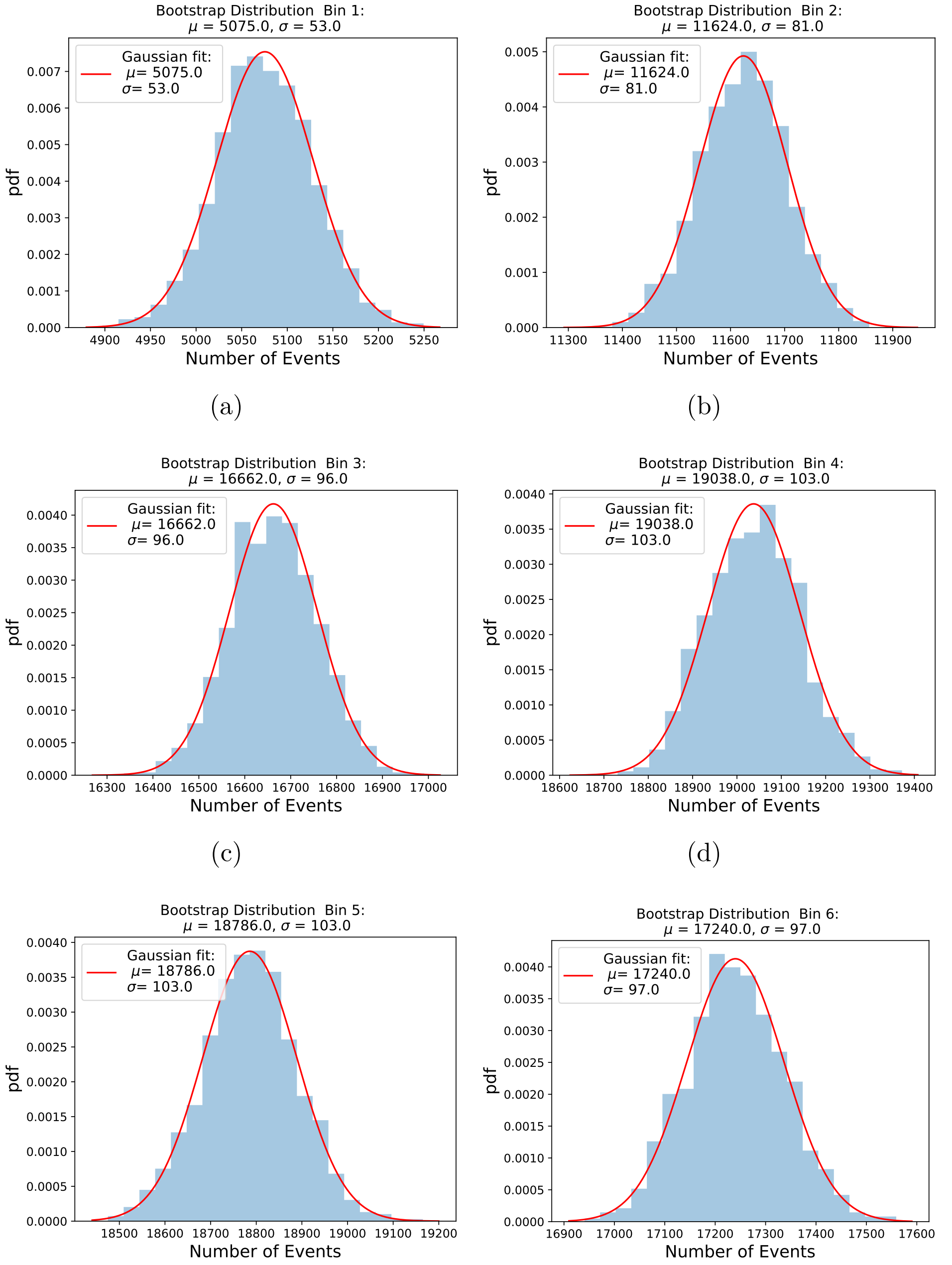

(a) (b)

(c) (d)

(e) (f)

Figure 7.1: Distribution of the bootstrap pulls for the season from June to August per energy bin. A Gaussian is fitted to the pull distribution. The mean and standard deviation are compared to the calculated values from the distribution.

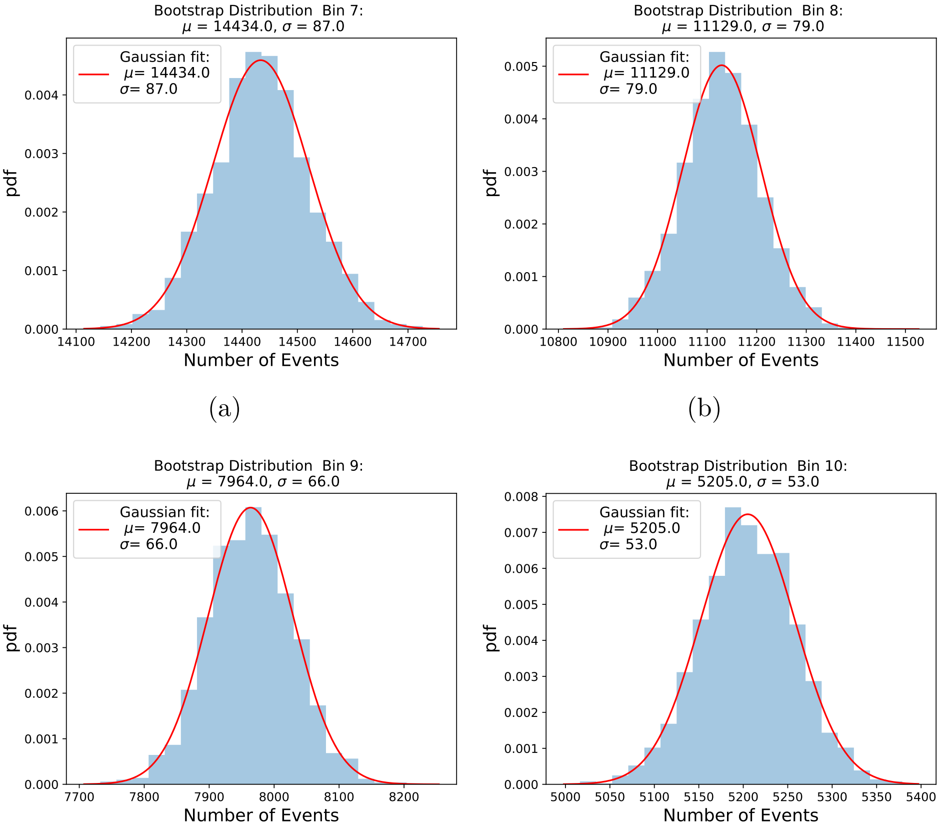

(a)

(b)

(c)

(d)

Figure 7.2: Distribution of the bootstrap pulls for the season from June to August per energy bin. A Gaussian is fitted to the pull distribution. The mean and standard deviation are compared to the calculated values from the distribution.

standard deviation of the pull distribution is used as an approximation of the statistical uncertainty for the unfolded number of events per energy bin. Correspondingly, the unfolded number of events per season per energy bin is determined by the mean of the pull distributions.

7.2 Systematic Uncertainties

The unfolded spectrum is subject to systematic uncertainties resulting from the detector setup, event reconstruction, or the robustness of the unfolding algorithm DSEA+. The impact of each source of uncertainty is accessible by unfolding pseudo samples, which are generated from a maximum variation of a systematic parameter. The difference between the unfolded pseudo spectra and the reference sample is defined as the upper/lower uncertainty of the unfolded spectrum attributed to a respective parameter. The same approach for the estimation of systematic uncertainties is employed in the neutrino spectrum unfolding with IceCube [151, 152], and its counterpart the Astronomy with a Neutrino Telescope and Abyss environmental RESearch (ANTARES) [153] experiment in the Mediterranean Sea. The utilized method tends to overestimate individual uncertainties because the respective uncertainties are solely determined based on the maximum increase/decrease of the parameter. Correlations between different uncertainties are not taken into account. At the developmental stage of this thesis, only discrete simulation sets, consisting of maximum, mean, and minimum fixed values of a systematic parameter, were available. Recently, a new approach for the treatment of uncertainties explained in Ref. [154] has been developed, where each event is simulated from a different combination of systematic parameters. However, these simulations were not available in the development stage of this dissertation.

Unfolding a pseudo sample, which is simulated from varied systematic parameters, yields a different spectrum for the unfolded one from the reference sample. It shows not only the impact of the systematic parameter on the unfolded spectrum but also the robustness of DSEA+ in unfolding a spectrum that deviates from the sample the algorithm was trained with. The final systematic uncertainty is determined by the addition of each systematic uncertainty in quadrature:

$$\sigma_{\text{sys}} = \sqrt{\sigma^2_{\text{DOM}} + \sigma^2_{\text{abs}} + \sigma^2_{\text{scat}} + \sigma^2_{\text{holeice}} + \sigma^2_{\text{flux}}}. \tag{7.1}$$

σ_{DOM} describes the uncertainties attributed to the quantum efficiency of the optical modules, σ_{abs} and σ_{scat} denote the uncertainty of the reconstruction due to absorption and scattering in ice, σ_{holeice} depicts the reconstruction uncertainty from the re-frozen ice around the strings, and σ_{flux} the impact on uncertainties from hadronic interaction and primary cosmic ray composition on the neutrino flux. Equ. 7.1 is evaluated separately for both the upper and lower limits of each respective source of uncertainty. The presented determination of uncertainties is independent of the size of the dataset because the uncertainty is defined as a ratio to the reference simulation. In the Appendix, the impact of each source of uncertainty on the unfolded event spectrum of the pseudo sample is summarized in Fig. B.6. The simulation sets with varied systematic parameters are shown in Table A.1. Each determined systematic parameter is outlined in the subsequent paragraphs.

7.2.1 Optical Modules

The uncertainty attributed to the optical modules σ_{DOM} is determined by the detection efficiency of the DOMs. The main source of uncertainty is the PMT inside the DOM, among others the wavelength-dependent PMT response, discriminator threshold effects, and photocathode non-uniformity. The PMT quantum efficiency is measured in a laboratory environment using a single photoelectron laser at 337 nm. These measurements are combined into a model of DOM uncertainties with measurements of Cherenkov photons induced by muons in ice. It accounts for cable shadowing effects, the refreezing process around the DOMs, optical absorption in the DOM glass and gel, and the angular dependence of the detection efficiency [5]. The final DOM efficiency ϵ_{DOM} is normalized to $\epsilon_{\text{DOM}} = 1.0$ as the reference value, the total uncertainty of the DOM efficiency is set to $\pm 10\%$. This measurement is conservative, and recent simulations have decreased the uncertainty to $\pm 5\%$. A higher quantum efficiency leads to a more sensitive detection threshold, for which more PMTs would be triggered by the same Cherenkov light yield of an induced muon. On the contrary, a reduced efficiency results in less triggered DOMs for an event of the same energy.

7.2.2 Detection Medium

A significant source of uncertainty in event reconstruction stems from the understanding of glacial ice as a detection medium. While ice has good absorption properties, the comprehension of scattering effects within the ice and the resulting delay in hit measurements is essential for any analysis. The understanding of the impact of photon propagation through ice is accumulated in ice models. The bulk ice behavior is influenced by the depth-dependent concentration of impurities, such as dust and volcanic ash. It is determined via measurements obtained from flasher LEDs on the DOMs, as depicted in Fig. 3.2. The simulations used in this thesis are created with the *SPIceMie* model [155], which accounts for absorption and scattering effects by Mie scattering. A newer model, *SPIceLea* [156], extends the previous version to an anisotropic absorption and scattering component in the xy-plane. The impact of the ice tilt, which makes the IceCube detector move downward at a rate of $10\,\text{m}\,\text{year}^{-1}$, has not yet been incorporated into any ice model [157]. The simulation set is available for different absorption, scattering, and hole ice parameters individually.

Absorption

The absorption coefficient is given by

$$\alpha(\lambda) = \alpha_{\text{dust}}(400\,\text{nm}) \cdot \left(\frac{\lambda}{400\,\text{nm}}\right)^{-\kappa} + A\exp\{-{}^{B}\!/\!{}_{\lambda}\} \cdot (1 + 0.01\delta\tau), \quad (7.2)$$

with the absorption due to dust α_{dust} and the temperature-dependent light absorption in ice $\delta\tau$ [157]. Coefficients are defined in Ref. [158]. The uncertainty of the absorption coefficient is estimated to be ±5% in the simulation at hand.

Scattering

Light scattering is a significant phenomenon in ice, as it causes a delay in detecting incoming photon hits due to ice impurities (see Equ. 3.3). The scattering coefficient is defined as in Ref. [157]:

$$s(\lambda) = s(400\,\text{nm}) \cdot \left(\frac{\lambda}{400\,\text{nm}}\right)^{-\alpha}. \quad (7.3)$$

The coefficients are specified in Ref. [158]. The uncertainty of the scattering coefficient is set to ±5% in the simulation.

Hole-ice

The IceCube strings were embedded into the ice in drilled holes of 60 cm diameter with a hot water drill. The refrozen ice around the strings has different optical properties than the surrounding glacial ice. The Swedish camera monitors the ice at a depth of 2450 m and recorded the refreezing process. Bubbles are more abundant in the ice inside the drilled holes compared to the surrounding bulk ice. As a consequence, the scattering and absorption around the strings must be modeled differently. Furthermore, the DOMs are positioned on the perimeter of the borehole, covering $^2\!/_3$ of its diameter, adding further complexity to the ice model [157].

7.2.3 Flux Model

Another source of systematic uncertainties arises from model assumptions for the weighting of the simulation sample. The choice of the flux models imprints uncertainties on both, the training sample for DSEA+, and the generation of pseudo samples for the uncertainty estimation of all parameters introduced above. As the weights are composed of an atmospheric flux prediction from MCEq and an assumption on the astrophysical flux, the impact of the model choices and their uncertainties on the weighting needs to be propagated. The uncertainty attributed to the atmospheric flux calculation from MCEq is governed by uncertainties in CR composition and hadronic interaction model uncertainties, and how they propagate onto lepton fluxes. In addition, uncertainties in the atmospheric flux model would need to be accounted for as well. However, NRLMSISE-00 is currently the only atmospheric model in MCEq that accounts for monthly temperature variations (see Appendix D), and the corresponding uncertainty cannot be investigated yet. The uncertainty of the astrophysical flux is negligible in the energy range of interest, as this component only becomes a significant contribution to the total flux at higher energies.

Energy / GeV	Lower Limit / %	Upper Limit / %
100 GeV	−23	32
1 TeV	−22	42
10 TeV	−30	47

Table 7.1: Uncertainties from the variation of CR composition and hadronic interaction models on the neutrino flux calculation, as determined in Ref. [159]. These reference values are used for the interpolation of the flux weight uncertainty of each simulated event.

Since the total flux uncertainty is not attributed to the detector or reconstruction, a simulation with varied parameters is not available. Therefore, two pseudo samples are generated from the reference simulation by weighting to the uncertainties of the neutrino flux rising from uncertainties in CR composition and hadronic interaction models. The propagation of these uncertainties on the neutrino flux can be determined by the variation of models in the calculation, which has been calculated in Ref. [159] for three respective energies, depicted in Table 7.1, and interpolated in between. The uncertainty of individual events in the simulation is calculated by log-linear interpolation between the reference values. The simulated events are sampled according to the upper and lower uncertainties added into the calculated neutrino flux from MCEq to create an upper and lower limit on the flux per event in the simulation.

7.2.4 Summary

The obtained uncertainties reflect their effect on the unfolded spectrum rather than those of the parameter itself. In Fig. 7.3, the systematic uncertainties are displayed by energy bin per source. As the increase/decrease of a systematic parameter does not affect each bin uniformly, the uncertainties are asymmetric. The uncertainties are larger in bins with fewer statistics, the first two and the last two bins. These bins have substantially lower statistics than the other bins, as can be seen in Fig. 7.1 and 7.2. The deviation of the unfolded pseudo sample from varied systematic parameters to the reference sample is shown in detail in Fig. B.6 in the Appendix. The DOM efficiency significantly affects the systematic uncertainties, along with the ice model parameters. The uncertainties from the flux model applied to the weighting have a minor impact on the unfolded spectrum.

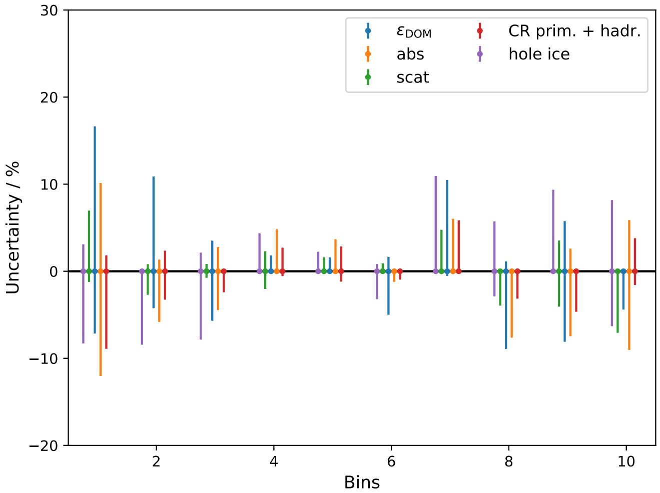

Figure 7.3: Overview of each source of systematic uncertainty per energy bin. The obtained systematic uncertainties remain constant for all seasons because of the relative uncertainty estimation.

7.3 Analysis Chain

All determined seasonal spectra in this thesis are deconvolved with DSEA+ with optimized settings discussed in Chapter 6.4. The algorithm is trained on 100 000 randomly selected events from the MC sample weighted to a realistic flux scenario, as explained in Chapter 5.3.1. The given number of events is considered sufficient for training once the parameters are fixed. The accuracy of the unfolded spectrum was found to not improve by an increase in the training sample size, as explained in Appendix B.2.

The seasonal variation measurement is conducted as follows: The entire dataset is bootstrapped, sorted into seasonal sets, and unfolded, as explained in Section 7.1. The individual unfolded number of events per energy bin is saved for each of the 2000 pulls. Reproducibility of the unfolding process is ensured by the selection of the same random seed for each season in each respective bootstrap iteration.

In this dissertation, the obtained seasonal variations are displayed in two ways. Firstly, the differential seasonal fluxes are by E^3 to make changes in the seasonal spectra observable. The unfolded spectra are shown in comparison to the MCEq predictions (with H3a as primary composition, Sibyll2.3c as hadronic interaction model, and NRLMSISE-00 as the atmospheric model) for the respective seasons and the annual average. Secondly, the ratio of the seasonal fluxes to the annual average flux, referred to as seasonal variation strength, is calculated. The ratio is only affected by statistical uncertainties because systematic uncertainties are independent of the season (see Section 7.2). Consequently, the intensity of the seasonal variation in each energy bin can be evaluated on a percentage level, which is the main objective of this dissertation.

7.4 Expected Results

Before the unfolding of the actual datasets, the expected results are determined by the unfolding of pseudo samples. These pseudo samples are constructed from simulated events weighted to the seasonal and monthly predictions from MCEq. The number of events is set to the expected number of neutrinos from the event selection in Chapter 5.1

in 11.5 years of data. This test ensures that the spectrum unfolding and the determination of the seasonal variation strength are feasible with the dataset at hand. Fixing the number of events in the pseudo samples to the expected number of events in the data allows to estimate statistical and systematic uncertainties and to determine the measurement accuracy.

7.4.1 Unfolding of Pseudo Samples

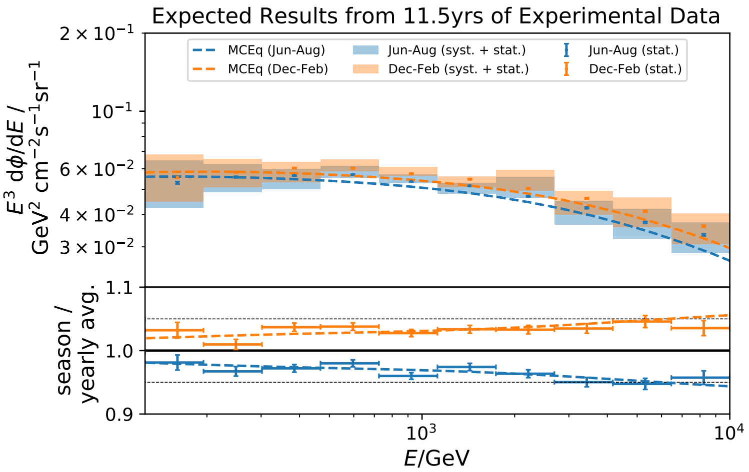

Figure 7.4: Expected results for the seasonal unfolding of June to August and December to February for 11.5 years of data from the unfolding of pseudo samples. Error bars depict statistical uncertainties while colored bands depict systematic ones. The predicted flux from MCEq is scaled up by a fitted normalization constant for the unfolded spectrum. The lower panel displays the ratio of the seasonal to annual average flux for the unfolded data and the MCEq-calculated theory fluxes. Black dashed lines illustrate ±5% deviation from the annual average flux. Since the systematic uncertainties remain the same for each season and cancel out in the ratio, the statistical uncertainties are the only uncertainties in the ratio.

Fig. 7.4 depicts the unfolded pseudo samples for austral summer from December to February, and austral winter from June to August, for the same seasons as shown in Fig. 2.10. Statistical uncertainties are indicated by error bars, while systematic uncertainties are presented as shaded bands. The unfolded seasonal spectra are consistent with the expectation computed with MCEq. The determined ratio of seasonal to annual mean flux indicates the variation strength, which is consistent with the prediction. This study demonstrates the feasibility of seasonal unfolding using 11.5 years of IceCube data. However, further investigation in the next section will quantify the agreement of the predicted ratio of seasonal to annual average flux with the prediction.

7.4.2 χ^2-Test

A χ^2- test (see definition in Chapter 4.5) is performed to investigate how accurately the strength of the seasonal variation, the ratio of the flux of a given season to the annual mean, can be unfolded. Pseudo Samples are generated with the expected number of events from 2011 to 2022. The pseudo samples are weighted to the seasonal MCEq predictions and unfolded. To determine whether the unfolded flux ratios of the pseudo samples are consistent with the predicted ratios from MCEq, the quotient of the two is calculated. The quotient equals one when the predicted and unfolded ratios of the seasonal to annual average flux are the same concerning uncertainties. The null hypothesis to be rejected in the test is defined as a quotient of one. The rejection threshold is set at 3σ, equivalent to p-values ≤ 0.003.

The test results for austral summer and winter are depicted in Fig. 7.5. The ratio of the unfolded seasonal variation strength to the MCEq prediction is depicted for each energy bin. The quotient between the unfolded to the predicted ratio is fitted by a linear function with respect to statistical uncertainties to display the slope of the deviations. The quotient is consistent with one, indicating that the null hypothesis cannot be rejected. Therefore, it can be concluded that the MC truth, the seasonal flux ratio, can be determined from the unfolding. Furthermore, the robustness of the unfolding of a spectrum that deviates in the spectral index from the training spectrum is investigated in Appendix B.5.2.

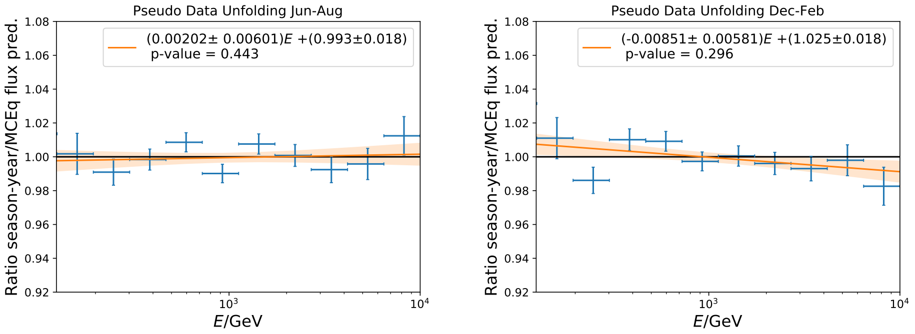

(a)

(b)

Figure 7.5: χ^2-test to determine the accuracy of the unfolded seasonal to annual average in zenith range from 90° to 120°. The target of the test is the quotient of the unfolded seasonal flux ratio to the prediction for each energy bin. The null hypothesis that should be rejected is defined as a quotient of one. This implies that the unfolded ratio is in agreement with the prediction. The linear fit determines the slope of the ratio between unfolded ratio from pseudo data to MCEq. The unfolded ratio from the pseudo sample should be compatible with the prediction to ensure the feasibility of seasonal unfolding. The null hypothesis cannot be rejected for both seasons, which indicates that the unfolded ratio is in agreement with the prediction.

7.5 Measurement of Seasonal Variations

This section discusses the seasonal unfolded spectra and variation strengths for the zenith range from 90° to 120°. The deviation of the seasonal unfolded flux to the annual average is quantified in a χ^2-test. Furthermore, the compatibility of the unfolded ratio to the MCEq predictions is investigated in a second χ^2-test.

7.5.1 Summer-Winter Split

Fig. 7.6 depicts the unfolded spectra for austral summer (December to February) and winter (June to August), as discussed in the previous section. The MCEq-calculated fluxes show a lower normalization than the unfolded spectra. The normalization is scaled up by 25%. This scaling factor is determined by fitting the MCEq normalization to the unfolded spectrum. The fit is obtained with respect to statistical and

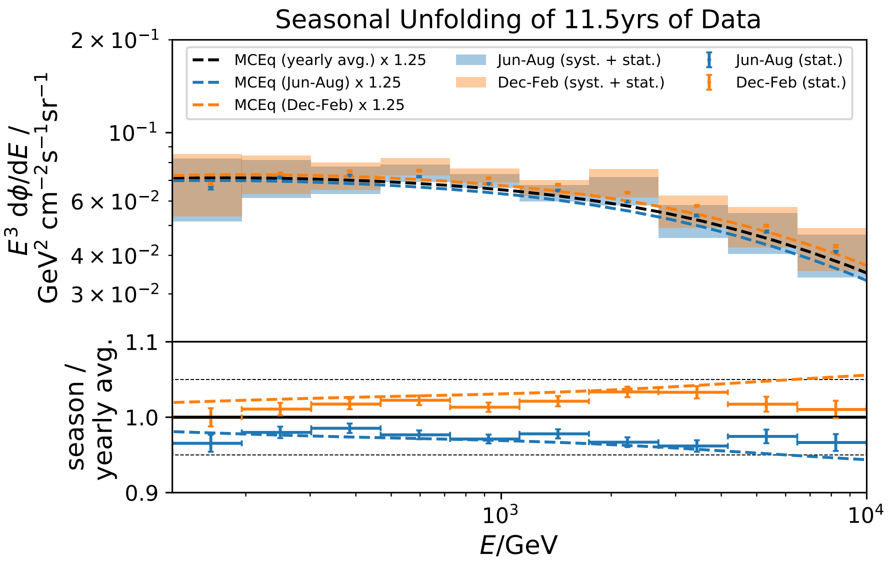

Figure 7.6: Unfolded seasonal muon neutrino spectra for austral summer and winter [127]. Error bars depict statistical uncertainties while colored bands depict systematic ones. The predicted flux from MCEq is scaled up by a fitted normalization constant for the unfolded spectrum. The lower panel displays the ratio of the seasonal to annual average flux for the unfolded data and the MCEq-calculated theory fluxes. Black dashed lines illustrate ±5% deviation from the annual average flux. Since the systematic uncertainties remain the same for each season and cancel out in the ratio, the statistical uncertainties are the only uncertainties in the ratio.

systematic uncertainties in an asymmetric loss function, minimized by the Nelder-Mead algorithm [160]. As discussed in Chapter 5.5, the measurement of approx. 20% more data is a common observation in other measurements of atmospheric muon and neutrino fluxes. The fitted normalization of the predicted fluxes allows a comparison of the shapes of the unfolded and the predicted spectrum. The scaled normalization of the MCEq prediction cancels in the calculation of the ratio of seasonal to annual average flux so that is does not impact the calculated variation strength.

The unfolded seasonal spectra are in agreement with the calculated fluxes from MCEq. The observed spectrum is mostly flat when scaled with E^3 below 500 GeV due to threshold effects, and the flux decreases with energy. The amplitude of the seasonal variation strength increases with energy up to 4 TeV with $(-3.8 \pm 0.8)\%$ for the season from June to August, yielding a reduction in the neutrino flux, as expected by MCEq. The variation strength for the season from December to February increases from $(0.0 \pm 1.2)\%$ at 125 GeV to $(+3.3 \pm 0.8)\%$ at 4 TeV. Seasonal variations are expected to increase with energy as the probability of reinteraction of the parent mesons increases compared to direct decays due to the temperature-dependent critical energy of the specific parent meson (see explanation in Chapter 2.5). On the contrary, neutrinos with higher energies are produced in showers of high-energy primary CRs, which interact at higher altitudes in the atmosphere, where the amplitude of temperature variations is larger (see Fig. 8.1). However, the strength of the variation decreases for both seasons above 4 TeV to a variation strength of $(-3.4 \pm 1.1)\%$ for the season from June to August and a variation strength compatible with the annual average with $(+1.0 \pm 1.2)\%$ for the season from December to February from 7 TeV to 10 TeV. The unfolded seasonal spectrum deviates from the annual average at 10.4σ for the season from June to August, and 12.3σ for December to February.

7.5.2 Half-year Split

As a consistency check, the dataset is divided into half-year subsets from January to June and July to December. Assuming symmetric temperature modulations throughout the year, such as the NRLMSISE-00 atmospheric model, both splits are expected to be consistent with the annual average. Fig. 7.7 illustrates that the unfolded spectra and ratios are consistent with the scaled predictions from MCEq. No seasonal variations are observable with respect to statistical uncertainties. The observed deviation is not significant, with 0.3σ for the first half from January to June, and 0.2σ for the second half from July to December.

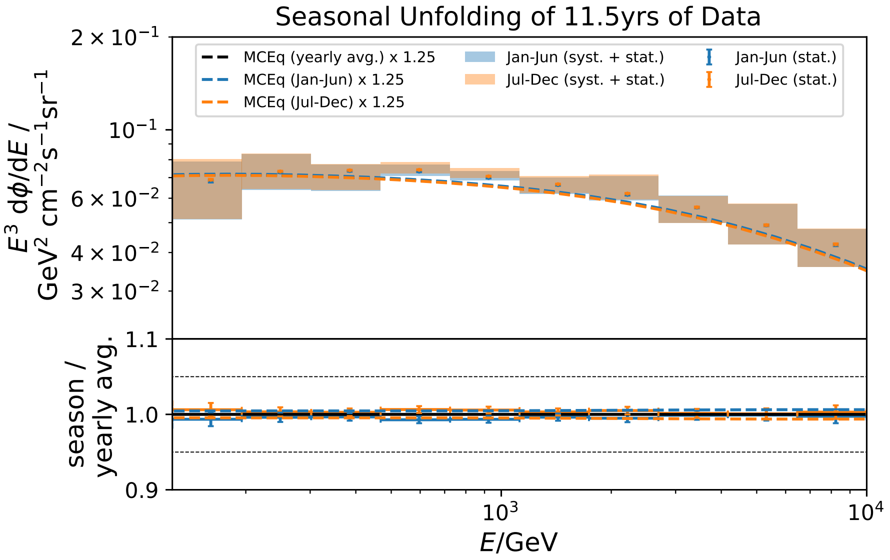

Figure 7.7: Unfolded seasonal muon neutrino spectra for the half-year splits. Error bars depict statistical uncertainties while colored bands depict systematic ones. The predicted flux from MCEq is scaled up by a fitted normalization constant for the unfolded spectrum. The lower panel displays the ratio of the seasonal to annual average flux for the unfolded data and the MCEq-calculated theory fluxes. Black dashed lines illustrate ±5% deviation from the annual average flux. Since the systematic uncertainties remain the same for each season and cancel out in the ratio, the statistical uncertainties are the only uncertainties in the ratio.

7.5.3 Monthly Variations

As indicated in the feasibility study on simulated events in Fig. B.7 to B.8 in the Appendix, the data sample contains sufficient statistics to perform monthly spectrum unfolding. The ratios of monthly to annual average flux are illustrated in Fig. 7.8 and 7.9 compared to the MCEq predictions in dashed lines. The unfolded monthly spectra are not shown in this section as the spectra themselves cannot be distinguished within the systematic uncertainties of the unfolded spectrum (see Fig. 7.6 and 7.7).

The strength of the variation in January is largely consistent with the MCEq prediction but tends to be lower in a few energy bins. In contrast, the predicted variations for February exceed the observed values, and the unfolded ratio decreases above 4 TeV. The seasonal variations for March and April are consistent with the annual average flux and fluctuate around a ratio of 1, which is in agreement with MCEq. The unfolded ratios for May and June are similar and decrease with energy, but a decrease of the variation strength is observed for June above 4 TeV. This decrease is not expected by MCEq. The unfolded ratio for July shows a consistent decreasing ratio with increasing energy over the entire energy range, as expected by MCEq. Despite the prediction, the unfolded ratio for August remains constant over the whole energy range. The unfolded flux ratio for September aligns with the annual average, contrary to the MCEq prediction. The seasonal variation strength is mostly constant for October at approx. $(+2.0 \pm 1.0)\%$, where no variations are predicted by MCEq. The unfolded ratio for November is approximately the same, except for a sudden increase to $(+7.1 \pm 1.9)\%$ between 7 TeV to 10 TeV. The unfolded ratio for December is in agreement with the MCEq prediction and shows an increasing variation strength up to 4 TeV, above which the ratio decreases.

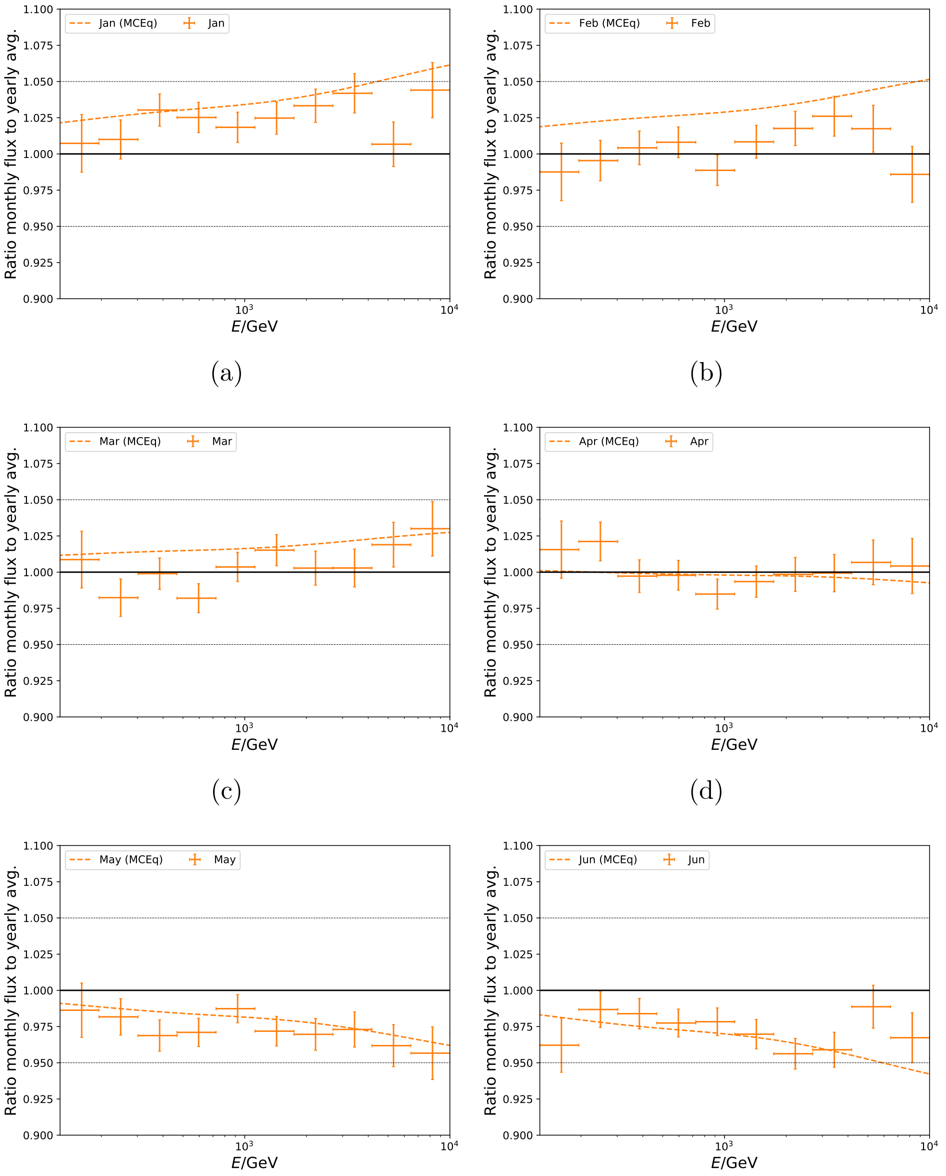

(a) (b)

(c) (d)

(e) (f)

Figure 7.8: Ratio of the unfolded monthly to the average annual flux. The corresponding MCEq predictions are depicted in dashed lines. The error bars denote the statistical uncertainty of the ratio.

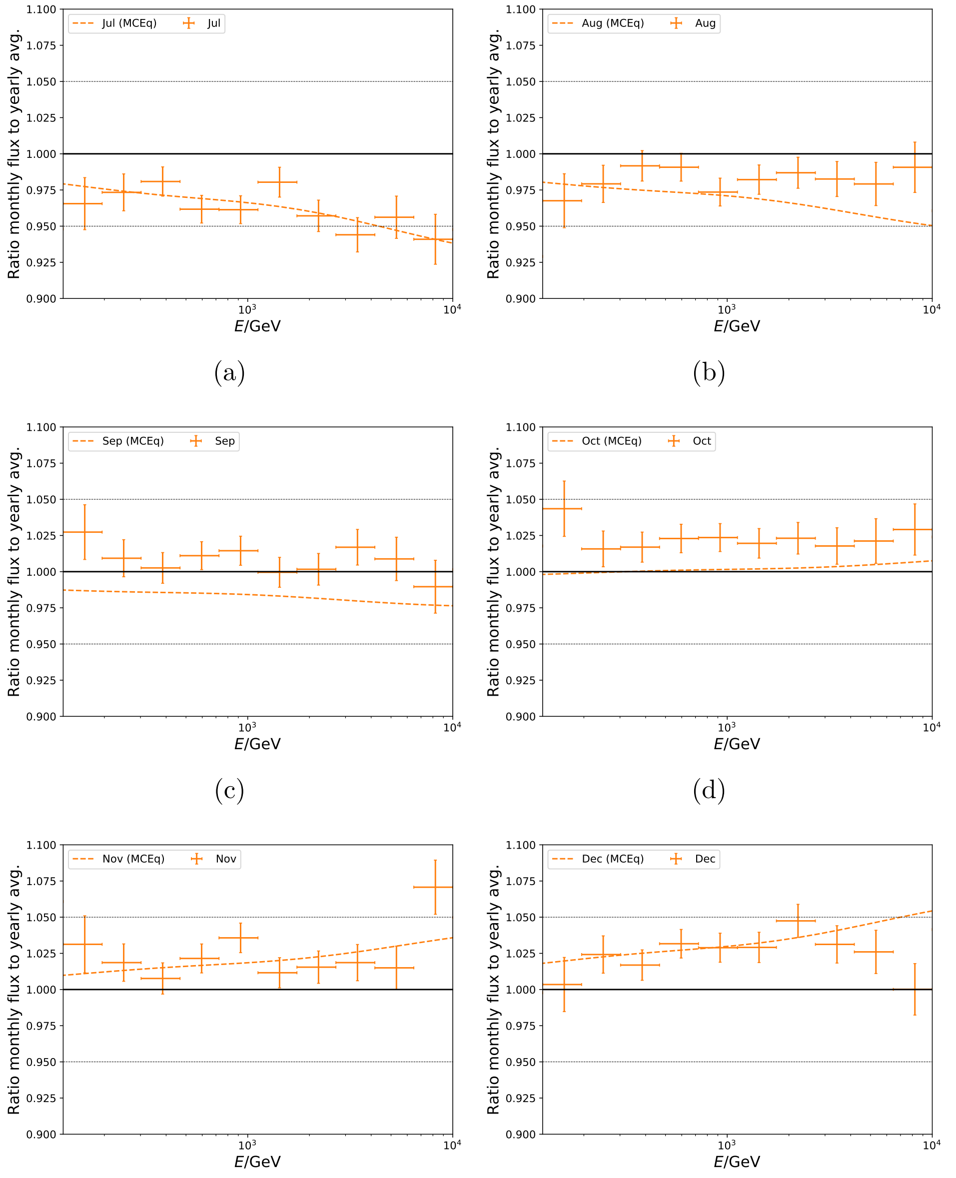

(a) (b) (c) (d) (e) (f)

Figure 7.9: Ratio of the unfolded monthly to the average annual flux. The corresponding MCEq predictions are depicted in dashed lines. The error bars denote the statistical uncertainty of the ratio.

7.5.4 Agreement to MCEq Predictions

As discussed in the previous part, the observed seasonal variation pattern differs from the MCEq predictions for several months. To quantify the deviation from the predicted seasonal to annual average flux by MCEq, a χ^2-test is conducted. The deviation from the prediction is measured by the quotient of the unfolded ratio of seasonal to annual average flux, similar to the previously discussed test in Section 7.4.2. The null hypothesis is defined as a quotient of one, which is equivalent to the agreement between the unfolded and predicted seasonal flux ratio. The rejection threshold is set at 3σ, corresponding to p-values ≤ 0.003.

The presented test investigates the deviation of the unfolded seasonal flux ratio to the calculated prediction from MCEq, which is given for a particular selection of hadronic interaction and CR composition model. The investigation on the comparison of the calculated flux ratios (refer to Appendix B.4.2) based on different model combinations shows that the ratio is approx. the same for the iteration of models in the energy range from 125 GeV to 10 TeV. Thus, the test investigates the deviation to the predicted flux, which is attributed to the selected atmospheric model NRLMSISE-00.

The tests for austral summer and winter are displayed in Fig. 7.10. The quotient of the unfolded seasonal variation strength to the prediction from MCEq is depicted for each energy bin. A ratio of 1 implies that the unfolded variation strength is in agreement with the calculation. The determined seasonal variations strength for austral winter from June to August is still compatible with the MCEq prediction, as the null hypothesis cannot be rejected with $p = 4.39 \times 10^{-2}$. However, the variation strength is smaller for austral summer from December to February than expected, and the MCEq hypothesis is rejected with $p = 7.12 \times 10^{-6}$. The test results for all months and seasons are depicted in Appendix B.5.3 (see Fig. B.13 to B.15). An overview of the calculated p-values is given in Table 7.2 and the main findings are summarized in the next paragraph.

Referring to the half-year splits in Fig. 7.7, the null hypothesis is rejected for January to June with $p = 2.38 \times 10^{-3}$. The null hypothesis cannot be rejected for July to December with $p = 4.00 \times 10^{-3}$. As observable in Fig. 7.11 and 7.12 the unfolded ratios for each the maximum and minimum are in agreement with the MCEq prediction, and the mismatches occur in the spring and fall seasons. Therefore, an off-

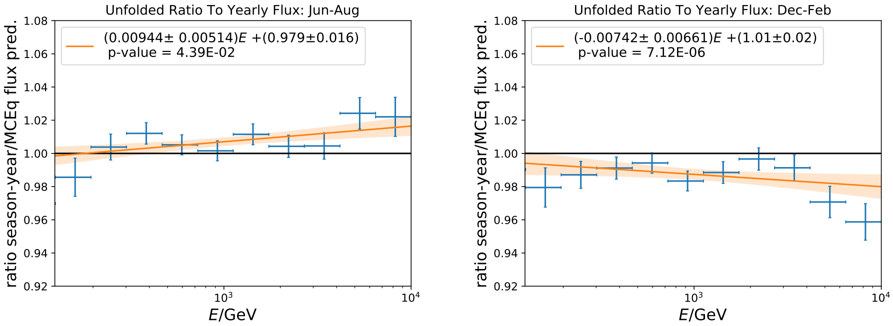

(a) (b)

Figure 7.10: χ^2-test to determine the deviation of the unfolded seasonal flux ratios to the prediction from MCEq. The error bars depict statistical uncertainties in the ratio from the unfolding. The null hypothesis that should be rejected is defined as a quotient of the seasonal flux ratio to the prediction of one, implying that the unfolded ratio is in agreement with the prediction. The p-value for each season is given in the caption. The ratio of the unfolded results to the MCEq prediction is fitted by a linear function to show potential offsets to the prediction.

set to the annual average flux is observed in the ratio of the half-year splits to the annual average. The variations predicted for February are larger than the observation, which cannot be described by MCEq. The null hypothesis is rejected with $p = 1.76 \times 10^{-6}$. The consecutive seasons are in agreement with the MCEq prediction. However, the unfolded ratio for September and October do not match the prediction and the MCEq flux can be rejected with $p = 3.14 \times 10^{-6}$ for September and $p = 1.41 \times 10^{-3}$ for October, respectively.

7.5.5 Seasonal Variation per Energy Bin

The monthly variation pattern is also investigated per energy bin. Fig. 7.11 and 7.12 show the unfolded ratio per month in each energy bin and the corresponding predictions from MCEq. A clear variation pattern is observed from bin 3 onwards, corresponding to a neutrino energy above 302 GeV. However, the observed variation pattern differs from the symmetric variation amplitudes predicted by MCEq. Fig. 7.8 and 7.9 show that the unfolded ratios for February, September, October, and partly March do not agree with the expectation of MCEq. This is underlined by the χ^2-test, in which the hypothesis rejection of the quotient of the seasonal flux ratio to the prediction was discussed (refer to Appendix B.5.3). A pattern of a gradually decreasing variation strength from January to July is apparent, followed by a rapid increase in strength between August and October, ultimately reaching a constant maximum strength. This pattern is consistently observed up to bin 8, corresponding to an energies below 2 TeV. Due to lower statistics at higher energies, bins 9 and 10 exhibit larger statistical uncertainties. There is no distinct pattern in bin 10 for energies between 7 TeV to 10 TeV, as the ratio varies from month to month.

In summary, the expected variations from MCEq follow a symmetric pattern in each energy bin, governed by the atmospheric model NRLMSISE-00. However, an asymmetric increase/decrease in the monthly fluxes is observed in the unfolding.

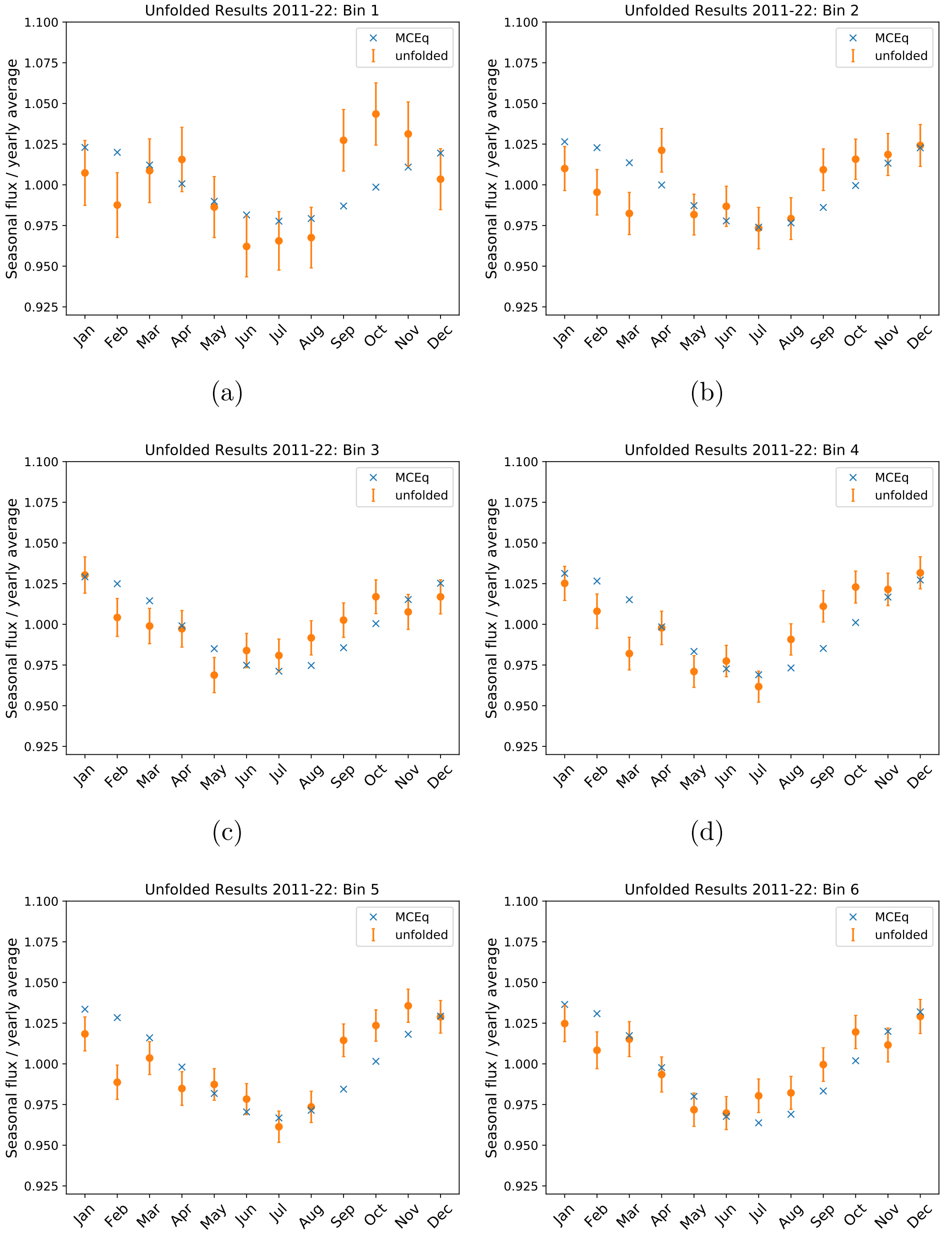

(a) (b)

(c) (d)

(e) (f)

Figure 7.11: Ratio of the monthly unfolded flux to the yearly average for each energy bin. The unfolded ratios are shown with error bars, and the MCEq predictions are shown in blue.

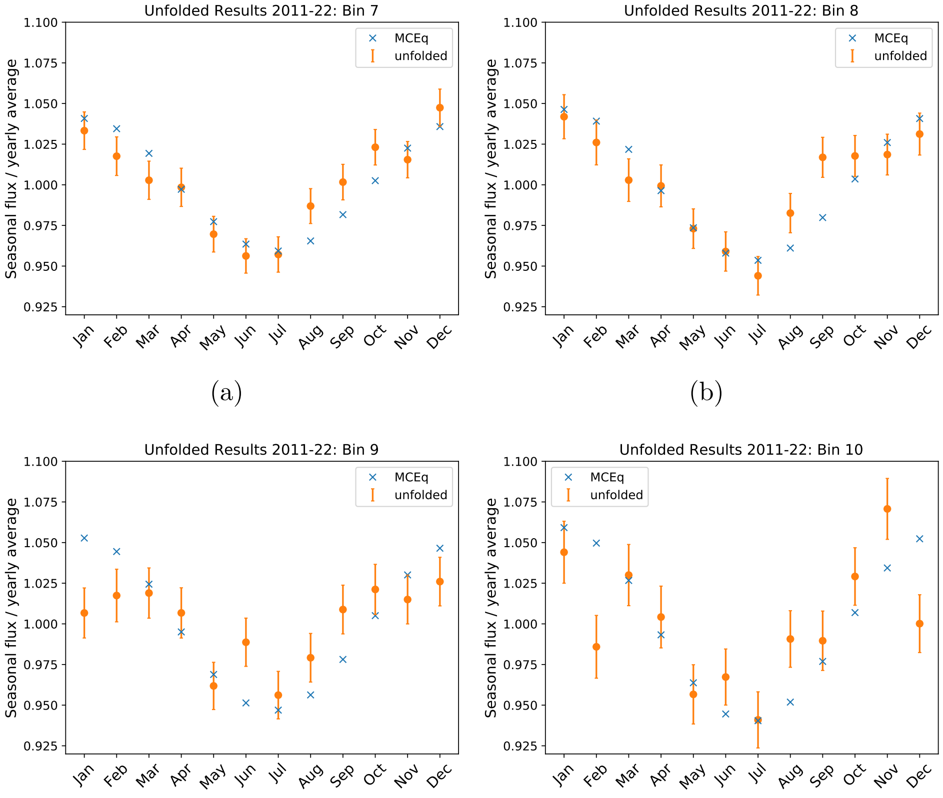

(a)

(b)

(c)

(d)

Figure 7.12: Ratio of the monthly unfolded flux to the yearly average for each energy bin. The unfolded ratios are shown with error bars, and the MCEq predictions are shown in blue.

7.5.6 Seasonal Change in Spectral Index

The shift in the spectral index of the seasonal flux is determined with respect to the annual average. The ratio of the seasonal flux to the annual average flux is expected to be one if no seasonal variations are observed. The ratio is fitted by the following power law,

$$f(\gamma) = \left(\frac{E}{1\,\mathrm{TeV}}\right)^{\Delta\gamma} . \tag{7.4}$$

$\Delta\gamma$ denotes the shift of the spectral index with respect to the annual mean. The fit accounts for the statistical uncertainties of the unfolded ratio. The resulting parameters are summarized in Table 7.2.

Season	p-value comp. MCEq	$\Delta\gamma$	Variation Significance / σ
January	1.49×10^{-1}	0.0039	4.6
February	1.75×10^{-6}	0.0053	0.7
March	1.08×10^{-2}	0.0086	0.8
April	8.83×10^{-1}	−0.0023	0.2
May	8.78×10^{-1}	−0.0045	5.3
June	3.75×10^{-1}	−0.0048	5.7
July	8.77×10^{-1}	−0.0080	8.5
August	2.04×10^{-2}	0.0006	2.4
September	3.14×10^{-6}	−0.0026	0.4
October	1.41×10^{-3}	−0.0000	3.7
November	4.38×10^{-1}	0.0032	4.4
December	2.48×10^{-1}	0.0030	5.6
June-August	4.39×10^{-2}	−0.0040	10.4
May-August	1.47×10^{-21}	0.0099	15.9
October-January	1.73×10^{-10}	0.0155	12.3
December-February	7.12×10^{-6}	0.0041	7.0
January-June	2.38×10^{-3}	0.0010	0.3
July-December	4.00×10^{-3}	−0.0008	0.2

Table 7.2: Summary of seasonal variations analysis showing the significance of the deviation of the unfolded seasonal spectrum to the annual average, the seasonal change in the spectral index. The p-values summarize the hypothesis test for the agreement of the unfolded seasonal flux with the MCEq prediction. The null hypothesis is rejected at a 3σ level for p-values below 0.003.

7.5.7 Summary

The investigation of the seasonal variations shows an asymmetric variation pattern compared to the predicted variations from MCEq. The calculated significance of the seasonal flux deviation to the annual average underlines an increase in the monthly flux from October to January, and a decreased flux from May to July/August with respect to the annual average. In particular, a similar ratio of the seasonal to annual mean flux is observed from October to January (cf. Fig. 7.11 and 7.12). In contrast, the decrease of the seasonal flux relative to the annual mean is maximal in July with 8.5σ. The deviation of the unfolded flux from the annual mean decreases continuously for the subsequent months. The monthly observed fluxes deviate from the annual mean flux by 5.7σ for June and 2.4σ for August. The χ^2-test shows that the unfolded ratio of seasonal to annual average flux is not compatible with the MCEq prediction for February, September, October, and the seasons December-February, January-June, May-August, and October-January. The mismatches between the prediction and the unfolded ratios underline the asymmetric seasonal variations. The analysis of monthly variations per energy bin shows a smooth decrease from January to July and a rapid increase from August to October. Therefore, the seasons are redefined as austral winter from May to August and austral summer from October to January based on the combination of months with a similar deviation to the annual average flux. The unfolded seasonal spectra are depicted in Fig. B.16 in the Appendix. In particular, the decrease in the variation strength for austral summer and winter above 4 TeV (refer to Fig. 7.6) is investigated further with respect to the zenith region in the next section.

	Energy Bin									
Season	1	2	3	4	5	6	7	8	9	10
January	0.7	1.0	3.0	2.5	1.8	2.5	3.3	4.2	0.7	4.4
±	2.0	1.4	1.1	1.0	1.0	1.1	1.2	1.4	1.5	1.9
February	−1.2	−0.5	0.4	0.8	−1.1	0.8	1.8	2.6	1.7	−1.4
±	2.0	1.4	1.2	1.1	1.1	1.1	1.2	1.4	1.6	1.9
March	0.9	−1.8	−0.1	−1.8	0.4	1.5	0.3	0.3	1.9	3.0
±	2.0	1.3	1.1	1.0	1.0	1.1	1.2	1.3	1.5	1.9
April	1.6	2.1	−0.3	−0.2	−1.5	−0.7	−0.2	−0.1	0.7	0.4
±	2.0	1.3	1.1	1.0	1.0	1.1	1.2	1.3	1.5	1.9
May	−1.4	−1.8	−3.1	−2.9	−1.3	−2.8	−3.0	−2.7	−3.8	−4.3
±	2.0	1.3	1.1	1.0	1.0	1.1	1.2	1.3	1.5	1.9
June	−3.8	−1.3	−1.6	−2.3	−2.2	−3.0	−4.4	−4.1	−1.1	−3.3
±	1.9	1.2	1.1	1.0	1.0	1.0	1.1	1.2	1.5	1.7
July	−3.4	−2.7	−1.9	−3.8	−3.9	−2.0	−4.3	−5.6	−4.4	−5.9
±	1.8	1.3	1.0	1.0	1.0	1.0	1.1	1.2	1.5	1.7
August	−3.2	−2.1	−0.8	−0.9	−2.6	−1.8	−1.3	−1.7	−2.1	−0.9
±	1.9	1.3	1.1	1.0	1.0	1.0	1.1	1.2	1.5	1.7
September	2.7	0.9	0.3	1.1	1.4	0.0	0.2	1.7	0.9	−1.0
±	1.9	1.3	1.1	1.0	1.0	1.0	1.1	1.2	1.5	1.8
October	4.4	1.6	1.7	2.3	2.4	2.0	2.3	1.8	2.1	2.9
±	1.9	1.2	1.0	1.0	1.0	1.0	1.1	1.3	1.5	1.8
November	3.1	1.9	0.8	2.1	3.6	1.2	1.5	1.9	1.5	7.1
±	2.0	1.3	1.1	1.0	1.0	1.0	1.1	1.3	1.5	1.9
December	0.3	2.4	1.7	3.2	2.9	2.9	4.7	3.1	2.6	0.0
±	1.9	1.3	1.1	1.0	1.0	1.0	1.1	1.3	1.5	1.8
Jun-Aug	−3.5	−2.0	−1.5	−2.3	−2.9	−2.2	−3.3	−3.8	−2.5	−3.4
±	1.1	0.8	0.6	0.6	0.6	0.6	0.6	0.8	0.9	1.1
Dec-Feb	0.0	1.1	1.7	2.2	1.3	2.1	3.4	3.3	1.7	1.0
±	1.2	0.8	0.7	0.6	0.6	0.7	0.7	0.8	1.0	1.2
May-Aug	−3.4	−3.3	−2.4	−6.0	−3.1	−3.1	−3.1	−1.0	−1.6	1.9
±	1.0	0.7	0.6	0.5	0.5	0.5	0.6	0.7	0.8	1.0
Oct-Jan	1.4	0.8	1.1	−1.3	1.8	3.3	1.3	4.7	5.7	6.7
±	1.1	0.7	0.6	0.5	0.5	0.6	0.6	0.7	0.9	1.1

Table 7.3: Unfolded seasonal variation strength per energy bin in percent.

8 Seasonal Variations in the Zenith Range from 90° to 110°

The disagreement between the ratio of the unfolded seasonal flux to the annual average and the MCEq predictions above 4 TeV is investigated further for the selected zenith region. The successive analysis of Ref. [1] of the correlation between temperature and seasonal rate variations from Ref. [72] restricted the maximum zenith angle to 110° because of only minimal temperature variations at higher zenith angles. Motivated by this adaptation, the seasonal temperature modulation is studied with respect to the zenith angle in the first section. The second section presents the determined seasonal variation strength in the restricted zenith range from 90° to 110°. The zenith angle was restricted after conducting the analysis results presented in the previous chapter. The investigation on rate and temperature variation with respect to the zenith angle was conducted as post-unblinding checks after approval of the analysis. The blinding policy and unblinding procedures are explained in Appendix B.4

Parts of this chapter are contained in conference proceedings of the author, in particular, Ref. [150, 127].

8.1 Zenith-dependence of Seasonal Variations

Seasonal variations of atmospheric lepton fluxes depend on the temperature variations, which differ with respect to the zenith angle. This effect is investigated firstly by temperature variations in different zenith bands. Secondly, the expected neutrino rate variation is calculated and compared to the measured data.

8.1.1 Temperature Variations

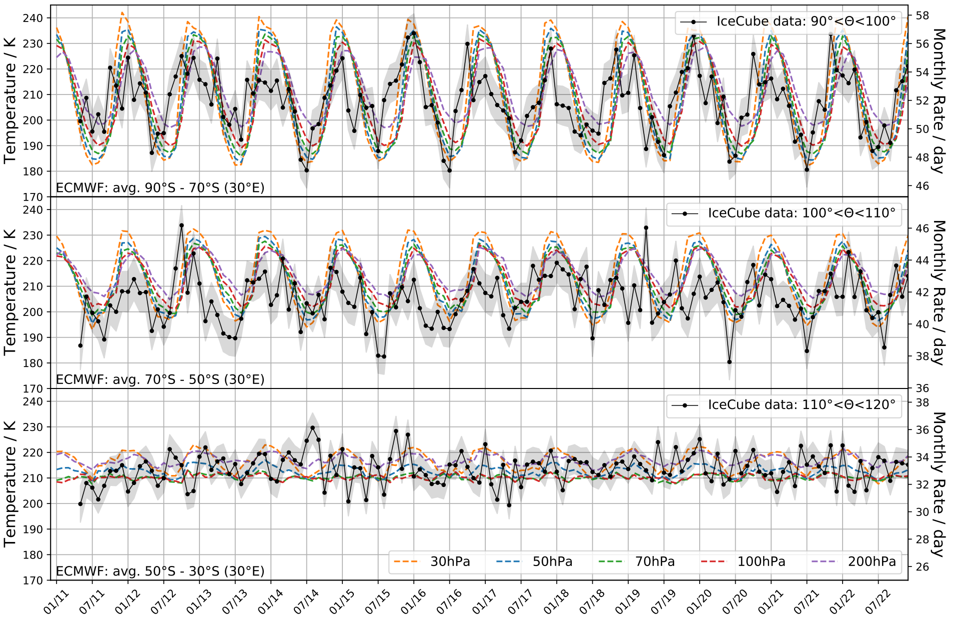

Figure 8.1: Phase comparison of selected ECMWF temperature profiles at different pressure levels relevant for neutrino production and measured monthly average neutrino rate in the zenith region from 90° to 120° by IceCube. Gray bands indicate the rate uncertainty determined by Gaussian errors. The averaged temperature profiles at stratospheric pressure levels between the minimum and maximum latitude of the respective band for a given longitude (30°E) are depicted as dashed lines. The temperature profiles are in phase with the corresponding neutrino rate up to a zenith angle of 110°. At higher zenith angles from 110° to 120°, the temperature profiles at 30 hPa to 50 hPa are in phase with the neutrino rate for all zenith bands, but an opposite phase is observed at 70 hPa to 100 hPa. The temperature profiles and neutrino rates are mostly flat and show no systematic variation.

The temperature modulation with respect to the zenith angle is investigated by stratospheric temperature data from the ERA-5 reanalysis dataset of the European Center for Medium-Range Weather Forecasts (ECMWF) [161] (see description in the Appendix D.1.4) from 2011 to 2022. Five exemplary temperature profiles at pressure levels from 30 hPa to 200 hPa relevant for neutrino production (cf. Ref. [67]) are overlaid with the average monthly measured neutrino rate for three zenith bands from 90° to 120° with equal width in zenith, shown in

Fig. 8.1. Lower atmospheric pressures correspond to higher altitudes and vice versa. The Gaussian uncertainty of the neutrino rate is depicted as gray bands. It can be observed that the temperature variations are larger at higher altitudes, where the pressure levels are lower. Higher energetic primaries interact at a higher altitude in the atmosphere so that the higher seasonal temperature modulation imprints a higher variation in the resulting lepton fluxes. Considering the variations from year to year, the temperature modulation at a given altitude remains constant throughout the years of interest.

The neutrino rate correlates well and the modulation is in phase with the temperature profiles at the displayed atmospheric pressure levels for zenith angles between 90° to 100°. The correlation decreases for the second zenith band between 100° to 110°, and the neutrino rate shows a smaller rate variation. No correlation between the modulation of the temperature profiles and the neutrino rate is observable for zenith angles from 110° to 120°. This indicates that the analyzed neutrino sample contains arrival directions from a stratospheric region that has no significant temperature change throughout the year. These events could affect the unfolded result as presented in Section 7.5, and potentially cause the variation strength to decrease at energies above 4 TeV due to the lack of sufficient temperature variation.

8.1.2 Relative Monthly Rate Variation

The predicted seasonal variation pattern is mainly attributed to the selected atmospheric model NRLMSISE-00 since the ratio of seasonal to annual average flux is not impacted by the primary composition or the hadronic interaction model in the energy range of interest (see Fig. B.4 and B.5). The current version of MCEq does not include temperature data as an input instead of an atmospheric model yet for the calculation of the spectrum. The other atmospheric models, such as the US Standard Atmosphere (see Appendix D.1.2), in MCEq do not consider seasonal variations monthly. Therefore, the predictions of seasonal energy spectra can currently only be calculated with the NRLMSISE-00 atmosphere.

However, a modified version of MCEq incorporating temperature data for the prediction of daily neutrino rates was developed in Ref. [1]. The observed seasonal variation in the neutrino rate is compared to the MCEq predictions using the NRLMSISE-00 atmosphere and the data-based approaches. A detailed description of the temperature data and atmospheric models in MCEq is given in Appendix D.1. Only the

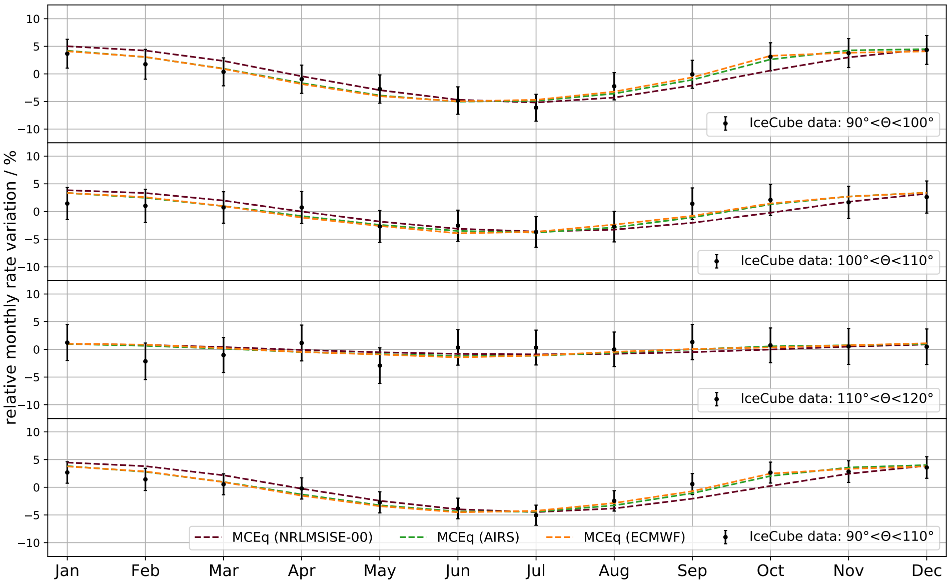

Figure 8.2: Relative average monthly neutrino rate modulation with respect to the annual average for the zenith ranges between 90° to 100°, 100° to 110°, 110° to 120°, and 90° to 110°, with statistical uncertainties. Dashed lines show the predicted variations from MCEq with the NRLMSISE-00 atmospheric model and temperature-based approaches using five years of temperature data from April 2012 to April 2017 from the AIRS instrument and one year of data from April 2012 to April 2013 from ECMWF.

expected rate, and not the resulting energy spectrum, can be calculated in the current modification of MCEq so far. As can be seen in Fig. 8.1, the temperature variation at a given altitude is mostly constant over the investigated years so that the calculated rates from Ref. [1] are usable for this investigation.

Fig. 8.2 depicts the monthly average rate variation with respect to the annual average for three distinct zenith bands in $\Delta\Theta = 10°$ width. The rate is overlaid with the calculated rate from MCEq with NRLMSISE-00, and temperature profiles as atmospheric model input from five years of AIRS data from April 2012 to April 2017 and one year of ECMWF data from April 2012 to April 2013. The relative monthly rate variation to the annual flux is averaged over the 11.5 years of data-taking. Statistical uncertainties are shown as error bars. The MCEq predictions from the different atmospheric assumptions are illustrated as dashed lines. Seasonal variations are observed in the upper panel for zenith angles between 90° to 100°. The maximum rate variation is observed in December with $(+5 \pm 2)\%$. The minimum is reached in July with a rate decrease of $(+6 \pm 2)\%$. The predicted rate variation differs between the calculation with NRLMSISE-00 and the data-based approaches. All predictions are in agreement between June/July and December/January, but the predicted rate with NRLMSISE-00 is approx. 1% to 2% larger in its amplitude. The variation strength increases rapidly from August to October, which is in agreement with the MCEq calculation based on AIRS and ECMWF data. The relative monthly variation strength decreases in the second panel for the zenith range of 100° to 110° with a maximum relative variation strength of approx. $(+2.5 \pm 2.5)\%$ in December and a minimum of $(-4 \pm 2.5)\%$ in July. The relative rate variation remains similar from September to March and decreases from April to August. The third panel shows the zenith region from 110° to 120°. No variation is measured or predicted in this range, as the monthly relative rate variation fluctuates around 0%. Therefore, the zenith range is reduced to angles from 90° to 110°. The observed and predicted variations for the adapted region are depicted in the lowest panel.

In summary, the comparison of the neutrino rate calculations from different atmospheric assumptions shows a deviation of the data-based calculations to NRLMSISE-00. The minimum and maximum variation strength and time of year are the same for all approaches. NRLMSISE-00 predicts a symmetric modulation throughout the year, while the data shows an asymmetric pattern. The decrease in variation strength from January to July is smooth and linear every month, which is why the predictions differ during this period, as discussed in Chapter 7. The discrepancy even increases between August and October due to the rapid increase in variation strength caused by sunrise in the Southern Hemisphere. The calculated average rate variation is similar for the calculation with AIRS and ECMWF data. The deviation of both calculations from NRLMSISE-00 is shown in the Appendix in Fig. D.1.

8.1.3 Comparison of the Zenith Regions

The seasonal variations are further analyzed on the modified zenith range between 90° to 110°, excluding zenith angles larger than 110°. The two zenith bands and the corresponding average seasonal rate variation per month are displayed in Fig. 8.3. The relative monthly rate

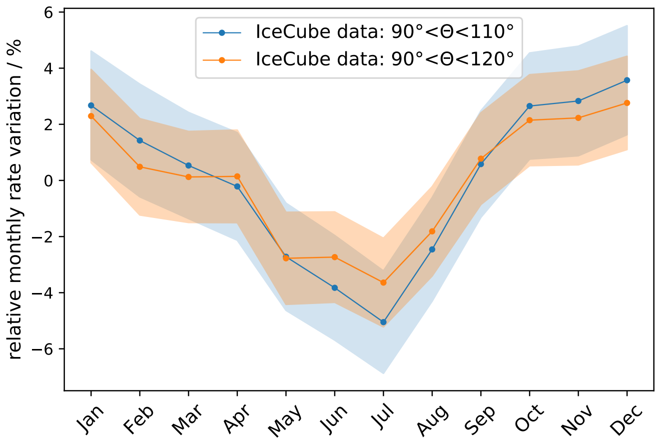

Figure 8.3: Relative average neutrino rate per month for the zenith ranges from 90° to 120° and 90° to 110°. The bands denote statistical uncertainties of the measured rate.

variations are approx. 1% to 2% larger for the restricted zenith range from 90° to 110°.

The seasons for the second analyzed dataset for zenith angles between 90° to 110° are constructed based on months with similar observed average neutrino rates. The relative rate comparison shows a maximum rate variation from October to January and a minimum from May to August. Restricting the zenith range to a maximum angle of 110° results in a loss of only about 26% of the events (refer to Fig. 5.5). However, the loss is compensated by defining austral summer and winter as a combination of four months instead of three.

8.2 Expected Results

Before the unfolded seasonal spectra can be investigated for the restricted zenith range from 90° to 110°, it needs to be ensured that DSEA+ can unfold the restricted dataset without being retrained to the adapted range. Pseudo samples are generated for the restricted energy range and weighted to the seasonal MCEq predictions and unfolded, as it was done in Section 7.4.1. The size of the samples is set to match the expected number of events within the restricted zenith range for each season in the dataset. However, systematic uncertainties need to the recalculated for the restricted range, as explained in Section 7.2.

The impact of each source of uncertainty on the unfolded spectrum is depicted in the Appendix in Fig. C.1.

8.2.1 Unfolding of Pseudo Samples

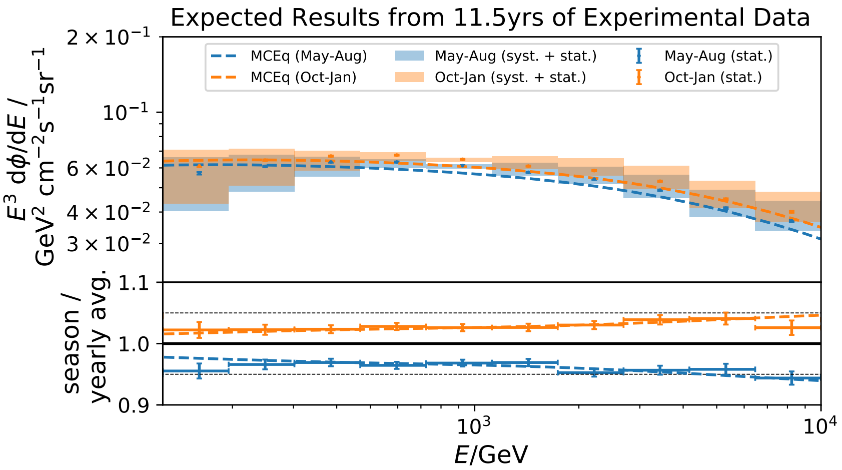

Figure 8.4: Unfolded seasonal spectra and unfolded ratio of seasonal to annual average flux from pseudo samples weighted to the seasonal MCEq predictions for 11.5 years of data-taking. Error bars depict statistical uncertainties while colored bands depict systematic ones. The predicted flux from MCEq is scaled up by a fitted normalization constant for the unfolded spectrum. The lower panel displays the ratio of the seasonal to annual average flux for the unfolded data and the MCEq-calculated theory fluxes. Black dashed lines illustrate ±5% deviation from the annual average flux. Since the systematic uncertainties remain the same for each season and cancel out in the ratio, the statistical uncertainties are the only uncertainties in the ratio.

The unfolded spectra for both pseudo samples from May to August and October to January are depicted in the upper panel in Fig. 8.4 in comparison to the MCEq predictions. The unfolded spectra are consistent with the predicted fluxes from MCEq concerning the corresponding uncertainties. The lower panel shows the unfolded ratio of the seasonal to annual average flux with respect to the statistical uncertainty. Prediction and unfolded pseudo-data are in agreement for both seasons. Whether DSEA+ needs to be retrained on the restricted range is investigated in the next section.

8.2.2 χ^2-Test

The same χ^2-test is performed as in Chapter 7.4.2 to investigate the compatibility of the unfolded ratio of seasonal to annual average flux to the MC truth. As discussed previously, the test calculates the quotient of the unfolded ratio and the prediction. The null hypothesis is defined as a quotient of 1 when both the unfolding and the prediction are compatible with respect to statistical uncertainties in the unfolded ratio. The hypothesis is rejected for p-values ≤ 0.003.

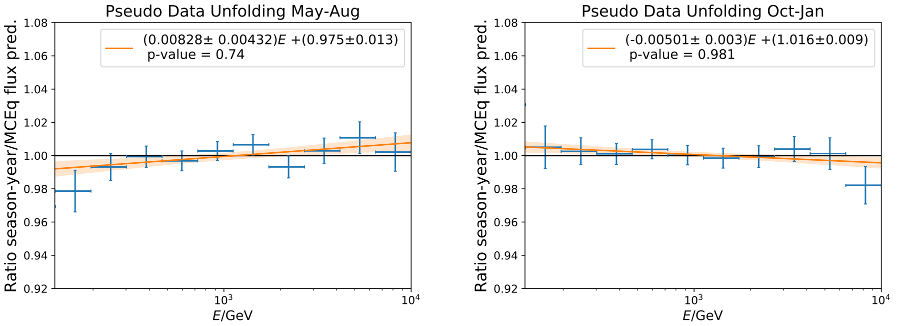

(a) (b)

Figure 8.5: χ^2-test to determine the accuracy of the unfolded seasonal to annual average in zenith range from 90° to 110°. The target of the test is the quotient of the unfolded seasonal flux ratio to the prediction for each energy bin. The null hypothesis that should be rejected is defined as a quotient of one. This implies that the unfolded ratio is in agreement with the prediction, ensuring the feasibility of seasonal unfolding. The null hypothesis cannot be rejected for both seasons, which indicates that the unfolded ratio is in agreement with the prediction.

Fig. 8.7 depicts the test results for austral summer and winter. The null hypothesis cannot be rejected with $p = 0.740$ from May to August and $p = 0.981$ from October to January. To conclude, no retraining of DSEA+ is required since the ratio can be determined at the required precision. The robustness against changes in spectral index is tested in Appendix C.2.1.

8.3 Measurement of Seasonal Variations

This section discusses the unfolded seasonal spectra and variation strengths for the zenith range from 90° to 110°. The deviation of the seasonal unfolded flux to the annual average is quantified in a χ^2-test, and the compatibility of the unfolded ratio to the MCEq predictions is investigated in a second χ^2-test, as in Chapter 7.5.

8.3.1 Summer-Winter Split

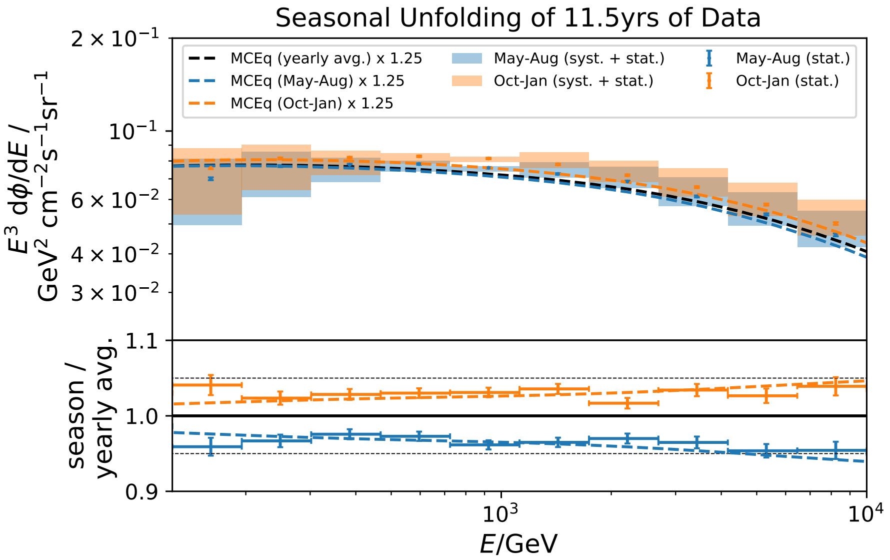

Figure 8.6: Unfolded seasonal muon neutrino spectra for austral summer and winter for the zenith range from 90° to 110°. Error bars depict statistical uncertainties while colored bands depict systematic ones. The predicted flux from MCEq is scaled up by a fitted normalization constant for the unfolded spectrum. The lower panel displays the ratio of the seasonal to annual average flux for the unfolded data and the MCEq-calculated theory fluxes. Black dashed lines illustrate ±5% deviation from the annual average flux. Since the systematic uncertainties remain the same for each season and cancel out in the ratio, the statistical uncertainties are the only uncertainties in the ratio.

The unfolded seasonal spectra for the restricted zenith region are shown in Fig. 8.6 for austral summer, defined as October to January, and austral winter, defined as May to August. The unfolded spectra are consistent with the scaled MCEq fluxes with the same fitted normalization factor as in Fig. 7.6. Except for threshold effects in the first bin, the unfolded ratios of the seasonal to annual mean flux increase with energy from $(+2.3 \pm 0.9)\%$ at 194 GeV to $(+3.9 \pm 1.2)\%$ above 7 TeV for October to January, and decrease up to $(-4.6 \pm 1.1)\%$ for May to August. The unfolded seasonal fluxes that deviate from the annual average are obtained by 10.6σ in austral summer from October to January, and 13.2σ for austral winter from May to August. The determined variation strength is depicted in Table 8.1.

8.3.2 Agreement to MCEq

As for the entire zenith range, the agreement between the ratio of the unfolded seasonal to annual average flux and the MCEq predictions is examined in a χ^2-test (as explained in Chapter 7.5.4). The test investigates the quotient of the unfolded seasonal to annual average flux and the prediction from MCEq. The null hypothesis is defined as a quotient of 1 with a rejection at 3σ significance level, corresponding to a p-value < 0.003. With p-values of $p = 5.31 \times 10^{-1}$ for the May-August season and $p = 1.73 \times 10^{-1}$ for the October-January season, the null hypothesis cannot be rejected for either season. The quotient is compatible with one with respect to the uncertainties, as depicted in Fig. 8.7. The results, as well as the fit of spectral index change (see Chapter 7.5.6) are summarized in Table 8.2.

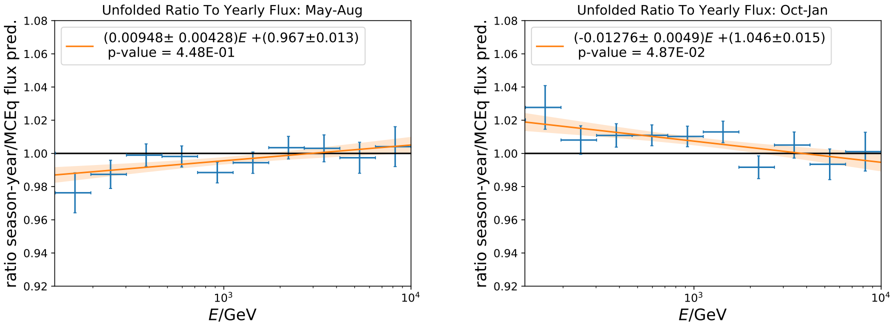

(a) (b)

Figure 8.7: χ^2-test to determine the deviation of the unfolded seasonal flux ratios to the predicted ratio by MCEq. The error bars depict statistical uncertainties in the ratio from the unfolding. The null hypothesis that should be rejected is defined as a quotient of the seasonal flux ratio to the prediction of one. This implies that the unfolded ratio is in agreement with the prediction. The p-value for each season is given in the caption. The ratio of the unfolded results to the MCEq prediction is fitted by a linear function to show potential offsets to the prediction.

	Energy Bin									
Season	1	2	3	4	5	6	7	8	9	10
May-Aug	−4.1	−3.3	−2.4	−2.7	−3.8	−3.5	−3.0	−3.5	−4.6	−4.6
±	1.2	0.8	0.7	0.6	0.6	0.6	0.7	0.8	0.9	1.1
Oct-Jan	4.1	2.3	2.8	3.0	3.1	3.6	1.7	3.4	2.7	3.9
±	1.3	0.9	0.7	0.6	0.6	0.7	0.7	0.8	1.0	1.2

Table 8.1: Unfolded seasonal variation strength per energy bin in percent for the restricted zenith range from 90° to 110°.

Season	p-value	$\Delta\gamma$	Variation Significance / σ
May-August	5.31×10^{-1}	-0.0034	13.2
October-January	1.73×10^{-1}	0.0001	10.6

Table 8.2: Summary of the seasonal variation analysis including the significance of the deviation of the unfolded seasonal spectrum to the annual average, and the seasonal change in spectral index. The p-values summarize the hypothesis test of the agreement of the unfolded ratio of seasonal to annual average flux. The null hypothesis is rejected for at a 3σ level for p-values below 0.003.

9 Conclusion

In the subsequent sections, the main findings of this dissertation are summarized and an outlook on future prospects is presented.

Summary

The study of seasonal variations of neutrinos from atmospheric particle cascades provides insights into hadronic particle interactions and atmospheric temperature modulation. Atmospheric neutrinos form a dominant background in the search for astrophysical neutrinos, and understanding the seasonal modulation of the atmospheric neutrino flux is crucial for accurate modeling of the detector background.

For the first time, seasonal energy spectra for atmospheric muon neutrinos were determined for the energy range from 125 GeV to 10 TeV. One of the main goals of this dissertation project was the development of an analysis pipeline for the energy-dependent measurement of seasonal variations. The second target was the hypothesis test of whether the seasonal variation strength increases with energy, which could not be measured previously due to insufficient statistics from neutrino telescopes at hand. In summary, the collected up-going muon neutrino events in IceCube from May 2011 to December 2022 were grouped into seasons, and energy spectra were unfolded with the Dortmund Spectrum Estimation Algorithm (DSEA+). In this dissertation, DSEA+ was applied for the first time in a complete data analysis pipeline in astroparticle physics. This work exploited the seasonal independence of systematic uncertainties on the unfolded spectra, which enabled a measurement of the seasonal variation strength at percentage precision. The variation strength was defined as the ratio of seasonal to annual average flux so that systematic uncertainties cancel in the ratio and it is only affected by statistical uncertainties. The variation strength was analyzed within two zenith ranges from 90° to 120° and 90° to 110° motivated by the deeper investigation of temperature modulation and neutrino rate dependent on the zenith direction.

Zenith Range from 90° to 120°

- The unfolding of the austral summer and winter shows a deviation of the seasonal to the annual average flux with a significance of 7.0σ for December to February and 10.4σ from June to August.

- The analysis of the monthly variation shows an asymmetric variation pattern across the months. The maximum amplitude of the seasonal variation strength to the annual mean is observed in July with 8.5σ, while the significance is lower with 5.3σ in May and 5.7σ in June. The significance of the increased flux is maximal in December with 5.6σ. The neutrino flux decreases smoothly from January to July, then increases rapidly until October, when the maximum flux is reached.

- The compatibility of the measured variation strength and the prediction from MCEq based on the atmospheric model NRLMSISE-00 was investigated in a χ^2-test. The hypothesis that the unfolded variations are compatible with the MCEq predictions was rejected at the 3σ level for the months of February, September, and October, and for the seasons of May-August, October-January, December-February, and January-June. Despite the expectation, the variation strength decreases above 4 TeV for the seasons June-August and December-February.

- The redefinition of the seasons based on months with similar rate and temperature variations reflects the asymmetric variation and results in an increase of the significance for the deviation from the annual average neutrino flux to 12.3σ for October to January but decreases to 15.9σ for May to August.

Reinvestigation of the Zenith Range from 90° to 110°

- The lack of sufficient temperature and measured rate variation for neutrinos from zenith angles between 110° to 120° motivated to reanalyze the seasonal variations only in the range of 90° to 110°. The new event selection includes 26% fewer events, but the redefinition of austral summer and winter ensures the same measurement accuracy for the entire zenith range.

- Seasonal deviations from the annual average were measured at 10.6σ for the season from October to January, and 13.2σ from

May to August. Monthly unfolding was not feasible with the available statistics.

- The unfolded seasonal variation strength is compatible with the MCEq prediction over the entire energy range from 125 GeV to 10 TeV and the null hypothesis could not be rejected.

Future Prospects

The analysis at hand presented an unfolding method to determine seasonal variations in the neutrino energy spectrum at a percentage level. So far, the variations can only be studied up to a maximum energy of 10 TeV due to the limited statistics in the event samples of atmospheric neutrinos in IceCube. The neutrino rate falls steeply according to a power law, and it is extremely difficult to distinguish between neutrinos of atmospheric and astrophysical origin in the TeV regime. The energy range beyond 10 TeV opens an interesting region, because the uncertainty of the atmospheric neutrino flux is largely due to the different hadronic interaction models. Thus, seasonal variations provide a unique way to test hadronic interactions in atmospheric particle cascades. Extending the analysis to energies around 100 TeV could constrain hadronic interaction models on energy scales beyond the reach of particle accelerators.
Furthermore, the measurement of seasonal variations could provide an indicator for the existence of a prompt component in the atmospheric neutrino flux. Prompt neutrinos are not expected to show seasonal flux variations due to the short lifetime of their parent particles. A decrease in the variation strength with respect to the predicted variations of the conventional component only could constrain the existence of prompt neutrinos.

In this thesis, the obtained seasonal variations for each season were compared with the MCEq prediction from the atmospheric model NRLMSISE-00. Although a good agreement is found for the zenith region from 90° to 110°, the predictions could be compared with the flux calculated from temperature data. MCEq would have to be modified to read temperature data instead of an atmospheric model.

Another follow-up analysis could be the measurement of the K/π-ratio in atmospheric air showers. The production of neutrinos and muons is governed by these two parent mesons, and their contribution to the rate variation can be counted and compared with the determined correlation coefficient between rate variation and temperature. The K/π-ratio has large uncertainties in previous measurements from colliders, and seasonal variations mark a way to obtain this quantity, as explained in Ref. [68, 162].

The analysis developed in this thesis can also be applied to atmospheric muons. The majority of detected particles are atmospheric muons from air showers, orders of magnitude more than atmospheric neutrinos. These muons represent an immense background for the search for astrophysical neutrinos in the down-going region. An accurate measurement of the seasonal variations would improve the background modeling. Moreover, the combination of seasonal variations of muons and neutrinos could further constrain hadronic interaction models, since muons do not come from cosmic objects, so they are purely atmospheric in origin.

A Simulation Sets

Number	Energy Range / GeV	Spectral Index γ	Syst. Parameter
21002	10^2 to 10^8	-2.0	ref. abs. and ref. hole ice & DOM eff.
21047	10^2 to 10^8	-2.0	
21003	10^2 to 10^8	-2.0	scat $+5\%$
21004	10^2 to 10^8	-2.0	scat -5%
21005	10^2 to 10^8	-2.0	abs $+5\%$
21006	10^2 to 10^8	-2.0	abs -5%
21047	10^2 to 10^8	-2.0	$\epsilon_{\mathrm{DOM}} + 10\%$
21047	10^2 to 10^8	-2.0	$\epsilon_{\mathrm{DOM}} + 10\%$
21047	10^2 to 10^8	-2.0	$p_0 + 1$
21047	10^2 to 10^8	-2.0	$p_0 - 1$

Table A.1: Simulation sets and corresponding systematic parameter variation.

B Unfolding of the Zenith Range from 90° to 120°

B.1 Dataset

Season	Number of Events	Livetime / days
January	41815	322.8
February	37809	297.2
March	41939	330.8
April	40605	320.3
May	42927	348.4
June	43796	355.7
July	44681	366.3
August	45782	368.3
September	45727	358.3
October	47670	368.6
November	44938	347.1
December	46027	353.8
June-August	134259	1090.2
December-February	125651	973.8
full year	523736	4137.5

Table B.1: Number of events and livetime per season within the zenith range from 90° to 120° from May 2011 to December 2022.

B.2 Size of the Training Sample

As described in Chapter 7.3, the size of the training sample is set to 100 000 events. This number is found to be sufficient to obtain an accurate unfolded spectrum with the event selection at hand. The impact of the size of the training sample is investigated by unfolding the same pseudo sample with DSEA+ trained on the same sample with varied sizes. The pseudo sample to be unfolded is generated by weighting

100 000 events of the MC sample to the annual average atmospheric and astrophysical flux (see description in Chapter 5.3.1). DSEA+ is then trained on events weighted by the same models, but the size of the training sample is varied between 100 000, 200 000, and 1 000 000 (referred to as *extended* training sample). The unfolded spectra obtained with DSEA+ trained on an event sample of different sizes are shown in Fig. B.1. The upper panel depicts the unfolded normalized number of events, which is the target quantity returned by DSEA+ averaged over 2000 bootstrap pulls. The statistical uncertainties in the shaded bands are too small to be visible in this representation. The lower panel depicts the ratio of the estimated normalized number of events to the true distribution. The dashed lines indicate a ±5% deviation from the MC truth. The unfolded spectrum from DSEA+ trained on 100 000 events is consistent with the true distribution. When the size of the training sample is further increased, the deviations from the truth increase.

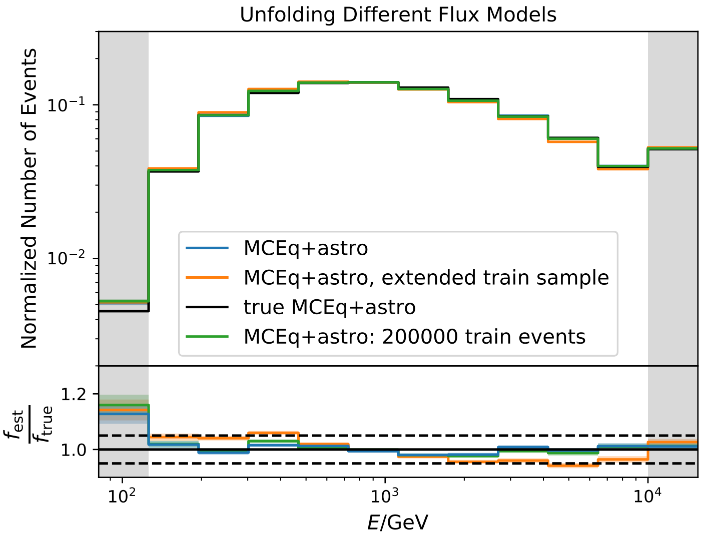

Figure B.1: Unfolded pseudo sample of the annual average atmospheric and astrophysical flux by DSEA+ trained on MC with varied training sample size. The blue distribution is obtained by DSEA+ trained on 100 000 events, green by DSEA+ trained on 200 000 events, and orange by DSEA+ trained on 1 000 000 events. Under- and overflow bins are marked as the shaded areas.

B.3 Robustness of DSEA+ to a Prior

The subsequent test examines the robustness of DSEA+ to a fixed prior (see description in Chapter 6.2). The unfolding algorithm is given a uniform prior as an argument. This is an assumption which DSEA+ makes as default for the first iteration. The chosen prior is far from the target distribution and the algorithm should ideally be independent of the selected input prior. The impact of the prior is investigated by the WD, which is calculated between the true and the estimated event spectrum in each iteration of DSEA+. A pseudo sample of 100 000 events weighted by the annual average of the atmospheric flux prediction from MCEq and astrophysical flux (see description in Chapter 5.3.1), which is the same weighting as for the training sample, is unfolded in 2000 bootstrap pulls. The WD distributions for iterations 1 to 6 are depicted in Fig. B.2. The WD of the first iteration is strongly influenced by the uniform prior because the RF predictions are weighted to the prior. Starting from the second iteration, the influence of the prior disappears because the prior is updated by the previous estimate of the first iteration of DSEA+. The WD remains unchanged for subsequent iterations as the algorithm converges. This test validates that four iterations are sufficient to unfold the neutrino spectrum from the event selection at hand.

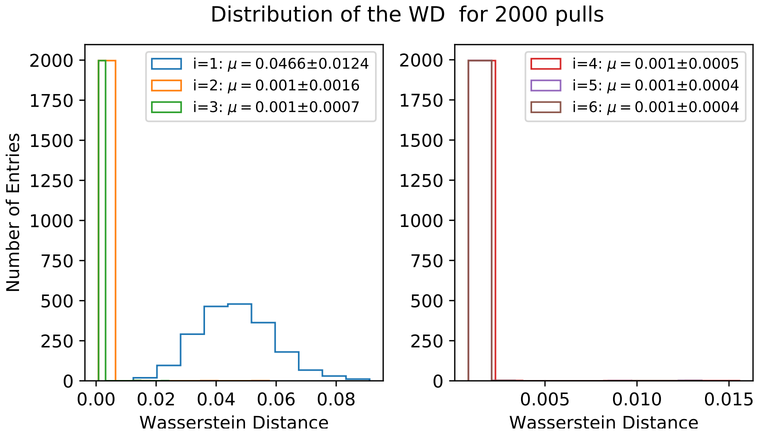

Figure B.2: Impact of uniform prior on the convergence of DSEA+. The WD distributions are shown for 2000 bootstrap pulls in dependence of DSEA+ iterations.

B.4 Burnsample Tests

Data analyses in IceCube are subject to blind analysis policies. The analysis pipeline in this dissertation has been exclusively developed using simulated data weighted by the respective expected physical flux model of the data. Before accessing the entire dataset, proof-of-concept tests are usually performed on a small dataset referred to as *burnsample*. During the development stage of this analysis, the burnsample was defined as 10% of the available data under full detector configuration. The purpose of a burnsample is to impartially evaluate the analysis without influencing potential outcomes. For this particular analysis, the burnsample consists of 10% of data collected between 2011 and 2020, corresponding to approximately one year of effective livetime. Constructing a burnsample from 10% of all available data from 2011 to 2022 (all detector runs ending with 0) would violate the purpose of a burnsample since it would comprise more than one year of effective lifetime. The sample is only generated to test the analysis pipeline and should not resolve any physical results. The entire dataset can be utilized after a collaboration-internal review process.

B.4.1 Unfolding of Seasonal Spectra

The unfolded burnsample sets for austral summer (December to February) and austral winter (June to August) are depicted in Fig. B.3. The upper panel displays the unfolded seasonal spectra, indicating systematic uncertainties through shaded areas. Statistical uncertainties are represented by error bars, which are greater than those for the entire dataset. The unfolded spectrum has a higher normalization compared to the calculated spectrum from MCEq, which is consistent with other measurements [131]. Chapter 5.5 discusses the difference in normalization between theory and measurement. The unfolded spectra agree in shape with the MCEq prediction. As described in Chapter 7.3, the lower panel depicts the ratio of seasonal to annual average flux, which is independent of systematic uncertainties on the spectrum unfolding. The statistical uncertainties on the ratio are relatively large due to the small statistics in the burnsample. The obtained flux ratios are largely consistent with MCEq and show increasing seasonal variations with energy, except for the second and last energy bin for the December-February season. The ratio in both bins aligns with the annual average.

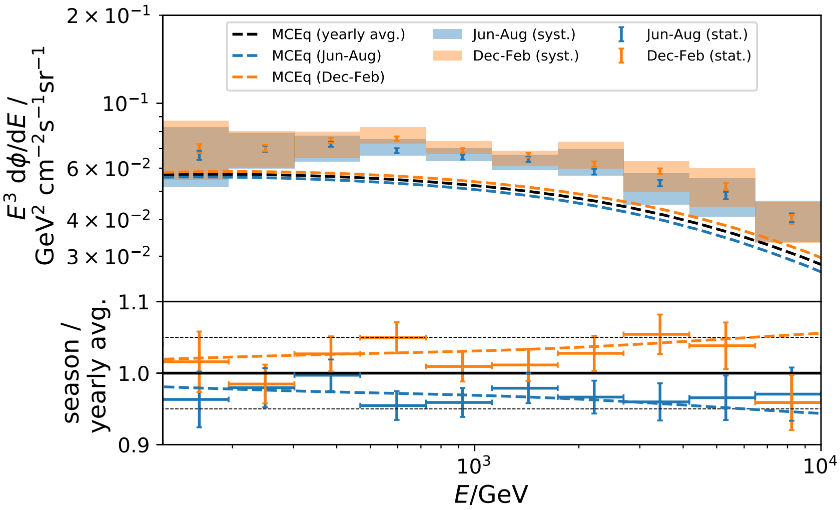

Figure B.3: Seasonal unfolding of the burnsample comprised 10% of the measured data between 2011 to 2020. Error bars depict statistical uncertainties while colored bands depict systematic ones. The predicted flux from MCEq is scaled up by a fitted normalization constant for the unfolded spectrum. The lower panel displays the ratio of the seasonal to annual average flux for the unfolded data and the MCEq-calculated theory fluxes. Black dashed lines illustrate ±5% deviation from the annual average flux. Since the systematic uncertainties remain the same for each season and cancel out in the ratio, the statistical uncertainties are the only uncertainties in the ratio.

B.4.2 Impact of Selected Models in MCEq

The impact of the selection of the primary CR composition and the hadronic interaction model in MCEq is studied for the seasonal burnsample unfolding from December to February. To investigate the impact of one specific model assumption, one of either the composition or hadronic interaction model is held constant, whereas the remaining ones are iterated over four different models. Fig. B.4 and B.5 show the unfolded and calculated (dashed lines) spectra for the austral summer in the upper panel, and the ratio to the annual mean in the lower panel. As can be seen in Fig. B.4, the spectral shape is largely determined by the primary composition model. The calculation shows different primary models show a change in normalization, and the deviations between the calculated spectra increases with energy. The calculated spectra with H3a and H4a show a slower decline with increasing energy than those with GST and PG. PG yields a lower normalization, as it is

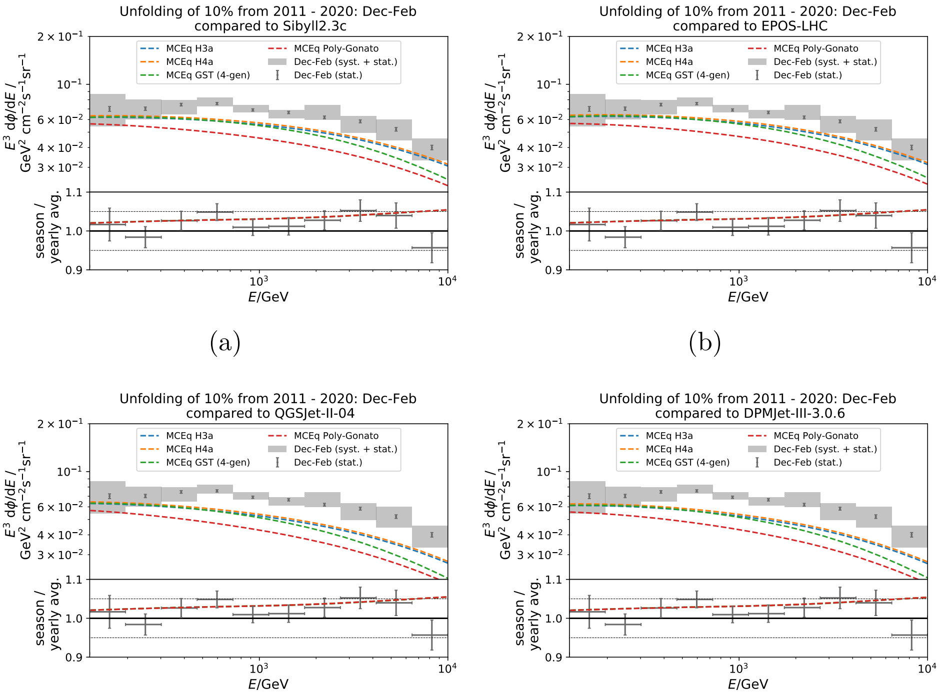

(a) (b)

(c) (d)

Figure B.4: *Top*: Unfolded seasonal burnsample for 10% of the data from December to February from 2011-2020 in comparison to the MCEq predictions with a variation of the primary CR composition model. *Bottom*: Ratio of seasonal to annual average flux.

derived from CR-data around the knee region only. Other primary energies are interpolated and PG might not accurately describe the spectrum outside of the knee region. As shown in Fig. B.5, the selection of the hadronic interaction model determines the slope of the calculated spectra, but all have the same normalization at 125 GeV. The deviations between the models increase with energy. Although the selection of the respective models leads to large differences in normalization and spectral index, the ratio of seasonal to annual average flux shows no visible changes in the energy range of interest. Therefore, comparing the unfolded ratio to the MCEq prediction of one specific model combination is sufficient. This test indicates that the predicted seasonal variation pattern in the energy range between 125 GeV to 10 TeV depends on the atmospheric model in MCEq. However, it is not possible to test changes in the atmosphere since NRLMSISE-00 is the only model that

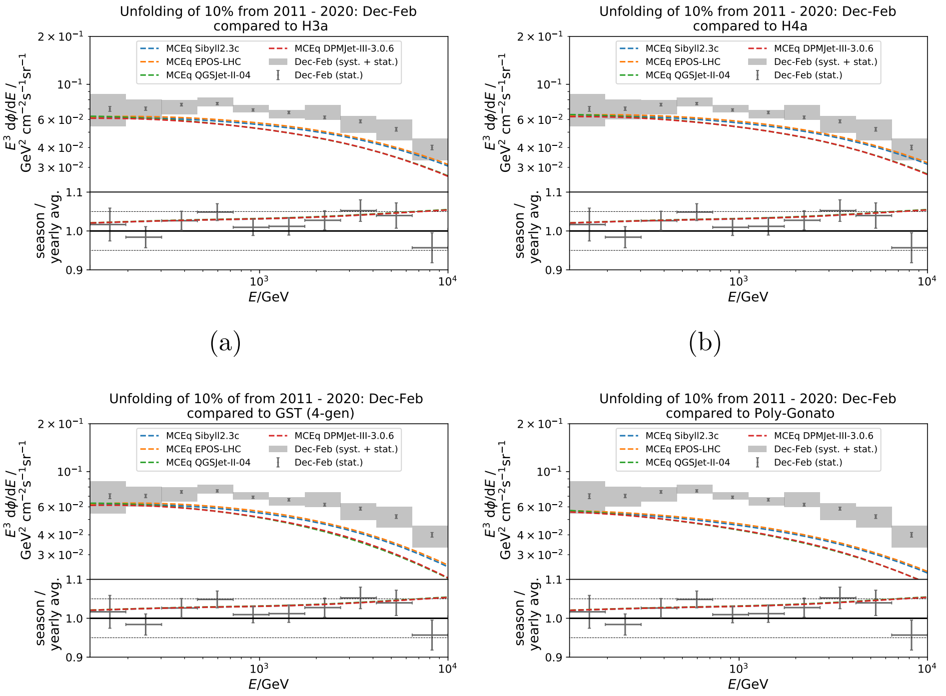

(a) (b) (c) (d)

Figure B.5: *Top*: Unfolded seasonal burnsample for 10% of the data from December to February from 2011-2020 in comparison to the MCEq predictions with variation of the hadronic interaction model. *Bottom*: Ratio of seasonal to annual average flux.

considers monthly temperature variations (refer to Appendix D.1 for descriptions).

B.4.3 Investigation of Systematic Parameters

This section provides a thorough analysis of the individual systematic parameters and their influence on the unfolded spectrum relative to the unfolded reference pseudo sample. The parameters are described in detail in Chapter 7.2. This test was conducted as a part of the blindness tests on the burnsample as well, before the analysis chain was applied to the complete dataset. The pseudo sample is weighted by the seasonal MCEq flux prediction for austral winter from June to August. The statistics in this seasonal test sample are comparable to one month of data within the entire data-taking period. The determined systematic uncertainties remain the same for all seasons, while

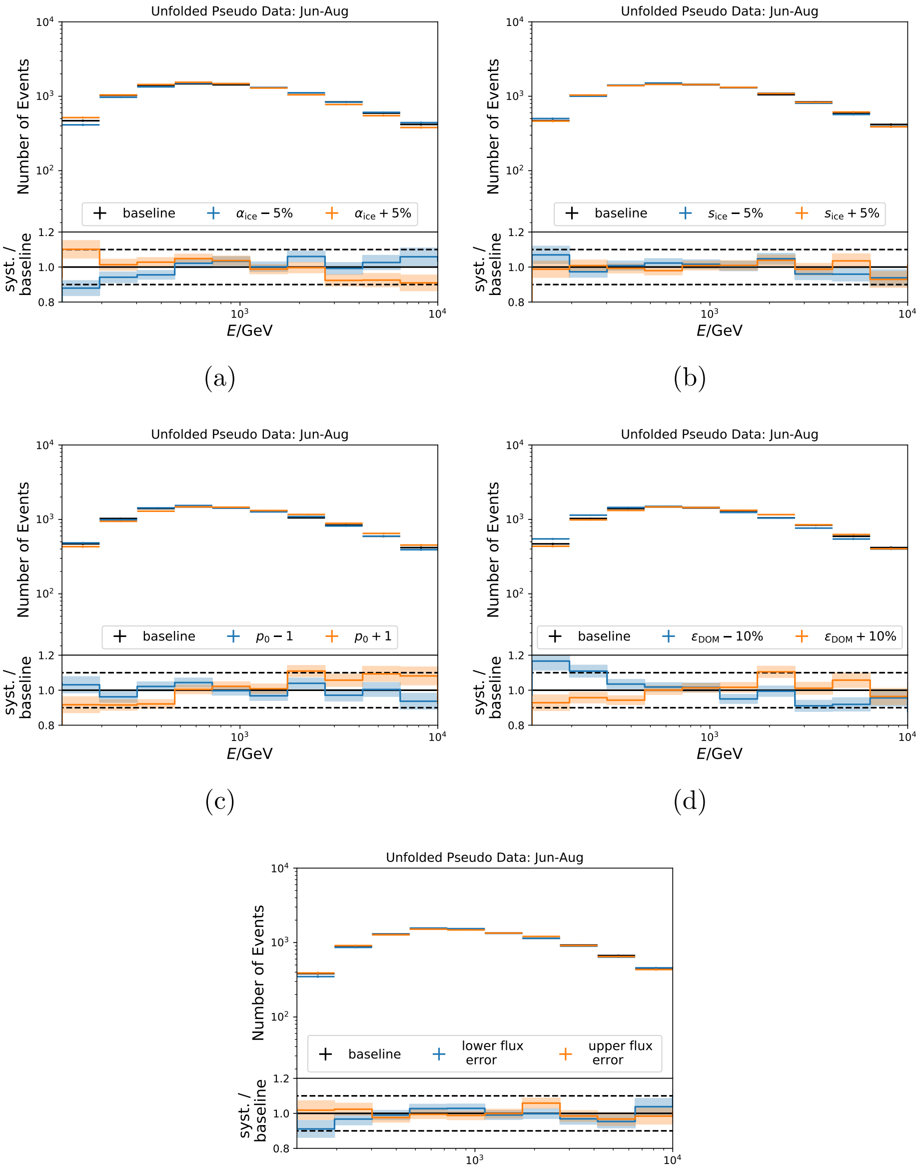

(a) (b)

(c) (d)

(e)

Figure B.6: Unfolded event spectra for the systematic and the reference pseudo samples. The number of events is set to 10% of the expected events for June to August between 2011 to 2020, as a burn-sample test. The statistical uncertainties in the ratio are illustrated as shaded bands.

the number of events in the pseudo sample is adjusted to provide a realistic statistical uncertainty. The unfolded event spectra obtained from a variation of a systematic parameter to the reference are depicted in the upper panel in Fig. B.6. The deviation of the event spectra to the unfolding of the baseline pseudo sample is shown in the lower panel concerning statistical uncertainties highlighted by shaded bands. Whereas scattering in ice and flux model uncertainties on the weighting have a similar impact over the entire energy range, changes in the DOM efficiency and absorption in ice are energy-dependent. In particular, the unfolded number of events differs up to approx. 18% to the unfolded reference pseudo sample in bins with lower statistics at the edges of the displayed energy range. The decrease of the hole ice parameter p_0 has almost no impact on the spectrum unfolding. However, the increase yields an energy dependence.

B.5 χ^2-Tests

χ^2-tests are used in this dissertation to quantify various objectives. The feasibility of seasonal unfolding on pseudo samples is examined in the first section. The second part tests for the ability of seasonal unfolding concerning a change in the spectral index compared to the seasonal predictions from MCEq. The third test investigates the compatibility of the unfolded seasonal variation strength from data with the MCEq prediction.

B.5.1 Feasibility of Seasonal Unfolding

A χ^2-test is performed to investigate how precisely the seasonal variation strength defined the flux ratio of a specific season to the annual average can be unfolded, as described in Chapter 7.4.2. The deviation is defined by the quotient of the ratio of the unfolded seasonal to annual average flux to the prediction from MCEq. The null hypothesis is defined as a quotient of 1, which indicates that the prediction and unfolded ratios are in agreement. The hypothesis is to be rejected at a 3σ-level the p-values smaller than ≤ 0.003.
The test results are depicted for every season in Fig. B.7 to B.10. The error bars represent the quotient of the unfolded ratio to the MCEq prediction in terms of statistical uncertainties. The corresponding p-values and linear fits are shown for each season. The ratio obtained fluctuates around 1, and the null hypothesis cannot be rejected for any

season. This study indicates that it is feasible to unfold the monthly data from 11.5 years of data.

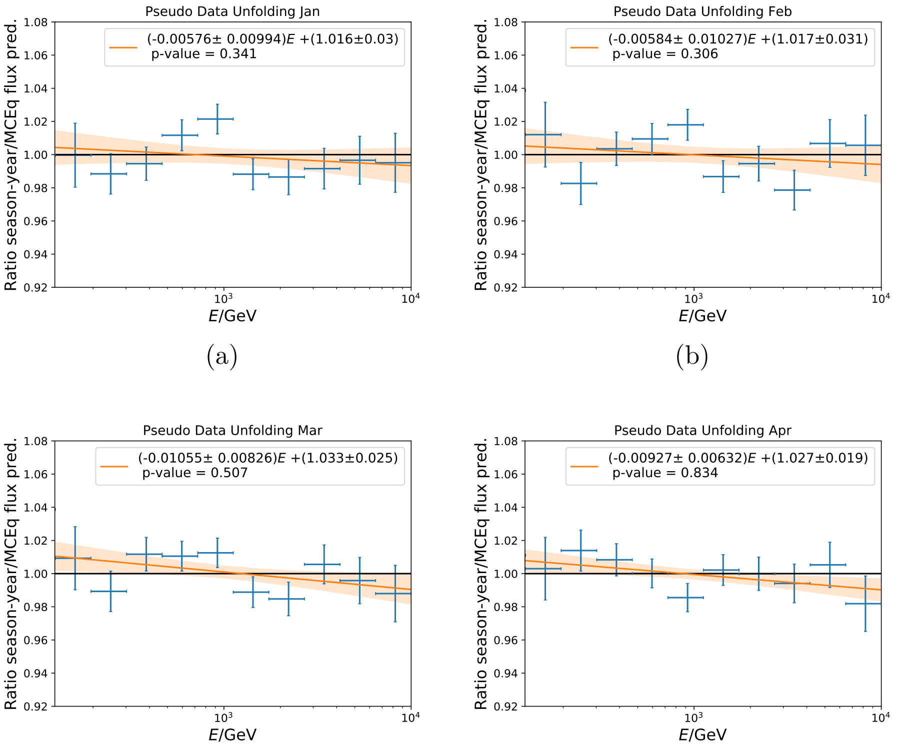

(a) (b)

(c) (d)

Figure B.7: χ^2-test to determine the accuracy of the unfolded seasonal to annual average in zenith range from 90° to 120°. The null hypothesis to be rejected is defined as the quotient of the ratio of unfolded seasonal to annual average flux to the prediction being compatible with 1. The linear fit determines the slope of the ratio between unfolded ratio from pseudo data to MCEq. The unfolded ratio from the pseudo sample should be compatible with the prediction to ensure the feasibility of seasonal unfolding. The null hypothesis cannot be rejected for both seasons, which indicates that the unfolded ratio is in agreement with the prediction.

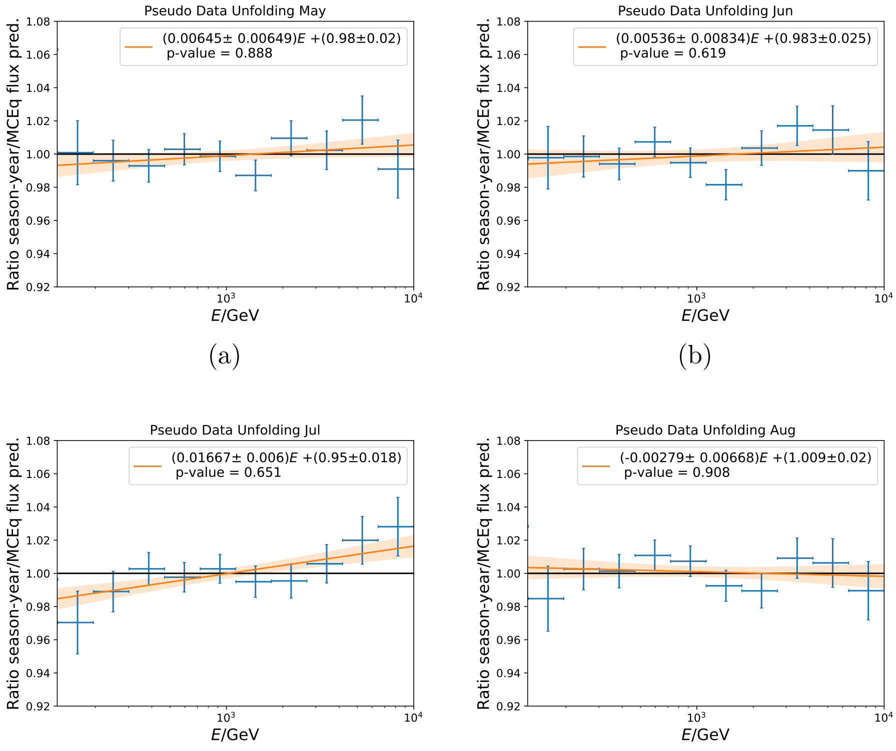

(a) (b)

(c) (d)

Figure B.8: χ^2-test to determine the accuracy of the unfolded seasonal to annual average in zenith range from 90° to 120°. The null hypothesis to be rejected is defined as the quotient of the ratio of unfolded seasonal to annual average flux to the prediction being compatible with 1. The linear fit determines the slope of the ratio between unfolded ratio from pseudo data to MCEq. The unfolded ratio from the pseudo sample should be compatible with the prediction to ensure the feasibility of seasonal unfolding. The null hypothesis cannot be rejected for both seasons, which indicates that the unfolded ratio is in agreement with the prediction.

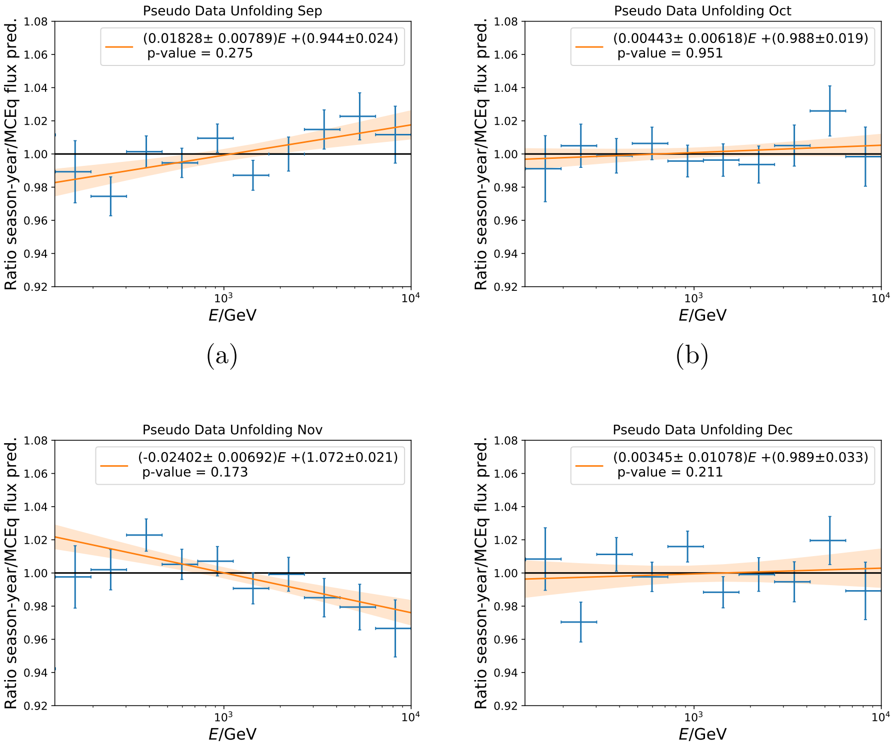

(a) (b)

(c) (d)

Figure B.9: χ^2-test to determine the accuracy of the unfolded seasonal to annual average in zenith range from 90° to 120°. The null hypothesis to be rejected is defined as the quotient of the ratio of unfolded seasonal to annual average flux to the prediction being compatible with 1. The linear fit determines the slope of the ratio between unfolded ratio from pseudo data to MCEq. The unfolded ratio from the pseudo sample should be compatible with the prediction to ensure the feasibility of seasonal unfolding. The null hypothesis cannot be rejected for both seasons, which indicates that the unfolded ratio is in agreement with the prediction.

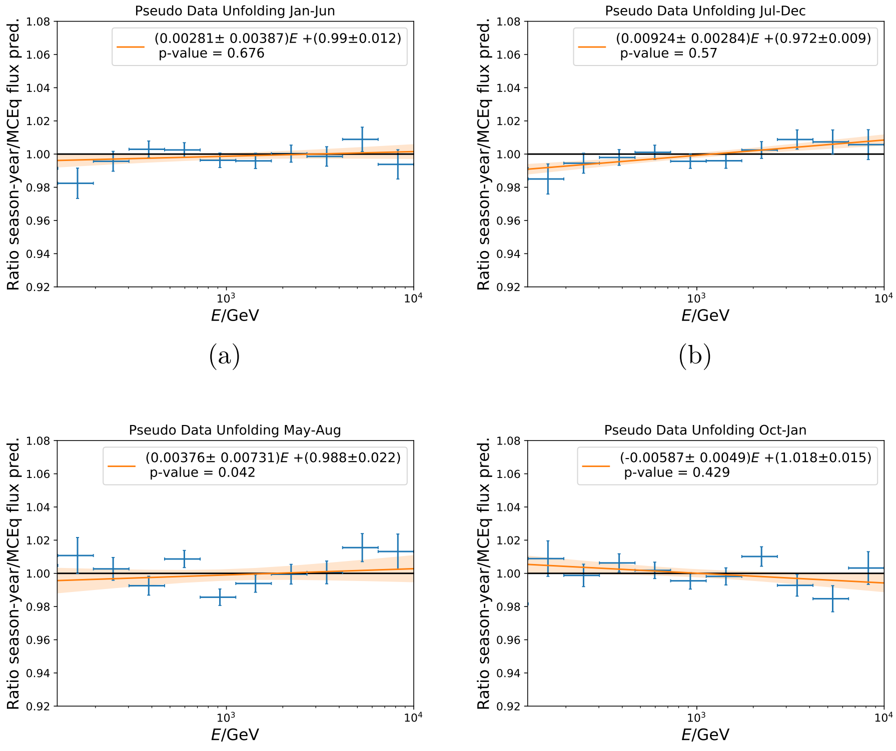

(a) (b)

(c) (d)

Figure B.10: χ^2-test to determine the accuracy of the unfolded seasonal to annual average in zenith range from 90° to 120°. The null hypothesis to be rejected is defined as the quotient of the ratio of unfolded seasonal to annual average flux to the prediction being compatible with 1. The linear fit determines the slope of the ratio between unfolded ratio from pseudo data to MCEq. The unfolded ratio from the pseudo sample should be compatible with the prediction to ensure the feasibility of seasonal unfolding. The null hypothesis cannot be rejected for both seasons, which indicates that the unfolded ratio is in agreement with the prediction.

B.5.2 Robustness Against Changes in Spectral Shape

A χ^2-test can be utilized to evaluate the robustness of the unfolding to possible changes of the spectral index in measured data compared to the flux model assumption for the algorithm training. The feasibility of seasonal unfolding is investigated on a pseudo sample weighted by seasonal predictions from MCEq (see Chapter 7.4.1). However, the spectrum of the data might be distributed differently. To test the feasibility of seasonal unfolding, the pseudo samples for June and December are re-weighted to a shift $\Delta\gamma$ in the spectral index:

$$\phi \cdot \left(\frac{E}{1\,\mathrm{TeV}}\right)^{\Delta\gamma} . \tag{B.1}$$

The pseudo samples are unfolded for four different spectral index scaling factors, and the ratio of monthly to annual average flux is calculated. The resulting ratios are then compared to the expected values from the rescaled MCEq predictions, defined as a quotient. The null hypothesis to be rejected is defined as a quotient of 1, similar to the previous section. As introduced previously, the rejection threshold is set at the 3σ-level for p-values ≤ 0.003.

The test results are depicted in Fig. B.11 for June and in Fig. B.12 for December. The null hypothesis cannot be rejected for both seasons up to $\Delta\gamma \pm 0.1$.

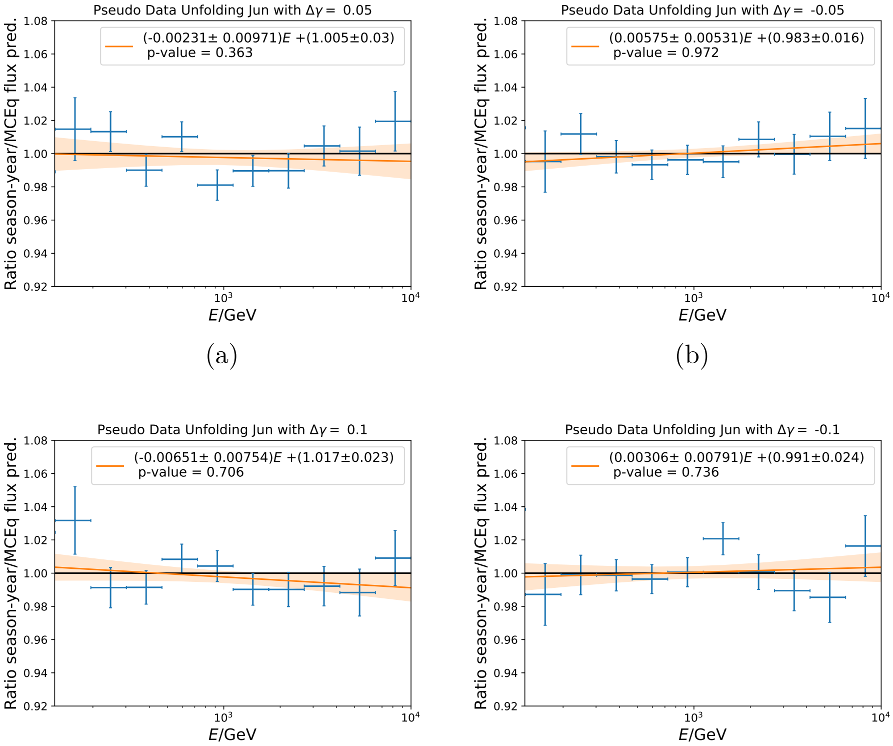

(a) (b)

(c) (d)

Figure B.11: χ^2-test to determine if the ratio can be accurately unfolded with a shifted spectral index of $\Delta\gamma$ in comparison to the training spectrum for the month of June. The pseudo data is sampled based on MCEq flux weights and the flux undergoes a spectral index shift. The fitting process calculates the slope of the ratio between the unfolded ratios derived from pseudo data and MCEq. The ratio of the unfolded seasonal flux ratio to the prediction is defined as the quotient, depicted for each energy bin. If the unfolded ratios are compatible with the prediction, then the quotient is 1, defined as the null hypothesis. In this scenario, the flux ratio can be unfolded, even if the spectral index changes with respect to the training spectrum.

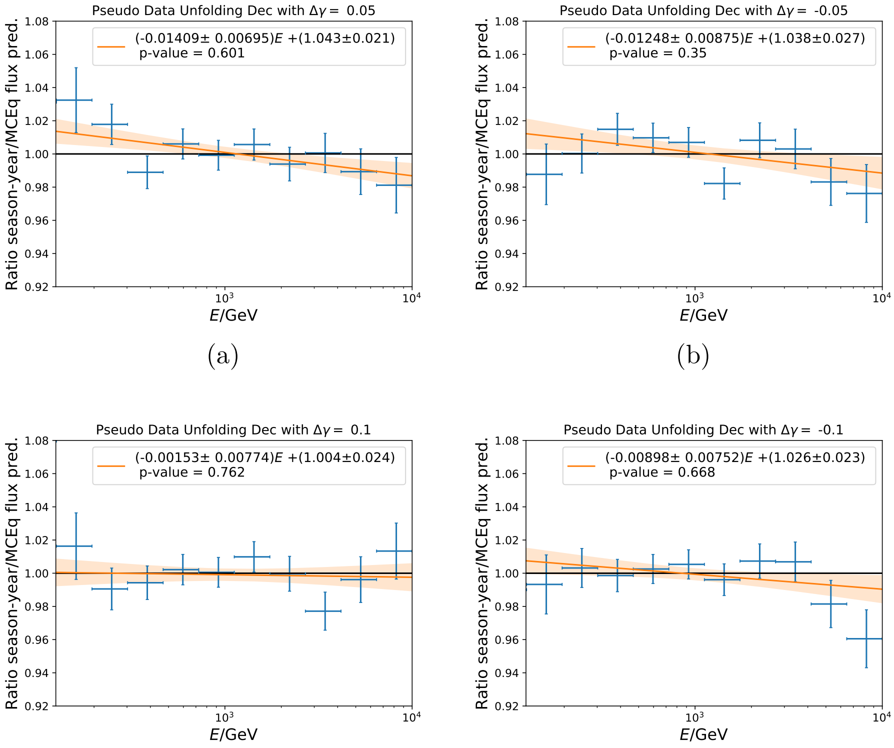

(a) (b)

(c) (d)

Figure B.12: χ^2-test to determine if the ratio can be accurately unfolded with a shifted spectral index of $\Delta\gamma$ in comparison to the training spectrum for the month of December. The pseudo data is sampled based on MCEq flux weights and the flux undergoes a spectral index shift. The fitting process calculates the slope of the ratio between the unfolded ratios derived from pseudo data and MCEq. The ratio of the unfolded seasonal flux ratio to the prediction is defined as the quotient, depicted for each energy bin. If the unfolded ratios are compatible with the prediction, then the quotient is 1, defined as the null hypothesis. In this scenario, the flux ratio can be unfolded, even if the spectral index changes with respect to the training spectrum.

B.5.3 Compatibility of the unfolded Seasonal Variation Strength with MCEq

To determine whether the unfolded ratio of seasonal to annual mean flux is consistent with the seasonal prediction from MCEq, another χ^2-test is performed. The quotient of the ratio of the unfolded seasonal to annual average flux to the MCEq prediction is the target quantity to describe the deviation from the prediction. The null hypothesis assumes that the predictions of the seasonal flux ratio are in agreement with MCEq, equivalent to a quotient of 1. If the obtained ratio is in agreement with MCEq, the variation pattern would follow the prediction of the atmospheric model NRLMSISE-00. As illustrated in Section B.4.2, the ratio of the predicted seasonal to annual average flux remains the same even if primary CR composition and hadronic interaction model are exchanged in the calculation of the seasonal flux ratio. The null hypothesis is rejected at a significance level of 3σ or p-values ≤ 0.003, as in the previous tests. The test results for all seasons are depicted in Fig. B.13 to B.15, and summarized in Table 7.2. The null hypothesis is rejected for February, September, October, and the seasons December-February, January-June, May-August, and October-January.

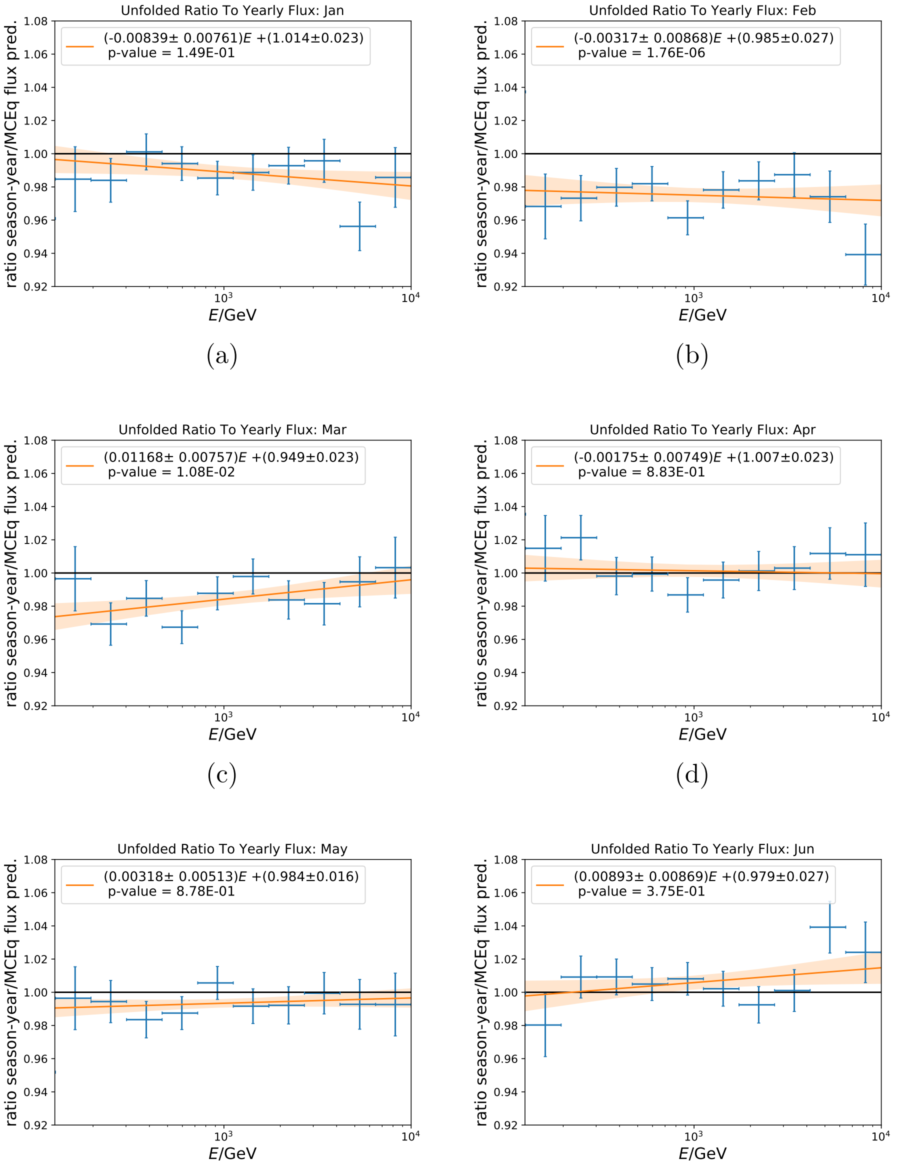

(a) (b)

(c) (d)

(e) (f)

Figure B.13: χ^2-test to determine the compatibility of unfolded seasonal flux ratios with the predicted ratio by MCEq. The error bars depict statistical uncertainties in the ratio from the unfolding. The p-value for each season is given in the caption. The ratio of the unfolded results to the MCEq prediction is fitted by a linear function to show potential offsets to the prediction.

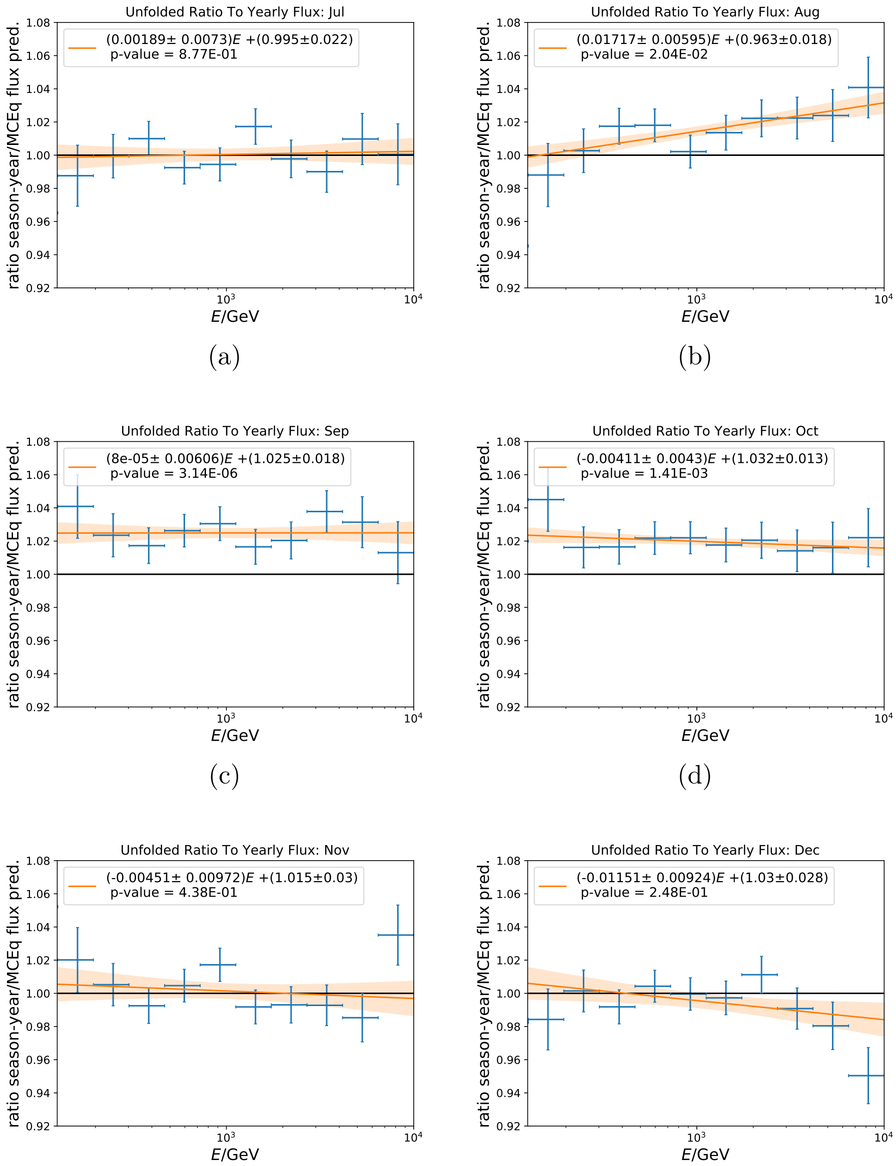

(a) (b) (c) (d) (e) (f)

Figure B.14: χ^2-test to determine the compatibility of unfolded seasonal flux ratios with the predicted ratio by MCEq. The error bars depict statistical uncertainties in the ratio from the unfolding. The p-value for each season is given in the caption. The ratio of the unfolded results to the MCEq prediction is fitted by a linear function to show potential offsets to the prediction.

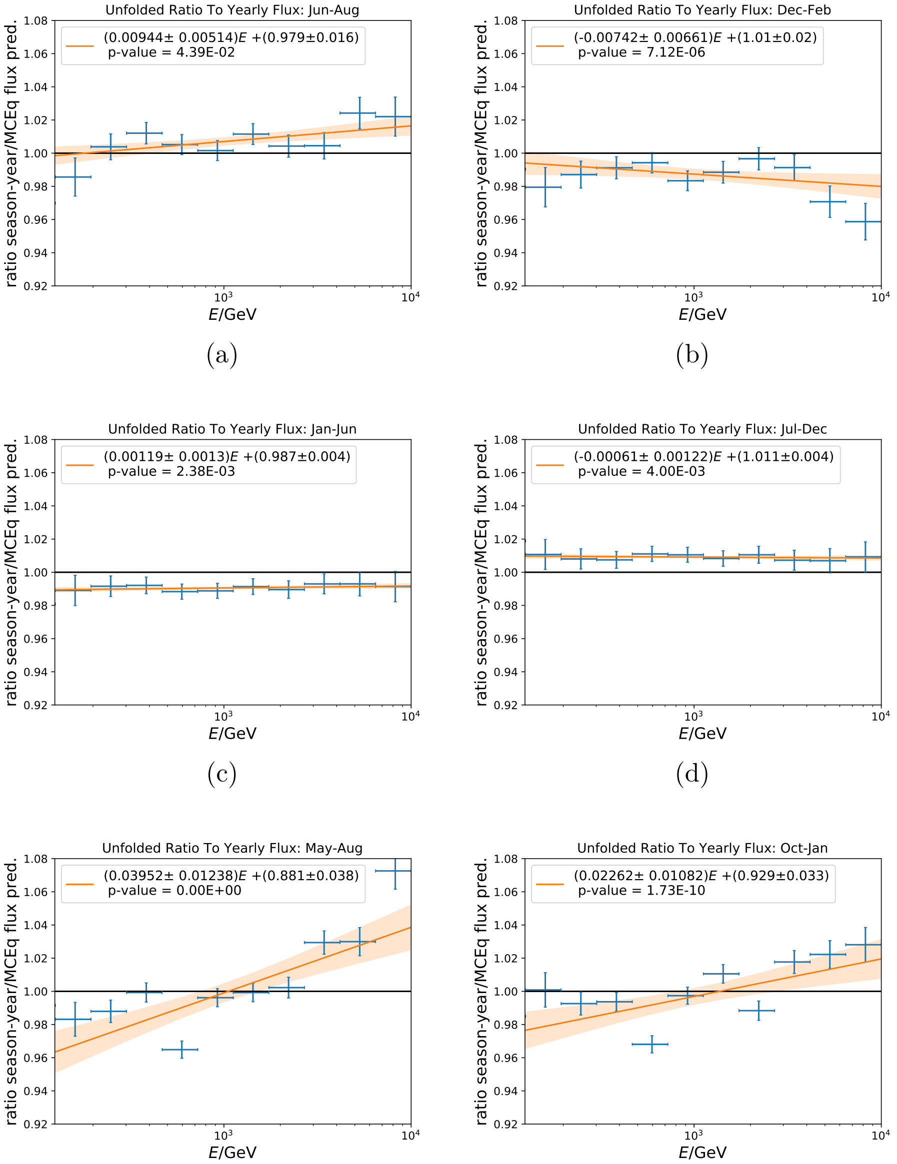

(a)

(b)

(c)

(d)

(e)

(f)

Figure B.15: χ^2-test to determine the compatibility of unfolded seasonal flux ratios with the predicted ratio by MCEq. The error bars depict statistical uncertainties in the ratio from the unfolding. The p-value for each season is given in the caption. The ratio of the unfolded results to the MCEq prediction is fitted by a linear function to show potential offsets to the prediction.

B.6 Redefining the Seasons

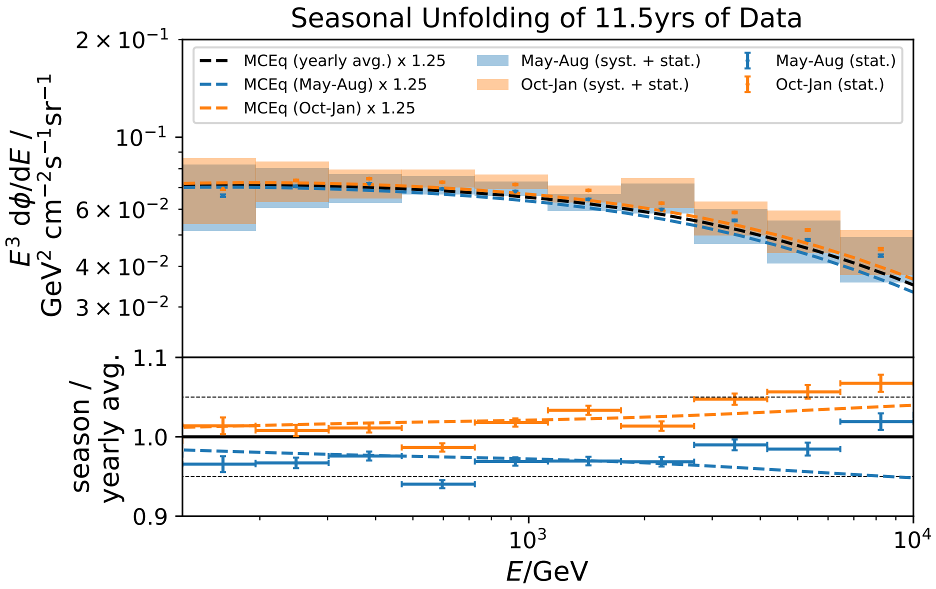

Figure B.16: Unfolded seasonal muon neutrino spectra for redefined austral summer from October to January and austral winter from May to August. Error bars depict statistical uncertainties while colored bands depict systematic ones. The predicted flux from MCEq is scaled up by a fitted normalization constant for the unfolded spectrum. The lower panel displays the ratio of the seasonal to annual average flux for the unfolded data and the MCEq-calculated theory fluxes. Black dashed lines illustrate ±5% deviation from the annual average flux. Since the systematic uncertainties remain the same for each season and cancel out in the ratio, the statistical uncertainties are the only uncertainties in the ratio.

As can be concluded from the discussions in Chapter 7.5, the observed seasonal variations are not distributed symmetrically throughout the year. The seasons are redefined by months with a similar significance of deviations from the annual average flux. The unfolded spectra for the austral summer from October to January, and austral winter from May to August are depicted in Fig. B.16. The fitted normalization factor of the predicted MCEq flux remains the same as in the previously shown figures. The unfolded spectra overlap for both seasons due to the systematic uncertainties and are shape-wise in agreement with the MCEq flux prediction. The amplitude of the unfolded ratio of seasonal to annual average remains constant around +1% to +2% with increasing energy, except between approx. 500 GeV to 700 GeV where the seasonal variations strength decreases to $(-1.3 \pm 0.5)\%$ for austral summer. The unfolded ratio increases at energies above 3 TeV with a strength of $(+4.7 \pm 0.7)\%$ to $(+6.7 \pm 1.1)\%$. The unfolded flux ratio for May to August remains approx. constant around −1% to −2% compared to the annual average, but decreases to $(-6.0 \pm 0.5)\%$ between 500 GeV to 700 GeV. The ratio also increases at energies above 3 TeV to a maximum variation strength of $(+1.9 \pm 1.0)\%$ above 7 TeV. The unfolded ratios are not in agreement with the MCEq predictions because of a sudden decrease in variation strength between 500 GeV to 700 GeV and the sudden increase in the ratio from May to August, which is supported by the χ^2-tests displayed in Fig. B.15.

B.7 Unfolded Annual Average Flux

Bin	Energy / GeV	Mean Energy / GeV	$E^3 \frac{\mathrm{d}E}{\mathrm{d}\phi}$ / $\mathrm{GeV}^2\,\mathrm{cm}^{-2}\,\mathrm{s}^{-1}\,\mathrm{sr}^{-1}$	Stat. Error / / %	Syst. + Stat. Error / %
1	125 – 195	160	6.84×10^{-2}	±0.5	+17.1 −21.1
2	195 – 302	248	7.30×10^{-2}	±0.3	+12.1 −13.4
3	302 – 468	385	7.37×10^{-2}	±0.3	+5.2 −11.6
4	468 – 724	596	7.37×10^{-2}	±0.3	+3.2 −3.3
5	724 – 1122	923	7.03×10^{-2}	±0.3	+2.9 −2.7
6	1122 – 1738	1430	6.64×10^{-2}	±0.3	+4.0 −5.5
7	1738 – 2692	2215	6.18×10^{-2}	±0.3	+14.9 −2.3
8	2692 – 4169	3430	5.60×10^{-2}	±0.3	+9.9 −9.0
9	4169 – 6457	5313	4.90×10^{-2}	±0.4	+15.4 −10.7
10	6457 – 1×10^4	8228	4.24×10^{-2}	±0.5	+13.6 −11.0

Table B.2: Unfolded average yearly atmospheric muon neutrino flux in the zenith range from 90° to 120°.

C Unfolding of the Zenith Range from 90° to 110°

C.1 Dataset

Season	Number of Events	Livetime / days
May-August	129753	1438.5
October-January	133950	1392.3
full year	386542	4137.5

Table C.1: Number of events and livetime per season within the zenith range from 90° to 110° from May 2011 to December 2022.

C.2 Reevaluation of Systematic Uncertainties

Due to the change in the dataset towards a restriction of the zenith range in Chapter 8, systematic uncertainties need to be estimated for the restricted range. Pseudo samples are generated from simulated events with varied systematic parameters, as described in Chapter 7.2. The determined uncertainties for each origin are depicted in Fig. C.1. Compared to the uncertainties obtained for the entire zenith region from 90° to 120° (Fig. 7.3), the scattering and hole ice parameters have the largest impact on the total systematic uncertainty and are larger than the respective uncertainties due to DOM efficiency and absorption at higher energies. To summarize, the uncertainties for the limited range of zenith angles differ from the calculated uncertainties for the zenith range between 90° to 120°. This is due to the behavior of DSEA+ when another spectrum is unfolded, thereby resulting in a slight difference between the spectrum for the restricted zenith range and the training spectrum. The uncertainties reflect this effect, which could be attributed to the unchanged training sample governing the entire zenith range. DOM efficiency and absorption have a minor impact compared to Fig. 7.3. The choice of the CR composition model/hadronic interaction model on the weighting is negligible. The deviation of the number of events per energy bin for a given systematic parameter is illustrated in Fig. C.2.

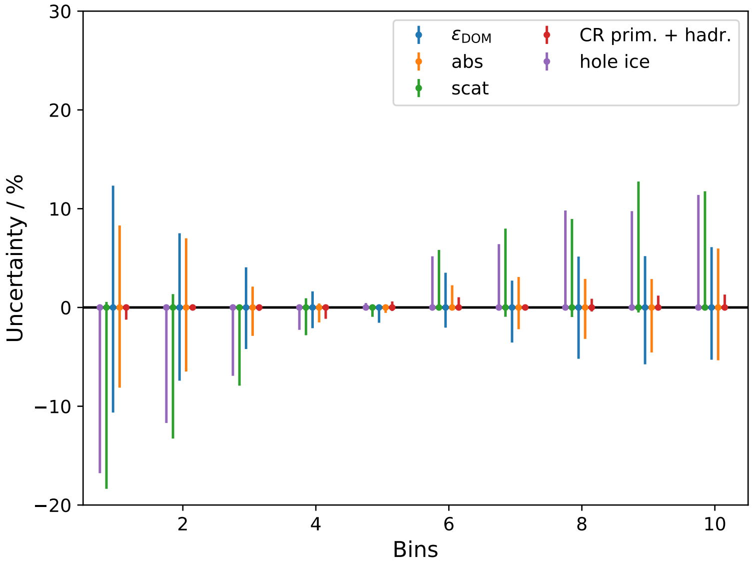

Figure C.1: Overview of each source of systematic uncertainty per energy bin. Due to the relative uncertainty estimation, the systematic uncertainties remain constant for all seasons.

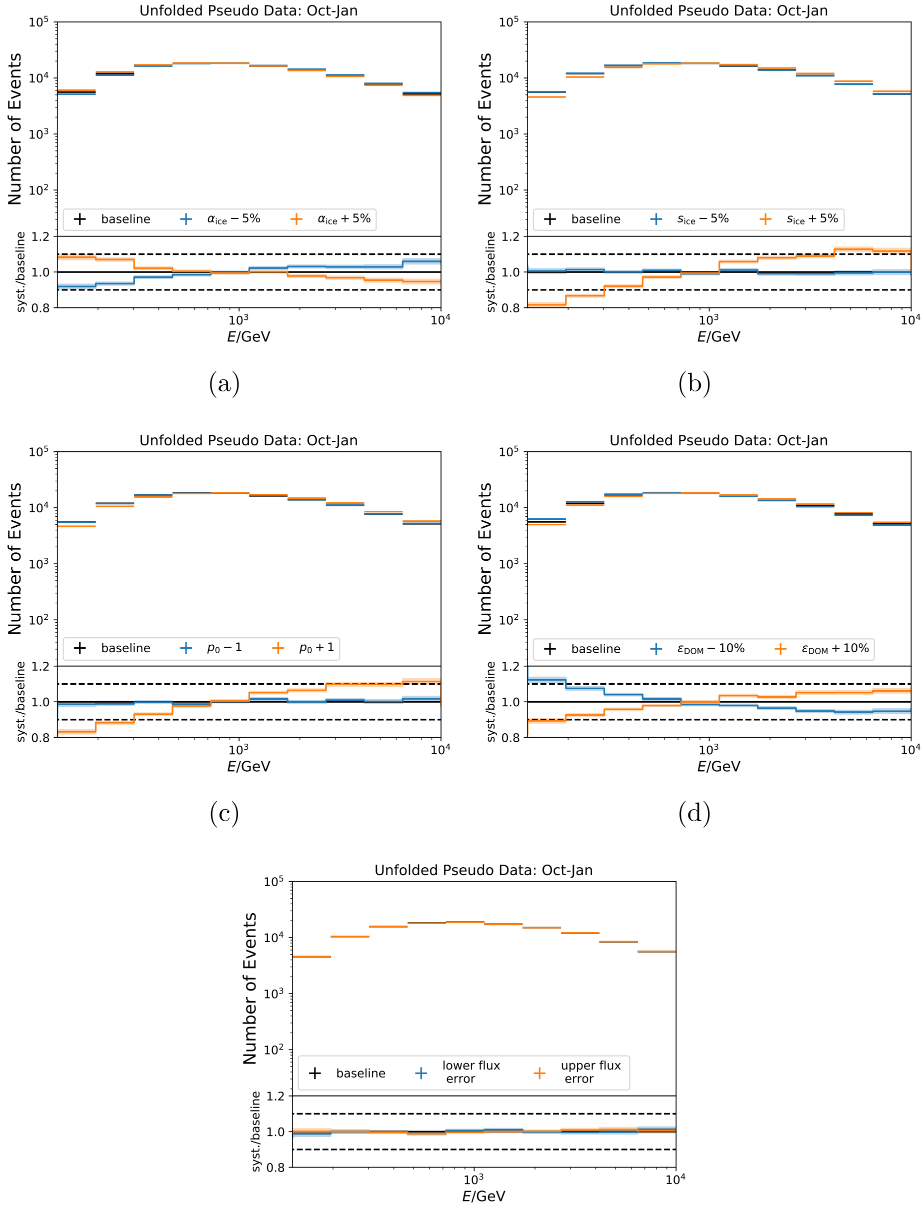

(a) (b) (c) (d) (e)

Figure C.2: Unfolded event spectra for the systematic and reference pseudo samples, exemplary for the season from October to January. The statistical uncertainties in the ratio are illustrated as shaded bands.

C.2.1 Robustness Against Changes in Spectral Shape

As explained in Appendix B.5.2, a χ^2-test can be performed for the evaluation of the robustness of the unfolding to possible changes of the spectral index of measured data. The pseudo samples for austral summer and winter are reweighted to a shift $\Delta\gamma$ in the spectral index according to Equ. B.1. The pseudo samples are unfolded for four different spectral index scaling factors, and the ratio of monthly to annual average flux is calculated. The resulting ratios are then compared to the expected values from the rescaled MCEq predictions, defined as a quotient. The null hypothesis to be rejected is defined as a quotient of 1, similar to the previous section. As introduced previously, the rejection threshold is set at the 3σ-level for p-values ≤ 0.003.
The test results are depicted in Fig. C.3 for austral winter from May to August and in Fig. C.4 for austral summer from October to January. The null hypothesis cannot be rejected for both seasons up to $\Delta\gamma \pm 0.1$.

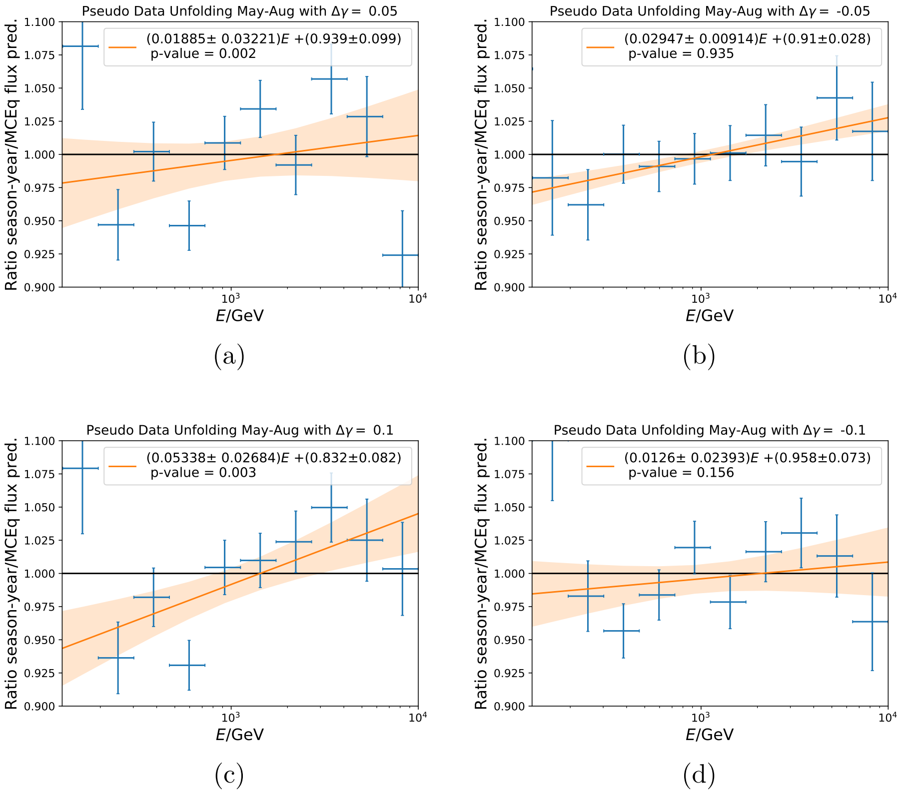

(a) (b)

(c) (d)

Figure C.3: χ^2-test to determine if the ratio can be accurately unfolded with a shifted spectral index of $\Delta\gamma$ in comparison to the training spectrum for austral winter. The pseudo data is sampled based on MCEq flux weights and the flux undergoes a spectral index shift. The fitting process calculates the slope of the ratio between the unfolded ratios derived from pseudo data and MCEq. The ratio of the unfolded seasonal flux ratio to the prediction is defined as the quotient, depicted for each energy bin. If the unfolded ratios are compatible with the prediction, then the quotient is 1, defined as the null hypothesis. In this scenario, the flux ratio can be unfolded, even if the spectral index changes with respect to the training spectrum.

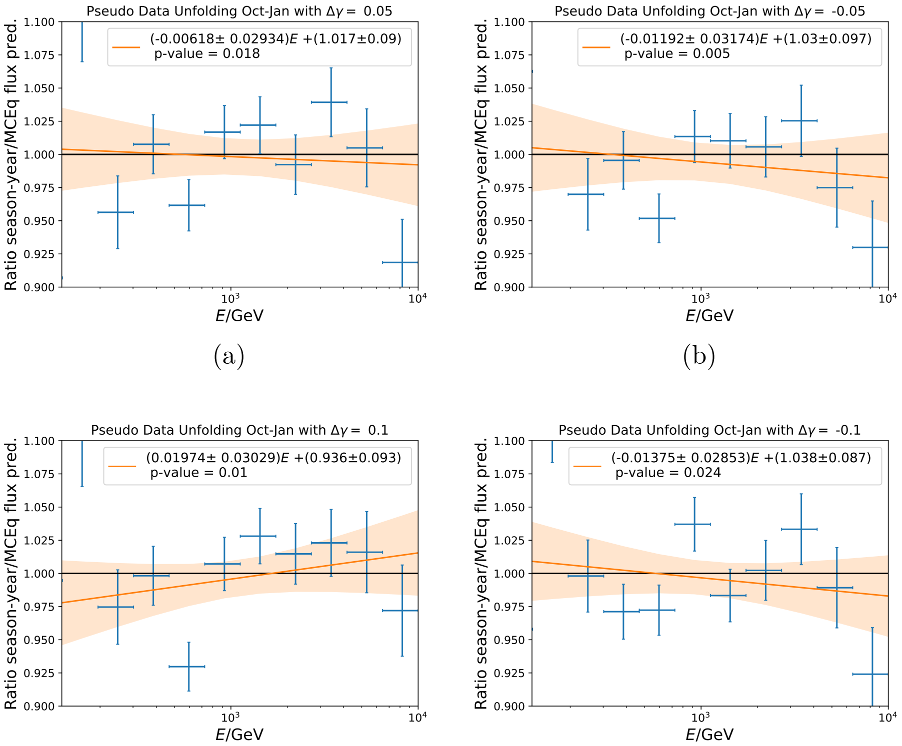

(a) (b)

(c) (d)

Figure C.4: χ^2-test to determine if the ratio can be accurately unfolded with a shifted spectral index of $\Delta\gamma$ in comparison to the training spectrum for austral summer. The pseudo data is sampled based on MCEq flux weights and the flux undergoes a spectral index shift. The fitting process calculates the slope of the ratio between the unfolded ratios derived from pseudo data and MCEq. The ratio of the unfolded seasonal flux ratio to the prediction is defined as the quotient, depicted for each energy bin. If the unfolded ratios are compatible with the prediction, then the quotient is 1, defined as the null hypothesis. In this scenario, the flux ratio can be unfolded, even if the spectral index changes with respect to the training spectrum.

C.3 Unfolded Annual Average Flux

Bin	Energy / GeV	Mean Energy / GeV	$E^3 \frac{\mathrm{d}E}{\mathrm{d}\phi}$ / $\mathrm{GeV}^2\,\mathrm{cm}^{-2}\,\mathrm{s}^{-1}\,\mathrm{sr}^{-1}$	Stat. Error / / %	Syst. + Stat. Error / %
1	125 – 195	160	7.47×10^{-2}	±0.6	+16.0 −29.4
2	195 – 302	248	7.95×10^{-2}	±0.4	+11.1 −20.9
3	302 – 468	385	8.12×10^{-2}	±0.3	+5.1 −12.3
4	468 – 724	596	8.23×10^{-2}	±0.3	+2.4 −5.1
5	724 – 1122	923	7.88×10^{-2}	±0.3	+1.3 −2.4
6	1122 – 1738	1430	7.51×10^{-2}	±0.3	+9.4 −2.6
7	1738 – 2692	2215	6.98×10^{-2}	±0.3	+11.6 −4.8
8	2692 – 4169	3430	6.32×10^{-2}	±0.3	+15.2 −6.8
9	4169 – 6457	5313	5.50×10^{-2}	±0.4	+17.9 −8, 1
10	6457 – 1×10^4	8228	4.77×10^{-2}	±0.6	+19.4 −11.0

Table C.2: Unfolded average yearly atmospheric muon neutrino flux from May 2011 to 2022 in the zenith range from 90° to 110°.

D Atmospheric Models in MCEq

This section introduces atmospheric parameterizations in MCEq. The density profiles can be provided by a numerical model or by measured/interpolated data. The description of the atmospheric density is crucial for the calculation of the lepton fluxes. The consideration of temperature variations on a monthly or daily basis allows the prediction of seasonal lepton flux variations. The first section introduces the atmospheric parameterization utilized in this dissertation, the second section compares the models/data-based approaches to one another.

D.1 Description of Models and Databases

D.1.1 NRLMSISE-00

MSIS models describe the composition, density, and temperature of the atmosphere at selected altitudes. These models combine data from mass spectrometers and incoherent scattering radar observations with theoretical predictions of atmospheric observables. The first model MSIS-86 [163] was developed primarily to describe the thermosphere and has been extended to include additional layers of the atmosphere. The extension US Naval Research Laboratory Mass Spectrometer Incoherent Scattering Extension 2000 (NRLMSISE-00) [4] incorporated data from the US Naval Research Laboratory and expanded the previous model from the ground to the exosphere in 2000.
Various quantities such as temperature and altitude, but also element abundance densities can be obtained from the model from the following inputs: day, time of day, geodetic altitude from 0 km to 1000 km, geodetic latitude-longitude, local apparent solar time, 81-day average of F10.7, solar flux, daily F10.7 solar flux for the previous day, and daily magnetic index. However, changes from year to year cannot be taken into account.

D.1.2 US Standard Atmosphere

The US Standard Atmosphere is used as a parametrization [58] of the atmospheric density in CORSIKA [164]. The slant depth of the atmosphere is approximated in five different layers depending on the height. The first four layers below 100 km are approximated by:

$$X(h) = a_i + b_i \exp\left(-\frac{h}{c_i}\right). \tag{D.1}$$

The fifth layer is represented by a linear relation:

$$X(h) = a_i - \frac{b_i h}{c_i}. \tag{D.2}$$

The exact parameters can be found in Ref. [164]. Depending on position and season, different parameters can be selected.

D.1.3 AIRS

The Atmospheric Infrared Sounder (AIRS) [123] is an instrument on NASA's Aqua satellite. The device is designed to measure infrared radiation emitted in the atmosphere with the central goal of providing vertical profiles of temperature and humidity. It is particularly sensitive to the lower stratosphere and troposphere. Temperature profiles are obtained at least twice daily at pressure levels ranging from 0.1 hPa to 1000 hPa with an angular resolution of $1° \times 1°$. The obtained profiles from April 2012 to April 2017 are fed into the modified version of MCEq used in Ref. [1]. Heights above 50 km are interpolated by NRLMSISE-00 [7].

D.1.4 ECMWF

The ERA reanalysis datasets provided by the European Center for Medium-Range Weather Forecasts (ECMWF) [161] are numerical weather prediction models that were developed using a variety of observational data. The latest version available, which is used in this thesis, is the ERA-5 version. It includes a collection of satellite measurements and weather stations from 1979 to the present. The combination of many measurements forms a continuous dataset, which has a larger coverage compared to AIRS. The current version of ERA-5 has a high spatial resolution and provides data on an hourly basis. The vertical temperature profiles between April 2012 and April 2013 are fed into the modified version of MCEq by Ref. [1].

D.2 Comparison of Atmospheres

The predicted rate from MCEq is investigated in comparison to the observed neutrino rate in IceCube for different zenith bands in Chapter 8.1. The impact of the atmospheric model in MCEq on the predicted average monthly neutrino rate is depicted in Fig. D.1 in three distinct zenith bands of 10° width and the final range from 90° to 110°.

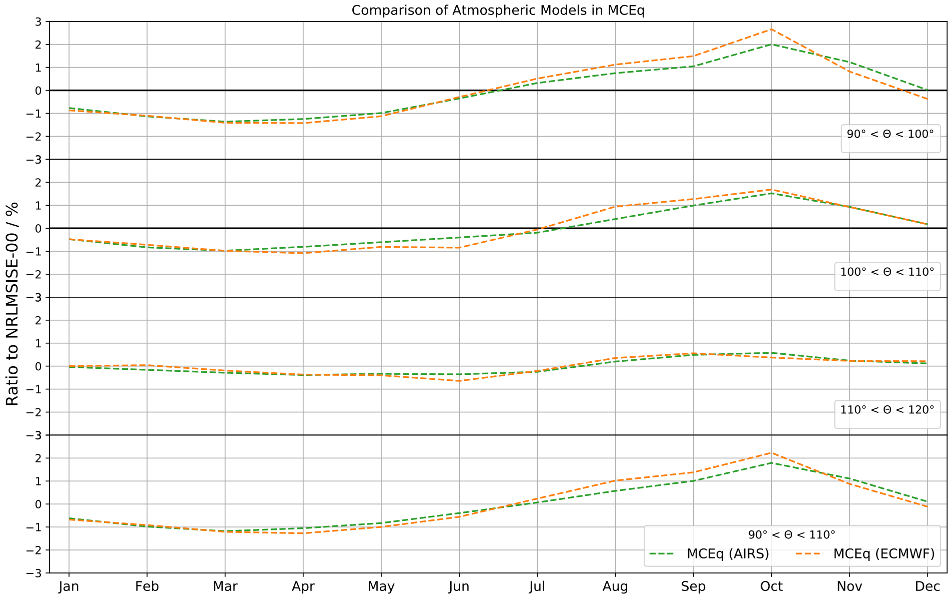

Figure D.1: Ratio of the monthly average muon neutrino fluxes calculated with MCEq with temperature data from AIRS and ECMWF to the empirical model NRLMSISE-00 as atmospheric input for different zenith bands. The MCEq flux is calculated using H3a as the primary CR composition and Sibyll2.3c as the hadronic interaction model. The prediction from temperature data differs from the NRLMSISE-00 prediction by up to 2% in spring and fall, especially in October. Small deviations between the AIRS and ECMWF predictions occur from August to December in the zenith range of 90° to 100°.

Dashed lines show the ratio of the calculated monthly average neutrino rate based on AIRS and ECMWF compared to NRLMSISE-00. The ratios obtained from AIRS and ECMWF are similar except for sub-percent level deviation between August and November in the zenith ranges from 90° to 110°. The data-based approaches are in agreement with NRLMSISE-00 in June/July and in December, as discussed in Chapter 7. Deviations of up to 2% are observable in October. A general overestimation using NRLMSISE-00 occurs from January to June and an underestimation from July to December. The deviation are largest close to the Pole in October, which could be attributed to SSW in the South Pole atmosphere, which is not modeled in NRLMSISE-00. To accurately compare the unfolded seasonal variation strength with theory predictions, data-based temperature profiles need to be implemented in the flux calculation from MCEq.

Bibliography

[1] R. Abbasi et al. “Observation of seasonal variations of the flux of high-energy atmospheric neutrinos with IceCube”. In: Eur. Phys. J. C 83 (2023). DOI: `10.1140/epjc/s10052-023-11679-5`.

[2] T. K. Gaisser. “Spectrum of cosmic-ray nucleons, kaon production, and the atmospheric muon charge ratio”. In: Astroparticle Physics 35 (2011).

[3] F. Riehn et al. “The hadronic interaction model Sibyll 2.3c and Feynman scaling”. In: Proceedings, 35th International Cosmic Ray Conference (2017).

[4] J. Picone et al. “NRLMSISE-00 empirical model of the atmosphere: Statistical comparison and scientific issues”. In: Journal of Geophysical Research 107 (2002). DOI: `10.1029/2002JA009430`.

[5] M. G. Aartsen et al. “The IceCube Neutrino Observatory: Instrumentation and Online Systems”. In: JINST 12 (2017). DOI: `10.1088/1748-0221/12/03/P03012`.

[6] Mirko Bunse et al. “Unification of Deconvolution Algorithms for Cherenkov Astronomy”. In: 5th International Conference on Data Science and Advanced Analytics (DSAA). IEEE. 2018.

[7] A. Fedynitch et al. “Calculation of conventional and prompt lepton fluxes at very high energy”. In: EPJ Web Conf. 99 (2015). Ed. by D. Berge et al. DOI: `10.1051/epjconf/20159908001`.

[8] IceCube Collaboration et al. “Neutrino emission from the direction of the blazar TXS 0506+056 prior to the IceCube-170922A alert”. In: Science 361 (2018). DOI: `10.1126/science.aat2890`.

[9] R. Abbasi et al. “Evidence for neutrino emission from the nearby active galaxy NGC 1068”. In: Science 378 (2022). DOI: `10.1126/science.abg3395`.

[10] R. Abbasi et al. “Observation of high-energy neutrinos from the Galactic plane”. In: Science 380 (2023). DOI: `10.1126/science.adc9818`.

[11] IceCube Collaboration. [Online: 13/09/2023]. URL: `https://gallery.icecube.wisc.edu`.

[12] T. K. Gaisser, R. Engel, and E. Resconi. Cosmic Rays and Particle Physics: 2nd Edition. Cambridge University Press, June 2016. ISBN: 978-0-521-01646-9.

[13] V. F. Hess. “Über Beobachtungen der durchdringenden Strahlung bei sieben Freiballonfahrten”. In: Phys. Z. 13 (1912).

[14] A. Aab et al. “The Pierre Auger Cosmic Ray Observatory”. In: Nucl. Instrum. Meth. A 798 (2015). DOI: `10.1016/j.nima.2015.06.058`.

[15] H. Kawai et al. “Telescope Array Experiment”. In: Nuclear Physics B - Proceedings Supplements 175-176 (2008). DOI: `https://doi.org/10.1016/j.nuclphysbps.2007.11.002`.

[16] A. Coleman et al. “Ultra-high-energy cosmic rays The intersection of the Cosmic and Energy Frontiers”. In: Astroparticle Physics 149 (Feb. 2023). DOI: `10.1016/j.astropartphys.2023.102819`.

[17] H. Dembinski et al. “Data-driven model of the cosmic-ray flux and mass composition from 10 GeV to 10^{11} GeV”. In: Proceedings of the 35th International Cosmic Ray Conference (2017). DOI: `10.22323/1.301.0533`.

[18] W. D. Apel et al. “Kneelike Structure in the Spectrum of the Heavy Component of Cosmic Rays Observed with KASCADE-Grande”. In: Phys. Rev. Lett. 107 (17 2011). DOI: `10.1103/PhysRevLett.107.171104`.

[19] R. Abbasi et al. “First Observation of the Greisen-Zatsepin-Kuzmin Suppression”. In: Phys. Rev. Lett. 100 (2008). DOI: `10.1103/PhysRevLett.100.101101`.

[20] J. Abraham et al. “Observation of the suppression of the flux of cosmic rays above 4×10^{19}eV”. In: Phys. Rev. Lett. 101 (2008). DOI: `10.1103/PhysRevLett.101.061101`.

[21] A. Aab et al. “Features of the Energy Spectrum of Cosmic Rays above 2.5×10^{18} eV Using the Pierre Auger Observatory”. In: Phys. Rev. Lett. 125 (2020). DOI: `10.1103/PhysRevLett.125.121106`.

[22] D. Ivanov et al. “Recent measurement of the Telescope Array energy spectrum and observation of the shoulder feature in the Northern Hemisphere”. In: Proceedings of the 37th International Cosmic Ray Conference (2021). DOI: `10.22323/1.395.0341`.

[23] A. M. Hillas. “The Origin of Ultra-High-Energy Cosmic Rays”. In: Ann. Rev. of Astron and Astrophys. 22 (1984). DOI: `10.1146/annurev.aa.22.090184.002233`.

[24] K. Greisen. “End to the Cosmic-Ray Spectrum?” In: Phys. Rev. Lett. 16 (1966). DOI: `10.1103/PhysRevLett.16.748`.

[25] G. T. Zatsepin and V. A. Kuzmin. “Upper limit of the spectrum of cosmic rays”. In: JETP Lett. 4 (1966).

[26] F. W. Stecker. “Photodisintegration of Ultrahigh-Energy Cosmic Rays by the Universal Radiation Field”. In: Phys. Rev. 180 (1969). DOI: `10.1103/PhysRev.180.1264`.

[27] B. Peters. “Primary Cosmic Radiation and Extensive Air Showers”. In: Nuovo Cimento XXII (1961).

[28] T. K. Gaisser, T. Stanev, and S. Tilav. “Cosmic Ray Energy Spectrum from Measurements of Air Showers”. In: Front. Phys. (Beijing) 8 (2013). DOI: `10.1007/s11467-013-0319-7`.

[29] C. de Boor. A Practical Guide to Spline. Vol. 27. 1978. DOI: `10.2307/2006241`.

[30] J. R. Hörandel. “On the knee in the energy spectrum of cosmic rays”. In: Astroparticle Physics 19 (2003). DOI: `10.1016/S0927-6505(02)00198-6`.

[31] C. D. Anderson. “The Positive Electron”. In: Phys. Rev. 43 (1933). DOI: `10.1103/PhysRev.43.491`.

[32] J. C. Street and E. C. Stevenson. “New Evidence for the Existence of a Particle of Mass Intermediate Between the Proton and Electron”. In: Phys. Rev. 52 (1937). DOI: `10.1103/PhysRev.52.1003`.

[33] G. D. Rochester and C. C. Butler. “Evidence for the Existence of New Unstable Elementary Particles”. In: Nature 160 (1947). DOI: `10.1038/160855a0`.

[34] C. M. G. Lattes et al. “Processes involving charged mesons”. In: Nature 159 (1947). DOI: `10.1038/159694a0`.

[35] R. M. Wagner. “Measurement of Very High Energy Gamma-Ray Emission from Four Blazars Using the MAGIC Telescope and a Comparative Blazar Study”. PhD thesis. TU München, 2006.

[36] D. Soldin. “Laterally seperated muons from cosmic ray air showers measured with the IceCube Neutrino Observatory”. PhD thesis. Bergische Universität Wuppertal, 2017.

[37] J. Matthews. “A Heitler model of extensive air showers”. In: Astropart. Phys. 22 (2005). DOI: `10.1016/j.astropartphys.2004.09.003`.

[38] W. Heitler. The quantum theory of radiation. Vol. 5. International Series of Monographs on Physics. Oxford: Oxford University Press, 1936.

[39] J. M. C. Montanus. “An extended Heitler-Matthews model for the full hadronic cascade in cosmic air showers”. In: Astropart. Phys. 59 (2014). DOI: `10.1016/j.astropartphys.2014.03.010`.

[40] P. Lipari. “Lepton spectra in the earth’s atmosphere”. In: Astropart. Phys. 1 (1993). DOI: `10.1016/0927-6505(93)90022-6`.

[41] A. Fedynitch. “Cascade equations and hadronic interactions at very high energies”. PhD thesis. KIT, 2015.

[42] R. Engel, D. Heck, and T. Pierog. “Extensive air showers and hadronic interactions at high energy”. In: Ann. Rev. Nucl. Part. Sci. 61 (2011). DOI: `10.1146/annurev.nucl.012809.104544`.

[43] A. Capella et al. “Dual parton model”. In: Phys. Rept. 236 (1994). DOI: `10.1016/0370-1573(94)90064-7`.

[44] T. Pierog et al. “EPOS LHC : test of collective hadronization with LHC data”. In: Physical Review C 92 (2013). DOI: `10.1103/PhysRevC.92.034906`.

[45] S. Ostapchenko. “Monte Carlo treatment of hadronic interactions in enhanced Pomeron scheme: I. QGSJET-II model”. In: Phys. Rev. D 83 (2011). DOI: `10.1103/PhysRevD.83.014018`.

[46] A. B. Kaidalov and K.-A. Ter-Martirosian. “Multihadron production at high energies in the model of quark-gluon strings. Comparison with experiment”. In: Sov. J. Nucl. Phys. 39 (1984).

[47] S. Roesler, R. Engel, and J. Ranft. “The Monte Carlo event generator DPMJET-III”. In: International Conference on Advanced Monte Carlo for Radiation Physics, Particle Transport Simulation and Applications (2000). DOI: `10.1007/978-3-642-18211-2_166`.

[48] C. L. Cowan et al. “Detection of the Free Neutrino: a Confirmation”. In: Science 124 (1956). DOI: `10.1126/science.124.3212.103`.

[49] P. Mészáros. “Astrophysical Sources of High-Energy Neutrinos in the IceCube Era”. In: Annual Review of Nuclear and Particle Science 67 (2017). DOI: `10.1146/annurev-nucl-101916-123304`.

[50] J. F. Beacom et al. “Measuring Flavor Ratios of High-Energy Astrophysical Neutrinos”. In: Phys. Rev. D 68 (2003). DOI: `10.1103/PhysRevD.68.093005`.

[51] M. Aker et al. “Direct neutrino-mass measurement with subelectronvolt sensitivity”. In: Nature Phys. 18 (2022). DOI: `10.1038/s41567-021-01463-1`.

[52] U. F. Katz and C. Spiering. “High-Energy Neutrino Astrophysics: Status and Perspectives”. In: Progress in Particle and Nuclear Physics 1260 (2012). DOI: `10.1016/j.ppnp.2011.12.001`.

[53] A. Faessler et al. “Can one measure the Cosmic Neutrino Background?” In: International Journal of Modern Physics E 26 (2016). DOI: `10.1142/S0218301317400080`.

[54] R. Davis, D. S. Harmer, and K. C. Hoffman. “Search for Neutrinos from the Sun”. In: Phys. Rev. Lett. 20 (1968). DOI: `10.1103/PhysRevLett.20.1205`.

[55] L. M. Krauss. “Neutrino spectroscopy of supernova 1987A”. In: Nature 329 (1987). DOI: `10.1038/329689a0`.

[56] V. S. Berezinsky and G. T. Zatsepin. “Cosmic rays at ultrahighenergies (neutrino?)” In: Phys. Lett. B 28 (1969). DOI: `10.1016/0370-2693(69)90341-4`.

[57] W. Rhode. “Untersuchung der Energiespektren hochenergetischer Muonen im Fréjusdetektor”. PhD thesis. Bergische Universität Wuppertal, 1993.

[58] N. Sissenwine, M. Dubin, and H. Wexler. “The US standard atmosphere”. In: Journal of Geophysical Research 67 (1962).

[59] A. Fedynitch et al. “Hadronic interaction model sibyll 2.3c and inclusive lepton fluxes”. In: Phys. Rev. D 100 (2019). DOI: `10.1103/PhysRevD.100.103018`.

[60] S. Osprey et al. “Sudden stratospheric warmings seen in MINOS deep underground muon data”. In: Geophys. Res. Lett. 36 (2002). DOI: `10.1029/2008GL036359`.

[61] Paul H. Barrett et al. “Interpretation of Cosmic-Ray Measurements Far Underground”. In: Rev. Mod. Phys. 24 (1952). DOI: `10.1103/RevModPhys.24.133`.

[62] N. Sherman. “Atmospheric Temperature Effect for μ Mesons Observed at a Depth of 846 m.w.e.” In: Phys. Rev. 93 (1954). DOI: `10.1103/PhysRev.93.208`.

[63] M. Ambrosio et al. “Seasonal variations in the underground muon intensity as seen by MACRO”. In: Astropart. Phys. 7 (1997). DOI: `10.1016/S0927-6505(97)00011-X`.

[64] K. Munakata et al. “Time variation of the cosmic ray muon flux in underground detectors and correlation with atmospheric temperature”. In: J. Phys. Soc. Jap. 60 (1991). DOI: `10.1143/JPSJ.60.2808`.

[65] M. C. Goodman. “Seasonal variations in Soudan-2”. In: Proceedings of the 26th International Cosmic Ray Conference (1999).

[66] D. D’Angelo. “Seasonal modulation in the Borexino cosmic muon signal”. In: 32nd International Cosmic Ray Conference (2011). DOI: `10.7529/ICRC2011/V04/0510`.

[67] S. Tilav et al. “Atmospheric Variations as observed by IceCube”. In: Proceedings of the 31th International Cosmic Ray Conference (2010).

[68] P. Desiati et al. “Seasonal Variations of High Energy Cosmic Ray Muons Observed by the IceCube Observatory as a Probe of Kaon/Pion Ratio”. In: Proceedings of the 32nd International Cosmic Ray Conference (2011). DOI: `10.7529/ICRC2011/V01/0662`.

[69] T. K. Gaisser. “Seasonal variation of atmospheric neutrinos in IceCube”. In: Proceedings of the 33rd International Cosmic Ray Conference (2013).

[70] S. Tilav et al. “Seasonal variation of atmospheric muons in IceCube”. In: Proceedings of the 36th International Cosmic Ray Conference (2019). DOI: `10.22323/1.358.0894`.

[71] M. Ackermann and E. Bernardini. "An investigation of seasonal variations in the atmospheric neutrino rate with the AMANDA-II neutrino telescope". In: Proceedings of the 29th International Cosmic Ray Conference (2005).

[72] P. Heix et al. "Seasonal Variation of Atmospheric Neutrinos in IceCube". In: Proceedings of the 36th International Cosmic Ray Conference (2019). DOI: `10.22323/1.358.0465`.

[73] M. Honda et al. "Atmospheric neutrino flux calculation using the
NRLMSISE-00 atmospheric model". In: Phys. Rev. D 92 (2015). DOI: `10.1103/PhysRevD.92.023004`.

[74] M. Honda et al. "Calculation of atmospheric neutrino flux using the interaction model calibrated with atmospheric muon data". In: Phys. Rev. D 75 (2007). DOI: `10.1103/PhysRevD.75.043006`.

[75] E. Andres et al. "The AMANDA neutrino telescope: Principle of operation and first results". In: Astroparticle Physics 13 (2000).

[76] IceCube Collaboration. IceCube Preliminary Design Document. 2001. URL: `https://icecube.wisc.edu/wp-content/uploads/2020/11`.

[77] R. Abbasi et al. "The Design and Performance of IceCube Deep-Core". In: Astroparticle Physics 35 (2012).

[78] R. Abbasi et al. "Calibration and Characterization of the Ice-Cube Photomultiplier Tube". In: Nuclear Instruments and Methods in Physics Research Section A Accelerators Spectrometers Detectors and Associated Equipment 618 (2010). DOI: `10.1016/j.nima.2010.03.102`.

[79] M. Aartsen et al. "IceCube-Gen2: The window to the extreme Universe". In: Journal of Physics G: Nuclear and Particle Physics 48 (2021). DOI: `10.1088/1361-6471/abbd48`.

[80] P. A. Cherenkov. "Visible emission of clean liquids by action of gamma radiation". In: Doklady Akademil Mauk SSE 2 (1937).

[81] I. M. Frank and I. E. Tamm. "Coherent visible radiation of fast electrons passing through matter". In: Compt. Rend. Acad. Sci. URSS 14 (1937). DOI: `10.3367/UFNr.0093.196710o.0388`.

[82] A. Cooper-Sarkar, P. Mertsch, and S. Sarkar. "The high energy neutrino cross-section in the Standard Model and its uncertainty". In: JHEP 08 (2011). DOI: `10.1007/JHEP08(2011)042`.

[83] H. E. Fisk and F. Sciulli. "Charged Current Neutrino Interactions". In: Ann. Rev. Nucl. Part. Sci. 32 (1982). DOI: `10.1146/annurev.ns.32.120182.002435`.

[84] M. G. Aartsen et al. "Evidence for High-Energy Extraterrestrial Neutrinos at the IceCube Detector". In: Science 342 (2013). DOI: `10.1126/science.1242856`.

[85] L. Witthaus. "Unfolding the atmospheric muon spectrum using stopping muons in IceCube". MA thesis. TU Dortmund, 2021.

[86] J. G. Learned and S. Pakvasa. "Detecting tau-neutrino oscillations at PeV energies". In: Astropart. Phys. 3 (1995). DOI: `10.1016/0927-6505(94)00043-3`.

[87] R. Abbasi et al. "The IceCube data acquisition system: Signal capture, digitization, and timestamping". In: Nuclear Instruments and Methods in Physics Research Section A: Accelerators, Spectrometers, Detectors and Associated Equipment 601 (2009).

[88] V. J. Stenger. Track Fitting for the DUMAND II Octagon Array. Tech. rep. University of Hawaii at Manoa, 1990.

[89] G. Sommani. "Analysis of IceCube neutrino data with focus on the study of the angular uncertainty". MA thesis. Universita di Pisa, 2022.

[90] R. Abbasi et al. "LeptonInjector and LeptonWeighter: A neutrino event generator and weighter for neutrino observatories". In: Computer Physics Communications 266 (2021). DOI: `10.1016/j.cpc.2021.108018`.

[91] A. Gazizov and M. P. Kowalski. "ANIS: High energy neutrino generator for neutrino telescopes". In: Comput. Phys. Commun. 172 (2005). DOI: `10.1016/j.cpc.2005.03.113`.

[92] G. C. Hill. "Experimental and theoretical aspects of high energy neutrino astrophysics". PhD thesis. University of Adelaide, 1996.

[93] T. DeYoung. "IceTray: A software framework for IceCube". In: 14th International Conference on Computing in High-Energy and Nuclear Physics (2005).

[94] D. Heck et al. CORSIKA: A Monte Carlo code to simulate extensive air showers. Tech. rep. 1998.

[95] J.-H. Koehne et al. "PROPOSAL: A tool for propagation of charged leptons". In: Computer Physics Communications 184 (2013). DOI: `10.1016/j.cpc.2013.04.001`.

[96] M. Dunsch et al. tudo-astroparticlephysics/PROPOSAL: Zenodo. Mar. 2020. DOI: `10.5281/zenodo.1484180`.

[97] C. Kopper. clsim. URL: `https://github.com/claudiok/clsim`.

[98] K. Schatto. "Stacked searches for high-energy neutrinos from blazars with IceCube". PhD thesis. Johannes Gutenberg Universität Mainz, 2014.

[99] R. Abbasi et al. "A Convolutional Neural Network based Cascade Reconstruction for the IceCube Neutrino Observatory". In: JINST 16 (2021). DOI: `10.1088/1748-0221/16/07/P07041`.

[100] J. Ahrens et al. "Observation of High Energy Atmospheric Neutrinos with the Antarctic Muon and Neutrino Detector Array". In: Phys. Rev. D 66 (2002).

[101] D. Pandel. "Bestimmung von Wasser- und Detektor Parametern und Rekonstruktion von Myonen bis 100 TeV mit dem Baikal Neutrinoteleskop NT-72". Diploma thesis. Humbolt-Universität zu Berlin, 1996.

[102] C. M. Bishop. Pattern Recognition and Machine Learning. Ed. by M. Jordan, J. Kleinberg, and B. Schölkopf. Vol. 4. Information science and statistics 4. Springer, 2006. Chap. Graphical. ISBN: 9780387310732. DOI: `10.1117/1.2819119`.

[103] G. James et al. An Introduction to Statistical Learning: With Applications in R. Springer Publishing Company, Incorporated, 2014. ISBN: 1461471370.

[104] L. Breiman. "Random Forests". In: Machine Learning 45 (2001). DOI: `10.1023/A:1010933404324`.

[105] C. Gini. Variabilità e mutabilità: contributo allo studio delle distribuzioni e delle relazioni statistiche. [Fasc. I.] Studi economico-giuridici pubblicati per cura della facoltà di Giurisprudenza della R. Università di Cagliari. Tipogr. di P. Cuppini, 1912.

[106] R. O. Duda, P. E. Hart, and D. G. Stork. Pattern Classification. 2nd ed. New York: Wiley, 2001. ISBN: 978-0-471-05669-0.

[107] L. Breiman et al. Classification and Regression Trees. Monterey, CA: Wadsworth and Brooks, 1984.

[108] T. Hastie, J. Friedman, and R. Tibshirani. The Elements of Statistical Learning: Data Mining, Inference, and Prediction. Springer Publishing Company, Incorporated, 2017.

[109] F. Pedregosa et al. "Scikit-learn: Machine Learning in Python". In: Journal of Machine Learning Research 12 (2011).

[110] P. Geurts, D. Ernst, and L. Wehenkel. "Extremely randomized trees". In: Machine Learning 63 (2006). DOI: `10.1007/s10994-006-6226-1`.

[111] J. Zhu et al. "Multi-class AdaBoost". In: Statistics and its interface 2 (2006). DOI: `10.4310/SII.2009.v2.n3.a8`.

[112] Y. Freund and R. E. Schapire. "A Decision-Theoretic Generalization of On-Line Learning and an Application to Boosting". In: J. Comput. Syst. Sci. 55 (1997). DOI: `10.1006/jcss.1997.1504`.

[113] J. H. Friedman. "Stochastic gradient boosting". In: Computational Statistics Data Analysis 38 (2002).

[114] H. Zhang. "The Optimality of Naive Bayes". In: Proceedings of the Seventeenth International Florida Artificial Intelligence Research Society Conference. AAAI Press, 2004.

[115] G. H. John and P. Langley. "Estimating continuous distributions in
bayesian classifiers". In: Proceedings of the 11th Conference on Uncertainty in Artificial Intelligence. Morgan Kaufmann Publishers Inc., 1995.

[116] A. Ramdas, N. Garcia, and M. Cuturi. "On Wasserstein Two Sample Testing and Related Families of Nonparametric Tests". In: Entropy 19 (2015). DOI: `10.3390/e19020047`.

[117] R. J. Barlow. Statistics: A Guide to the Use of Statistical Methods in the Physical Sciences (Manchester Physics Series). Reprint. WileyBlackwell, 1989. ISBN: 0471922951.

[118] R. Abbasi et al. "Improved Characterization of the Astrophysical Muon–neutrino Flux with 9.5 Years of IceCube Data". In: Astrophys. J. 928.1 (2022). DOI: `10.3847/1538-4357/ac4d29`.

[119] L. Rädel. "Measurement of High-Energy Muon Neutrinos with the IceCube Neutrino Observatory". PhD thesis. RWTH Aachen University, 2017.

[120] M. G. Aartsen et al. “Observation and Characterization of a Cosmic Muon Neutrino Flux from the Northern Hemisphere Using Six Years of IceCube Data”. In: ApJ 833 (2016). DOI: `10.3847/0004-637X/833/1/3`.

[121] J. Ahrens et al. “Muon Track Reconstruction and Data Selection Techniques in AMANDA”. In: Nuclear Instruments and Methods in Physics Research Section A: Accelerators, Spectrometers, Detectors and Associated Equipment 524 (2004). DOI: `10.1016/j.nima.2004.01.065`.

[122] M. Zoll. “A search for solar dark matter with the IceCube neutrino detector : Advances in data treatment and analysis technique”. PhD thesis. Stockholm University, 2016.

[123] IRS Science Team/Joao Teixeira. IRS/Aqua L3 Daily Standard Physical Retrieval (AIRS-only) 1 degree x 1 degree V006, Greenbelt, MD, USA, Goddard Earth Sciences Data and Information Services Center (GES DISC). DOI: `10.5067/Aqua/AIRS/DATA303`.

[124] T. Menne. “Stacking Point Source Search for a Neutrino Contribution at 22 Track-Like HESE Positions using Six Years of IceCube Data”. PhD thesis. TU Dortmund, 2018.

[125] R. Labbe. Kalman and Bayesian Filters in Python. `https://drive.google.com/file/d/0By_SW19c1BfhSVFzNHc0SjduNzg/view`. 2020.

[126] K. Hymon. “Measurements of Seasonal Variations of the Unfolded Atmospheric Neutrino Energy Spectrum with IceCube”. MA thesis. Ruhr-Universität Bochum, 2020.

[127] K. Hymon and T. Ruhe. “Seasonal Variations of the Atmospheric Neutrino Flux measured in IceCube”. In: Proceedings of the 38th International Cosmic Ray Conference (2023).

[128] M.G. Aartsen et al. “In-situ calibration of the single-photoelectron charge response of the IceCube photomultiplier tubes”. In: Journal of Instrumentation 15 (2020). DOI: `10.1088/1748-0221/15/06/P06032`.

[129] A. Fedynitch, W. Woodley, and M.-C. Piro. “On the Accuracy of Underground Muon Intensity Calculations”. In: Astrophys. J. 928 (2022). DOI: `10.3847/1538-4357/ac5027`.

[130] A. Romanov and P. Kalaczyński. “Comparison of the atmospheric muon flux measured by the KM3NeT detectors with the CORSIKA simulation using the Global Spline Fit model”. In: Proceedings of the 38th International Cosmic Ray Conference (2023). DOI: `10.22323/1.444.0338`.

[131] M. Aartsen et al. “Observation and Characterization of a Cosmic Muon Neutrino Flux from the Northern Hemisphere using six years of IceCube data”. In: The Astrophysical Journal 833 (2016). DOI: `10.3847/0004-637X/833/1/3`.

[132] I. Fredholm. “Sur une classe d’équations fonctionnelles”. In: Acta Math. 27 (1903). DOI: `doi:10.1007/BF02421317`.

[133] V. Blobel and E. Lohrmann. Statistische und numerische Methoden der Datenanalyse. Teubner Verlag Stuttgart, 1998.

[134] V. Blobel. “Unfolding methods in high-energy physics experiments”. In: CERN school of computing ’84. 1985.

[135] A. N. Tikhonov. “On the solution of ill-posed problems and the method of regularization”. In: Dokl. Akad. Nauk SSSR 151 (1963).

[136] T. K. Gaisser. Cosmic rays and particle physics. Cambridge University Press, 1990.

[137] J. Beringer et al. “Review of Particle Physics”. In: Phys. Rev. D 86 (2012). DOI: `10.1103/PhysRevD.86.010001`.

[138] G. D’Agostini. “A Multidimensional unfolding method based on Bayes’ theorem”. In: Nucl. Instrum. Meth. A362 (1995). DOI: `10.1016/0168-9002(95)00274-X`.

[139] V. Blobel. “An Unfolding Method for High Energy Physics Experiments”. In: arxiv.org/abs/hep-ex/0208022 (2002).

[140] M. Bunse. [Online: 02.10.2020]. URL: `https://sfb876.tu-dortmund.de/deconvolution/index.html`.

[141] T. Ruhe et al. “ DSEA: A Data Mining Approach to Unfolding”. In: Proceedings of the 33rd International Cosmic Ray Conference (2013).

[142] M. Bunse. “DSEA Rock-Solid – Regularization and Comparison with other Deconvolution Algorithms”. MA thesis. TU Dortmund, 2018.

[143] J. Nocedal and S. J. Wright. Numerical Optimization. 2e. New York, NY, USA: Springer, 2006.

[144] N. Milke. “Unfolding of the atmospheric neutrino flux spectrum with the new program TRUEE and IceCube”. PhD thesis. TU Dortmund, 2012.

[145] T. Ruhe. “Data Mining on the Rocks”. PhD thesis. TU Dortmund, 2013.

[146] M. Börner. “Bestimmung des Energiespektrums von atmosphärischen Myonneutrinos mit 3 Jahren Daten des IceCube-Detektors”. PhD thesis. TU Dortmund, 2018.

[147] R. Abbasi et al. “An improved method for measuring muon energy using the truncated mean of dE/dx”. In: Nuclear Instruments and Methods in Physics Research Section A Accelerators Spectrometers Detectors and Associated Equipment A703 (2013). DOI: `10.1016/j.nima.2012.11.081`.

[148] K. Morik and W. Rhode, eds. Volume 2 Machine Learning under Resource Constraints - Discovery in Physics. Berlin, Boston: De Gruyter, 2023. ISBN: 9783110785968. DOI: `doi:10.1515/9783110785968`.

[149] D. Ruppert. Efficient Estimations from a Slowly Convergent Robbins-Monro Process. Cornell University Operations Research and Industrial Engineering, 1988.

[150] K. Hymon and T. Ruhe. “Seasonal Variations of the Unfolded Atmospheric Neutrino Spectrum with IceCube”. In: Proceedings of the 37th International Cosmic Ray Conference (ICRC 2021) (2021).

[151] M. G. Aartsen et al. “Development of a General Analysis and Unfolding Scheme and its Application to Measure the Energy Spectrum of Atmospheric Neutrinos with IceCube”. In: Eur. Phys. J. C 75 (2015). DOI: `10.1140/epjc/s10052-015-3330-z`.

[152] M. G. Aartsen et al. “Measurement of the ν_μ energy spectrum with IceCube-79”. In: Eur. Phys. J. C 77 (2017). DOI: `10.1140/epjc/s10052-017-5261-3`.

[153] A. Albert et al. “Measurement of the atmospheric ν_e and ν_μ energy spectra with the ANTARES neutrino telescope”. In: Phys. Lett. B 816 (2021). DOI: `10.1016/j.physletb.2021.136228`.

[154] M. G. Aartsen et al. “Efficient propagation of systematic uncertainties from calibration to analysis with the SnowStorm method in IceCube”. In: Journal of Cosmology and Astroparticle Physics 2019 (2019). DOI: `10.1088/1475-7516/2019/10/048`.

[155] M. G. Aartsen et al. "Measurement of South Pole ice transparency with the IceCube LED calibration system". In: Nucl. Instrum. Meth. A 711 (2013). DOI: `10.1016/j.nima.2013.01.054`.

[156] D. Chirkin. "Evidence of optical anisotropy of the South Pole ice". In: Proceedings of the 33rd International Cosmic Ray Conference (2013).

[157] D. Williams. "Light propagation in the South Pole ice". In: AIP Conference Proceedings 1630 (2014). DOI: `10.1063/1.4902793`.

[158] M. Ackermann et al. "Optical properties of deep glacial ice at the South Pole". In: J. Geophys. Res. 111.D13 (2006). DOI: `10.1029/2005JD006687`.

[159] A. Fedynitch, J. Tjus, and P. Desiati. "Influence of hadronic interaction models and the cosmic ray spectrum on the high energy atmospheric muon and neutrino flux". In: Physical Review D 86 (2012). DOI: `10.1103/PhysRevD.86.114024`.

[160] J. A. Nelder and R. Mead. "A simplex method for function minimization". In: Computer Journal 7 (1965).

[161] H. Hersbach et al. ERA5 monthly averaged data on pressure levels from 1940 to present. Copernicus Climate Change Service (C3S) Climate Data Store (CDS) (Accessed on 06-06-2023). DOI: `10.24381/cds.6860a57`.

[162] E. W. Grashorn et al. "The Atmospheric charged kaon/pion ratio using seasonal variation methods". In: Astropart. Phys. 33 (2010). DOI: `10.1016/j.astropartphys.2009.12.006`.

[163] A. E. Hedin. "MSIS-86 thermospheric model". In: Journal of Geophysical Research 92 (1987).

[164] D. Heck and T. Pierog. Extensive Air Shower Simulation with CORSIKA: A User's Guide. Tech. rep. KIT, 2019.

List of Figures

List of Tables

Acronyms

AdaBoost Adaptive Boosting. 38, 44, 62, 63, 68

AIRS Atmospheric Infrared Sounder. 48, 104, 105, 152–154

AMANDA Antarctic Muon And Neutrino Detector Array. 21, 22, 25

ANIS All Neutrino Interaction Simulation. 31

ANTARES Astronomy with a Neutrino Telescope and Abyss environmental RESearch. 78

ATWD Analog Transient Waveform Digitizer. 30

BDT Boosted Decision Tree. 44–47, 169

CART Classification And Regression Tree. 36, 59

CC Charged-Current. 29, 30, 45

CMB Cosmic Microwave Background. 9, 17

CORSIKA COsmic Ray SImulations for KAscade. 31, 45, 152

CR cosmic ray. 1, 2, 5–11, 14, 15, 18–20, 23, 24, 47, 49, 81, 88, 93, 123, 124, 135, 144, 153, 169, 170

CV cross-validation. 39, 45, 62

DOM Digital Optical Modules. 25–30, 32–34, 41–43, 45, 52, 60, 61, 79, 80, 82, 127, 143, 169

DPM Dual-Parton-Model. 15, 16

DSEA+ Dortmund Spectrum Estimation Algorithm. i, iii, vi, 2, 3, 55, 57–59, 61–63, 65, 67–69, 75, 77, 78, 81, 83, 106–108, 113, 119–121, 143, 169, 170, 173

DT Decision Tree. 35–37, 62, 68

ECMWF European Center for Medium-Range Weather Forecasts. 102, 104, 105, 152–154, 170

ERT Extremely Randomized Trees. 37, 62, 68

fADC fast Analog to Digital Converter. 30

GB Gradient Boosting. 38, 62, 63, 68

GSF Global Spline Fit. 7, 10

GST Gaisser-Stanev-Tilav. 10, 123

GZK Greisen-Zatsepin-Kuzmin. 9

H3a Gaisser-Hillas 3 approximation. 2, 9, 10, 20, 23, 24, 49, 83, 123, 153

H4a Gaisser-Hillas 4 approximation. 10, 123

HiRes High Resolution Fly's Eye. 9

HLC Hit Local Coincidence. 30

ICL IceCube Lab. 27

KATRIN KArlsruhe TRItium Neutrino. 17

LHC Large Hadron Collider. 15

LLHFit Likelihood Fit. 31, 32

MC Monte Carlo Simulation. 31, 45, 54, 56, 61–63, 69, 71, 83, 85, 108, 120, 169

MCEq Matrix Cascade Equations. i, iii, vi, 2–4, 15, 18, 20, 23, 24, 49, 75, 81–99, 101, 103–107, 109–111, 114, 115, 121–125, 127–140, 146–148, 151–154, 170, 171

MPE Multi-Photoelectron. 32–34, 43–45, 48, 60

NB Naive Bayes. 38, 62, 63, 68

NC Neutral-Current. 29, 30

NRLMSISE-00 US Naval Research Laboratory Mass Spectrometer Incoherent Scattering Extension 2000. i, iii, 2, 22–24, 49, 81, 83, 88, 93, 95, 103–105, 124, 135, 151–154

NuGen Neutrino Generator. 31, 45, 49

NuSim Neutrino Simulation. 31

PAO Pierre Auger Observatory. 7–10

PDF probability density function. 32, 33, 39, 57, 58, 75

PE photoelectron. 30, 41, 43, 60

PG Poly-gonato. 10, 123, 124

PMT photomultiplier tube. 27, 30, 79

PROPOSAL PRopagator with Optimal Precision and Optimized Speed for All Leptons. 32

QGS Quark-Gluon-String Model. 15, 16

RF Random Forest. 36, 37, 62–65, 67–69, 73, 121

RUN Regularized UNfolding. 59

SMT Simple Multiplicity Trigger. 30

SPE Single-Photoelectron. 32, 33, 44

SPIce South Pole Ice. 79

SSW Sudden Stratospheric Warming. 21, 154

TA Telescope Array. 7, 8, 10

WD Wasserstein Distance. 39, 62, 63, 65, 68, 121

Publications

Publications with main contributions of the author:

1. K. Hymon and T. Ruhe. *Seasonal Variations of the Unfolded Atmospheric Neutrino Spectrum with IceCube.* PoS ICRC2021 (2021). Ref. [150]
2. K. Morik and W. Rhode, eds. *Volume 2 Machine Learning under Resource Constraints - Discovery in Physics.* Berlin, Boston: De Gruyter, 2023. Ref. [148]
3. K. Hymon and T. Ruhe. *Seasonal Variations of the Atmospheric Neutrino Flux measured in IceCube.* PoS ICRC2023 (2023). Ref. [127]

Acknowledgments

I would like to thank ...

- Prof. Dr. Dr. Wolfgang Rhode for the opportunity to continue my work in Dortmund after my master thesis. Thank you for the support and guidance over the past years, the opportunity to attend a variety of schools and conferences, and for always being supportive in my career.
- Dr. Chris Malena Delitzsch for taking over as a second reviewer of this thesis.
- Serap Tilav for being my advisor during my stay at Bartol, the many discussions about IceCube, neutrinos, muons, and the atmosphere, and for making it possible to come back to Delaware a second time.
- Tim Ruhe for being my advisor especially in the early stages of this work, for discussing DSEA and unfolding.
- Dominik Elsässer for his support and discussions over the past years.
- Frank Schroeder for helping me with organizing the visit to Delaware, and the financial support regarding travel expenses.
- the entire astroparticle group in Dortmund and the Delaware IceCube group for the physics (and non-physics) talks, lunches, and laughs. Life and work became so much more bearable with you, especially in the more stressful times!
- the main conveners of the Cosmic Ray Working Group in IceCube Agnieszka Leszczyńska, Dennis Soldin, and Matthias Plum for always being willing to help, giving guidance, and being very understanding.
- all those who gave some inputs for this thesis: Lucas, Leonora, Simone, Jean-Marco, Giacomo, Stefan, Alexander, Pascal, Janina, and Jan Lukas.

- last but not least all my friends who supported me during my degree, and in particular my parents for holding my back all these years!

Funding Acknowledgments

I would like to thank the German Academic Exchange Service (DAAD) for the opportunity to attend the International Cosmic Ray Conference in Nagoya, Japan.

This work has been supported by the DPG, Collaborative Research Center SFB 876 under the project C3 (https://sfb876.tu-dortmund.de) and the SFB 1491 (https://www.sfb1491.ruhr-uni-bochum.de).